3D RECONSTRUCTION OF BUILDING ROOFTOP AND POWER LINE MODELS IN RIGHT-OF-WAYS USING AIRBORNE LIDAR DATA

YOONSEOK JWA

A DISSERTATION SUBMITTED TO
THE FACULTY OF GRADUATE STUDIES
IN PARTIAL FULFILLMENT OF THE REQUIREMENTS
FOR THE DEGREE OF
DOCTOR OF PHILOSOPHY

GRADUATE PROGRAM IN GEOMATICS ENGINEERING
LASSONDE SCHOOL OF ENGINEERING
YORK UNIVERSITY
TORONTO, ONTARIO

NOVEMBER 2013

Abstract

An overhead power line (PL) corridor area, also known as Right-of-Way (ROW), is vulnerable to risks that have dangerous consequences to utility operators and their customers, as for example the 2003 Northeast blackout. To mitigate the risks, 3D modeling of building and PL objects in the ROW has become a topic of increasing importance. The reason is due to the fact that the 3D models can provide large benefits in effectively performing the PL risk management. For example, the use of PL models allows us to easily determine a clearance quantity between PLs and vegetation by simulating a conductor blowout using its sag and swing position. The use of 3D building models enables us to carry out more precise thermal rating by considering the effect of electromagnetic field of PLs near residential areas. The research objectives aimed to achieve thorough the thesis are to develop methods for reconstructing the models of building and PL objects of interest in the PL corridor area from airborne LiDAR data. For this, it is mainly concerned with the model selection problem for which model is more optimal in representing the given data set. This means that the parametric relations and geometry of object shapes are unknowns and optimally determined by the verification of hypothetical models. Therefore, the proposed method achieves high adaptability to the complex geometric forms of building and PL objects. For the building modeling, the method of implicit geometric regularization is proposed to rectify noisy building outline vectors which are due to the irregular distribution of LiDAR data. A cost function for the regularization process is designed based on Minimum Description Length (MDL) theory which consists of two terms, model closeness and model complexity. The cost function favours smaller deviation between a model and observation as well as orthogonal and parallel properties between polylines. Next, a new approach, called Piecewise Model Growing (PMG), is proposed for 3D PL model reconstruction using a catenary curve model. It piece-

wisely grows to capture all PL points of interest and thus produces a full PL 3D model. However, the proposed method is limited to the PL scene complexity, which causes PL modeling errors such as partial, under- and over-modeling errors. To correct the incompletion of PL models, the inner and across span analysis are carried out, which leads to replace erroneous PL segments by precise PL models. The inner span analysis is performed based on the MDL theory to correct under- and over-modeling errors. The across span analysis is subsequently carried out to correct partial-modeling errors by finding start and end positions of PLs which denotes Point Of Attachment (POA). As a result, this thesis addresses not only geometrically describing building and PL objects but also dealing with noisy data which causes the incompletion of models. In the practical aspects, the results of PL and building modeling should be essential to effectively analyze a PL scene and quickly alleviate the potentially hazardous scenarios jeopardizing the PL system.

To God

And to Miyon and my family

Acknowledgement

Table of Contents

List of Tables

List of Figures

List of Abbreviations

C/A	Coarse/Acquisition
CLF	Compass Line Filter
CP	power line Candidate Point
DD	Double Difference
DoD	Department of Defense
FERC	Federal Energy Regulatory Commission
GPS	Global Positioning System
HT	Hough Transformation
IMU	Inertial Measurement Unit
INS	Inertial Navigation System
KHz	KiloHertz
kV	kiloVolt
LiDAR	Light Detection And Ranging
MDL	Minimum Description Length
NAVSTAR	NAVigation Satellite Timing and Ranging
NERC	North American Electric Reliability Corporation
PL	Power Line
PMG	Piecewise Model Growing
POA	Point of Attachment
PP	power line Primitive Point
PPM	Parts Per Million
PPS	Precise Positioning Service
PRF	Pulse Repetition Rate
PRN	Pseudo Random Noise
ROW	Right Of Way
SD	Single Difference
SPS	Standard Positioning Service

CHAPTER 1

Introduction

1.1 Motivation

An overhead power line (PL) corridor area, also known as Right-of-Way (ROW), is vulnerable to risks that have dangerous consequences for utility operators and their customers. Possible dangerous elements that threaten PL systems are mainly subject to three issues: vegetation encroachments, PL component anomalies, and unforeseen events. Vegetation is the most hazardous object in ROW as it is possible for vegetation to come into contact with overhead PLs by growing in and falling down within and outside ROW. Moreover, as PL structures wear out over time, their inelastic deformations occur. These cause spatial displacements of PL components which result in malfunctions developing in the whole PL network. The damage of PL components can be also affected by unexpected situations, such as large wind vibration, corona effect, icing, lightning, contamination flashovers, earthquakes, forest fires and so on. Any one of these hazardous events might result in a huge power outage. The 2003 Northeast blackout was mainly caused by the interference of trees with overhead PLs, which affected more than 50 million people who had to rely on limited public services over the following week. This power outage caused financial losses of about $6 billion (Figure 1.1). If the potential vegetation-related risk factors had been identified in time, the accident could have been prevented. In 2005, the Java-

Bali blackout occurred due to the supply's shortfall, affecting about 100 million people and causing major traffic jams as well as interruption of electricity to homes and businesses throughout the day. In this case, an accurate PL thermal rating analysis would have helped to control the increase of the electrical capacity, thereby avoiding the large blackout. In addition, in 2003, the blackout in Italy that happened due to windstorm damages left more than 55 million people without normal electric services over several days.

Figure 1.1: Toronto city view before (City of Toronto, up) and after (National Post on August 14, 2003, down) the 2003 Northeast blackout.

NERC (North American Electric Reliability Corporation), which is certified by the U.S. Federal Energy Regulatory Commission (FERC) and governmental authorities in Canada, was established to ensure the reliability of the North American bulk power system in 1968. Its primary duty is to develop and enforce standards that are related to the connection, reliability, and operation of the electric PL system. If a failure to follow the NERC standards occurs, maximum $1 million US per day is imposed to associated utility firms as a fine (Hurysz and Crider, 2009). To avoid the potential failure, utility firms should check the condition of the conductor and insulator, conductor sag-tension, structure vibration and alignment, the condition of the guy wire and structure footings, and other structures related to the PL system during the regular inspection cycle. The NERC standards also significantly specify the regulation on vegetation-related violations (i.e., vegetation encroachments) as the vegetation has the most potential to be a hazardous object to the PL structure. This interference has contributed to over 30% of service interruptions, which corresponds to the economic loss of approximately $40 billion US per year (Goodfellow and Peterson, 2011).

Recently, the NERC decided to change the target PL voltages which are needed to be monitored according to its specific regulations from 200 kV and above to 100 kV and above. In addition, the NERC standard related to vegetation management (Facilities Design, Connections, and Maintenance, FAC003) was revised to enhance the reliability in managing vegetation located near to PL systems (Flood, 2011). In this context, utility firms are strongly demanded from the regulations enforced by the NERC to precisely identify violations as much as possible and rapidly eliminate them to prevent potential power outages. To effectively meet the NERC's requirements, many utility firms have recently changed from a conventional inspection technique to a new automatic workflow using the state-of-the-art data acquisition systems. The conventional method relies on aerial- and ground-based human inspection with optical measuring devices to remove

potential hazardous elements around the ROW. Since the aforementioned large critical blackouts, the existing workflow has been recognized as insufficient for monitoring the risks of PL systems. In other words, it is cost-effective, but is less accurate. In recent years, the new system, airborne LiDAR system using LiDAR, digitial cameras, and video sensors, has been introduced to establish a new PL maintenance workflow taking into account a trade-off between cost and accuracy. For instance, compared to the conventional method, the airborne LiDAR system based inspection is approximately 1.5 times higher in cost per circuit mile, but more than 2 times higher in accuracy for correctly detecting vegetation-related violations. Moreover, the cost of airborne LiDAR equipment has continuously decreased since its initial usage for the ROW management in 2007. This means that the airborne system based maintenance becomes the most effective approach with respect to cost as well as accuracy (Narolski, 2010).

In terms of industry needs, PL risk management works focus on three main tasks: vegetation management, thermal rating, and asset management (Sohn and Ituen, 2010). These tasks are performed through the evaluation of as-built condition which corresponds to comparing the original design condition with the current condition of ROW, thereby identifying clearance issues. In the vegetation clearance management, since vegetation is grown to all possible scale with respect to its life cycle, it is not easy to precisely identify potentially hazardous vegetation to PL structures especially using the conventional inspection techniques. The best way to assess the necessary clearance area is to employ a PL model-based inspection workflow. This means that the clearance quantity can be easily determined by simulating a conductor blowout based on its maximum designed sag and swing position. Next, a thermal rating of PLs is the process of determining a certain conductor temperature to prevent the unpredictable elongation of conductors. The conductor elongation causes the conductor sag positions to drop down and come into contact with other objects such as vegetation and buildings. This might result in a mechanical

failure of the PL system. Additionally, in the residential area, it is required to carry out more precise thermal rating by taking into account the public safety which is closely related to concerns over potential adverse health effects. If the geometric PL models are ready, it allows us to precisely estimate the PL sag positions by changing the operating temperatures which mostly depend on the amount of electrical energy flowing through PLs. In addition to the benefits provided by PL models, if the information of 3D building models is compiled with a PL corridor map, safety zones with respect to the probable risks can be accurately determined between PLs and buildings. Based on the safety zones specified, the thermal rating is effectively performed by adjusting the magnitude of the current flow of PLs. For the asset management, as PLs are connected to the corresponding components such as a pylon and insulators, PL models become significant in easily inspecting any inelastic deformations of the components which are usually derived from positional movements of PLs over time.

In the PL corridor area, as aforementioned, the geometric information of PLs and buildings ensures that it allows us to precisely identify violations which should be cleared between PLs and other objects. In this regard, more detailed study and stronger research on modeling of PL and building objects is needed to be tackled in the following issues:

- *Accuracy*: in practice, most utility firms simply generate PL models under the assumption that conductors are isolated enough to separate each other. However, the use of the assumption mostly causes bundle conductors to be over-simplified as for example one PL model, where PLs in the bundle conductors are normally close to each other with the orthogonal distance of about 30 cm. If the design accuracy of conductor which is approximately 15 cm in the as-built condition is taken into account (Lu and Kieloch, 2008), the over-simplified model is not appropriate for the application of precise PL

management. Additionally, even though the accurate PL modeling is achieved, it is also required to precisely determine start and end positions of PL models, called Point Of Attachment (POA). In most utility companies, POAs are manually determined by dotting points on the raw data, so that it is sometimes hard to obtain the acceptable positional accuracy level of POAs (i.e., ~40 cm). To supplement the difficulty, PL models, if are properly extracted, should be initially used for the detection of accurate POAs because POAs are placed along the corresponding PLs in reality. Consequently, a PL model with the accurate POAs helps to identify the accurate clearance area based on the simulation of conductor motion using two POAs. In this study, the required modeling scheme has high representational power for capturing PL shape details.

- *Robustness***:** In recent years, the PL corridor mapping enables detailed capture of a 3D PL scene with high point density (more than 30 points/m^2). However, the PL scene complexity frequently restricts the capability of recognizing PL objects from the LiDAR data. The complexity can be derived from various factors such as object encroachments and occlusions as well as the complicated distribution of the PL network. These factors mostly cause high irregularity in the distribution of PL points, resulting in data gaps from a centimetre to meter level on PLs. To perform a robust PL modeling, the proposed modeling scheme should be much less sensitive to the presence of PL scene complexity.

- *Automation:* Many utility firms have currently adopted a semi-automatic approach for the modeling of PLs and buildings, which is developed based on COTS (Commercial Off-The-Shelf) software such as the well-known TerraScan software. The use of the COTS product obviously causes the manual interventions to manipulate each module of the COTS software and hence the rapid PL modeling for an immediate response to violations to PL structure is hard to be achieved. In recent years, some utility firms have been trying

to complete the total workflow for PL risk management within 72 hours (Neal 2009) to prevent a hazardous situation while minimizing human-based activities. To meet the aimed timeline, developing a new automatic approach for processing raw data and modeling associated objects seems to be inevitable.

- *Regularization*: The process of data-driven building modeling (i.e., generic building modeling) usually relies on the geometric information collection in the form of modeling cues/primitives (i.e., lines, corners, planes). As observations (LiDAR data) are inevitably corrupted by noise and scene complexity, the sequences of primitives cause geometric distortions in the final shape of building model. In practice, common building rooftops show specific regularities between boundary lines or plane segments such as parallelity, collinearity, and orthogonality. For this, a new shape reconstruction scheme for building rooftop modeling is required by imposing the geometric regularities to the noisy building vectors.

1.2 Objectives of the thesis

The research objectives aimed to achieve through the thesis are to develop methods for reconstructing the models of building and PL objects of interest in the PL corridor area from Airborne LiDAR data. The resulting building rooftop and PL models are also required to be satisfied with requirements addressed in the four issues, accuracy, robustness, automation, and regularization. For this, the thesis is mainly concerned with the *model selection problem* for which model is close to optimal in representing the given data set. Here, the term *model* means the *hypothetical* description of a real object. The model is also used to denote a *geometric model* that explicitly expresses the structure of an object with a finite number of adjustable parameters. As

data acquired by sensors contain random errors, a resulting model derived from the data is not completely identical to its real shape. So, every model generated is to be hypothetical. The *model selection* is a process in which an appropriate model is determined among a set of candidate models based on the *model selection criterion* defined. Where, the all candidate models represent the given data and are differently parameterized. The selection criterion is normally comprised of two issues; how to optimally fit the model to the data and how to simply explain the data using the model. The first criterion can be easily formulated based on the principle of maximum likelihood. The maximum of the likelihood is thus achieved when the observed sequence is represented by using as many parameters as possible. However, the criterion only following the maximum likelihood principle definitely fails to produce an optimal model due to the occurrence of over-fitting problem. The most common way to correct the model selection problem is to adopt a combined criterion by considering the second criterion, a term of model complexity. This is motivated by Ockham's razor, a simple explanation of the facts is better than a complex one (Hansen and Yu, 2001). In this sense, the best/optimal model requires the simpler description with respect to the model complexity and at the same time the higher goodness-of-fit between a model and data. As a result, properly combining the criteria is vital for an optimal model selection in this study. Note that there is no guarantee that the use of combined criteria can select a desired global model, but it can give us an expectation that the selected model will be near to the best ideal model.

1.3 General framework

Figure 1.2 schematically shows the whole workflow diagram of the proposed approach for the automatic building and power line modeling. The main data source used for this study is laser point clouds acquired by the airborne LiDAR system. For the building modeling, the method of implicit geometric regularization is proposed to rectify noisy building outline vectors. Due to the use of data-driven approach, the research is mainly concerned with rectifying the irregular rooftop shape under the assumption that building rooftops are comprised of generic plane surfaces. It is performed based on Minimum Description Length (MDL) theory, which is motivated by the study on a local MDL-based regularization of noisy building outlines (Weidner and Forstner, 1995). Next, a new method, called Piecewise Model Growing (PMG), for the 3D PL model reconstruction is proposed, which is a model-based hypothesis verification and propagation process. The proposed method starts by detecting PL candidate points. Then an initial catenary model generated over the candidate points piece-wisely grows to capture all PL points of interest and thus converted into a full PL 3D model. However, the proposed method is limited to the PL scene complexity, which causes PL modeling errors such as partial, under- and over-modeling errors. To correct the incompletion of PL models, the inner and across span analysis are carried out, which leads to replace erroneous PL segments by precise PL models. The inner span analysis is performed based on the MDL theory to correct under- and over-modeling errors. The across span analysis is subsequently carried out to correct partial-modeling errors by finding start and end positions of PLs (i.e., POAs), thereby producing complete PL models.
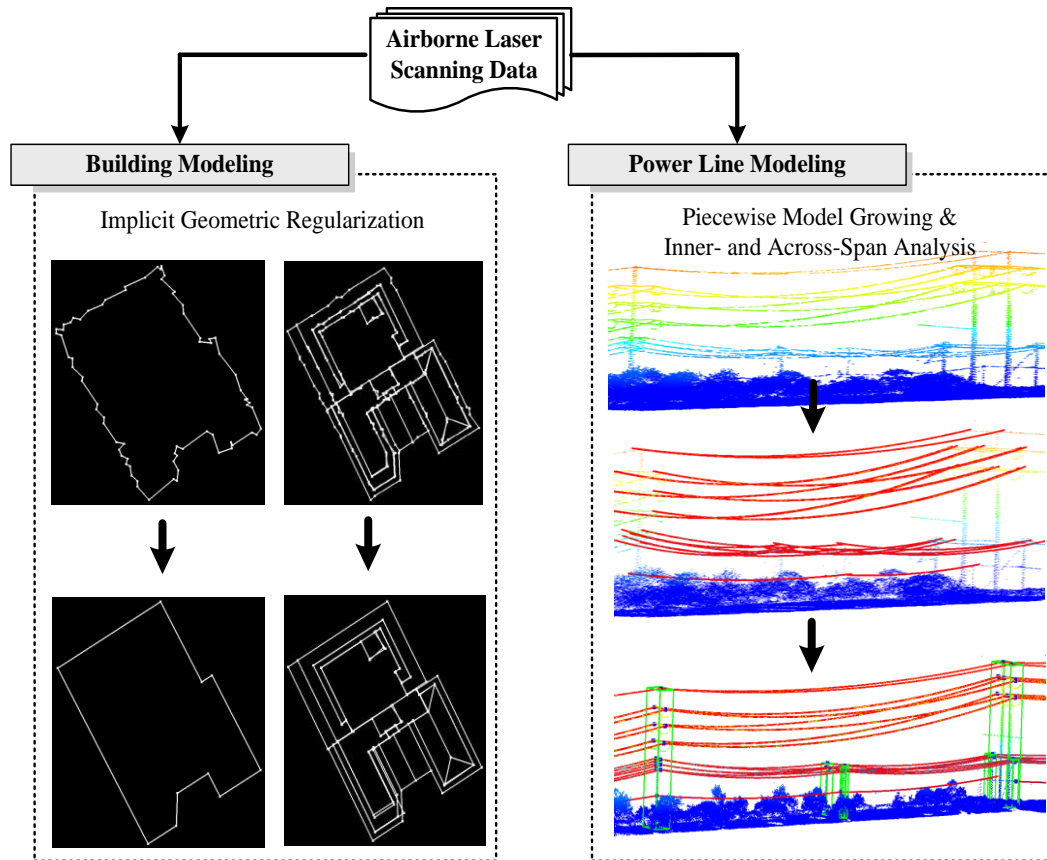
Figure 1.2: Schematic workflow of proposed methods for 3D reconstruction of buildings and PLs in PL corridor area (ROW).

1.4 Contributions

My main achievements of this study were to develop a robust solution for the automatic modeling of buildings and PLs from airborne LiDAR data in order to fulfill the effective power line risk management in the PL corridor area. All the proposed algorithms are implemented and their performances are evaluated. The main contributions are itemized as follows:

- Introducing a new method, called implicit geometric regularization, for 3D shape reconstruction of building rooftops from noisy airborne LiDAR data. The innovational aspect is that redundant line segments which are frequently caused by data-driven modeling approach are minimized with geometric regularities such as parallelity, collinearity, and orthogonality. The regularities are also implicitly represented to rooftop models by a set of rules defined during the regularization process without explicitly using hard constraints.

- Presenting a new method, called Piecewise Model Growing (PMG), for 3D PL model reconstruction using a catenary curve model. The key aspect is that the proposed PL modeling process is less sensitive to the lack of data information representing PL objects which is caused by a PL scene complexity. Moreover, the PMG method enhances the efficiency of PL modeling process by simultaneously capturing PL points and modeling PLs. This is in contrast to the general approach that *a priori* information such as labelled PL points in incorporated into the PL modeling process.

- Proposing a new method for rectifying 3D PL modeling errors using the inner and across span analysis. The highlighted fact is that the proposed method is capable of dealing with noisy data corrupted under the windy environment and predicting suitable model parameters, resulting in the correction of PL modeling errors such as partial-, under-, and

over-modeling errors. Thus, the proposed method produces promising results in the extraction of accurate PL model including associated POA information, which leads to achieve the geometric and topological completion of PL models in forming the whole PL network.

1.5 Thesis outline

An overview of the chapters is introduced as follows:

Chapter 1: an introduction to the motivation of this study and the proposed approach for solving research questions.

Chapter 2: a summary of the recent trends of PL risk management and the previous researches on PL and building modeling. In addition, the background knowledge of airborne LiDAR system is briefly introduced.

Chapter 3: a development of a new method for regularizing noisy building vectors derived from LiDAR points. A cost function for the regularization process is designed based on the MDL theory.

Chapter 4: an introduction of a new algorithm for reconstructing 3D PL models using a catenary curve model. Model parameters are estimated based on a model-based hypothesis verification and propagation process.

Chapter 5: a suggestion of a new approach for rectifying PL modeling errors. The rectification process is performed by the inner and across span analysis. Additionally, information on POAs and pylon positions is extracted as by-products which are also important factors in constituting the PL network.

Chapter 6: a conclusion of this study and a direction of future works.

CHAPTER 2

Background

In general, a PL corridor area, called Right-of-Ways (ROW), is comprised of very extensive transmission networks. For example, Canada's bulk transmission network is only the fifth largest producer in the world, carrying 4 percent of the world's total, yet this network consist of more than 160,000km of high voltage lines with above 50kV (Industry Canada, 2008). Recently, North American Electric Transmission Investments has announced a future plan that $160 billion US will be invested in the electric transmission including more than 30,000 km of new and upgraded lines from 2012 to 2020. As the ROW is vulnerable to risks that have dangerous consequences for utility operators and their customers, monitoring and maintenance of extensive PL networks have become a topic of increasing importance. This chapter summarizes the recent trends of PL risk management and state-of-the art techniques in reconstructing PL and building models are discussed. In addition, the background knowledge of airborne LiDAR system is briefly introduced.

2.1 Power line risk management

The tasks of PL risk management over a long PL corridor (i.e., ROW) include risk monitoring, risk identification, risk assessment, and risk clearance. This is for serving a reliable supply of electricity to customers at all times. The risk monitoring process commonly involves a scheduled maintenance cycle for ROW inspections. For example, the detailed climbing inspection for the high-voltage PLs is performed on a 5-year cycle and aerial inspections are visually completed several times a year (Shoemaker and Mack, 2011). While monitoring the ROW, the identification of possible risk factors to PL systems is carried out. The potentially hazardous scenarios jeopardizing PL systems are normally alleviated by identifying anomalies in PL structure and vegetation-related Clearance 1 and Clearance 2 in ROW (Strmiska, 2000; Neal, 2009). The first violation is related to the damage of PL components by wind vibration (Diana et al., 2005), the corona effect (Zhao et al., 1996), corrosion (Smith and Hall, 2011), icing (Ma et al., 2011), ambient temperature, earthquakes, lightning, contamination related flashovers and so on. During the regular inspection cycle, utility firms should check the condition of the conductor and insulator, conductor sag-tension, structure vibration and alignment, the condition of the guy wire and structure footings, and other structures related to the PL system. Next, the second violation is reported by a vegetation encroachment. Vegetation is the most hazardous object in ROW as it is possible for vegetation to come into contact with overhead PLs by growing in and falling down within and outside ROW. This interference has contributed to over 30% of service interruptions, which corresponds to the economic loss of approximately $40 billion US a year (Goodfellow and Peterson, 2011). The risk assessment is a process for the determination of clearance quantity according to the defined clearance criteria. Since measuring the clearance quantity is associated with assessing a certain amount on the occurrence probability of dangerous situations, it can be the most difficult task which results in the most time-consuming work in the PL risk management

workflow. Lastly, the risk clearance is accomplished by eliminating the risk factors to the PL systems based on the clearance quantity assessed.
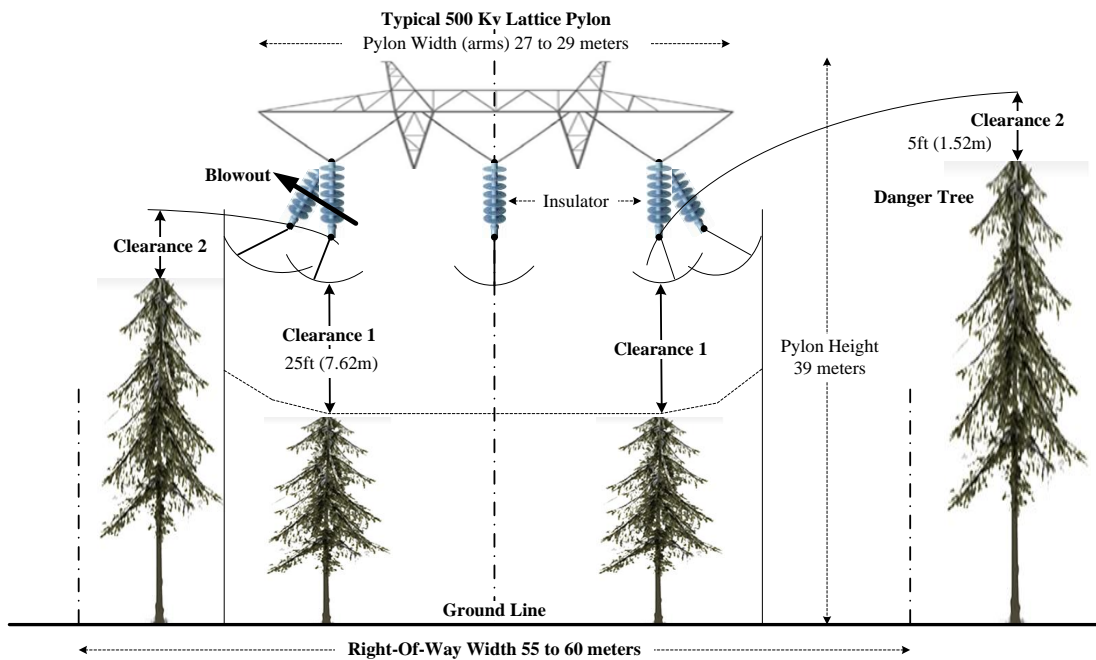
Figure 2.1: Vegetation management in the PL corridor area with respect to certain regulations (Clearance 1 and 2).

For the vegetation management, as shown in Figure 2.1, the ground clearance around ROW is first performed. This is done through the year-round pruning, trimming, and removing of trees. All trees as well as under-brush within a specific distance of overhead PLs should be removed. The distance for clearance is normally determined to be a gap of at least 7.62 m (25 ft) under each conductor within ROW. If trees fall from the outside to the inside of ROW and come within approximately 1.52 m (5 ft) of a conductor, they are categorized as danger trees and a cutting operation is required to maintain the required minimum safety criteria (Shoemaker and Mack, 2011). As a result, if the maintenance work with respect to the aforementioned violations is not

carried out at the appropriate time, a lot of complications including increased equipment failure, higher maintenance costs and a higher frequency of outages may arise.

In the fulfillment of PL monitoring and risk identification work, many utility firms have adopted a conventional inspection technique. The technique relies on aerial- and ground-based human inspection with optical measuring devices to remove potential hazardous elements around the ROW. However, since the large critical blackouts such as 2003 Northeast blackout, the conventional maintenance workflow has been recognized as an insufficient approach for monitoring the risk situations of PL systems (Ituen and Sohn, 2008). In other words, the conventional workflow is cost-effective, but is less accurate. In recent years, as state-of-the-art data acquisition systems using LIDAR, digital cameras, and video sensors, have been introduced, many researchers and utility companies have been trying to establish a new automatic workflow for more effective PL corridor management through a trade-off between cost and accuracy. For instance, compared to the conventional method, an airborne LIDAR-based inspection is approximately 1.5 times higher in cost per circuit mile, but more than 2 times higher in accuracy for correctly detecting vegetation-related violations. Moreover, the cost of airborne LIDAR equipment has continuously decreased since its initial usage in 2007, which indicates that the airborne LIDAR-based maintenance is the most effective approach with respect to cost as well as accuracy (Narolski, 2010). This shift is inevitable because the limitations of the conventional approach (i.e., a time-consuming work, large gross inspection errors and so on) are hampering an immediate response to undesirable events such as vegetation encroachments. By using LiDAR measurements, detecting and modeling objects of interest, for instance, PLs, pylons, insulators and other PL components as well as buildings, trees, terrain, and other neighboring features, are required to establish geometrical relationships between them for the identification of violations. As a result, it ensures that an accurate and time- and cost-effective PL maintenance can be carried

out using the rapid mapping products. In this study, the main emphasis lies on 3D modeling of man-made objects, PLs and buildings, as main features in ROW. Their significance and benefits for the effective PL risk management are discussed in greater detail in the following sections.

2.1.1 Scene complexity of power line corridor area

In general, buildings are known as one of the most difficult for reconstructing 3D models regardless of where they are, for example a rural, urban, or PL corridor area. This is due to the high dimensional variations in the structure and shape, occlusions by neighbouring objects such as vegetation, insufficient data representation, and so on. Thus, the focus in this section is on addressing difficulties in modeling PL objects having even a simple linear shape due to a scene complexity of ROW.

A PL is a geometrically distinguishable feature from the other objects in the PL scene. It hangs over the underlying terrain at a certain height and is isolated from its surroundings by a certain distance at all directions. PLs are also successively connected to one another through pylons running in a similar line direction. Although PLs are distinct and isolated objects, a method in automatically reconstructing 3D PL models for the rapid and accurate mapping has been not established. This is due to the fact that PL scenes are complex, which creates obstacles that hinder the robustness of PL reconstruction. The complex factors of the PL scene represented by LiDAR data can be grouped under several aspects: (a) the complexity of PL as-built condition, (b) object encroachment on ROW, and (c) various data quality.

The first complication with PL modeling is that PL networks are distributed in a complex manner for example over urban areas as shown in Figure 2.2. PLs of various voltage types are placed closer together, and go in different directions. Some PLs cross over land, roads, railways, pipelines, residential areas and other wires, often exhibiting a variety of curvatures and

asymmetrical shapes. As a result, these complications cause difficulties in differentiating PL points from the raw data even though the segmentation process is done by a human operator. Second, if the vegetation is integrated with the PLs, as depicted in Figure 2.3, it is very hard to discern PL points from vegetation points. Although points are labelled as a PL class in the vicinity of vegetation, it is not guaranteed to be PL points due to the mixture of points representing PLs and vegetation. This causes the degradation of PL modeling accuracy or a total failure of PL modeling. Third, LIDAR points representing PLs show irregular point densities due to many factors such as the effects of occlusions, PL movements by external forces at the data acquisition epoch, LiDAR system's systematic random errors, and so forth. Figure 2.4 illustrates a typical case of PL point distribution in the densely arranged lines. The line arrangement causes a large occlusion along the downward height direction, which results in the various average point distances per PL ranged from dense (0.17 m) to sparse (1.83 m). In the histogram derived from the point distance factor, PL points in the top show a relatively regular distribution with the high point density in which more than 90% points are placed with point distance of less than 0.5 m. On the other hand, the distribution of PL points in the bottom shows rather irregular in which its range is very broad (i.e., up to 3 m) and only 50 % points are positioned with point distance of less than 0.5 m. Thus, due to the low point density, the linearity of PLs is rather not clear, so that it can affect the modeling success rate and the degree of modeling accuracy. Therefore, if PL points are more regularly distributed with high point density, it surely helps to facilitate the development of automatic modeling approach and improve the modeling quality.
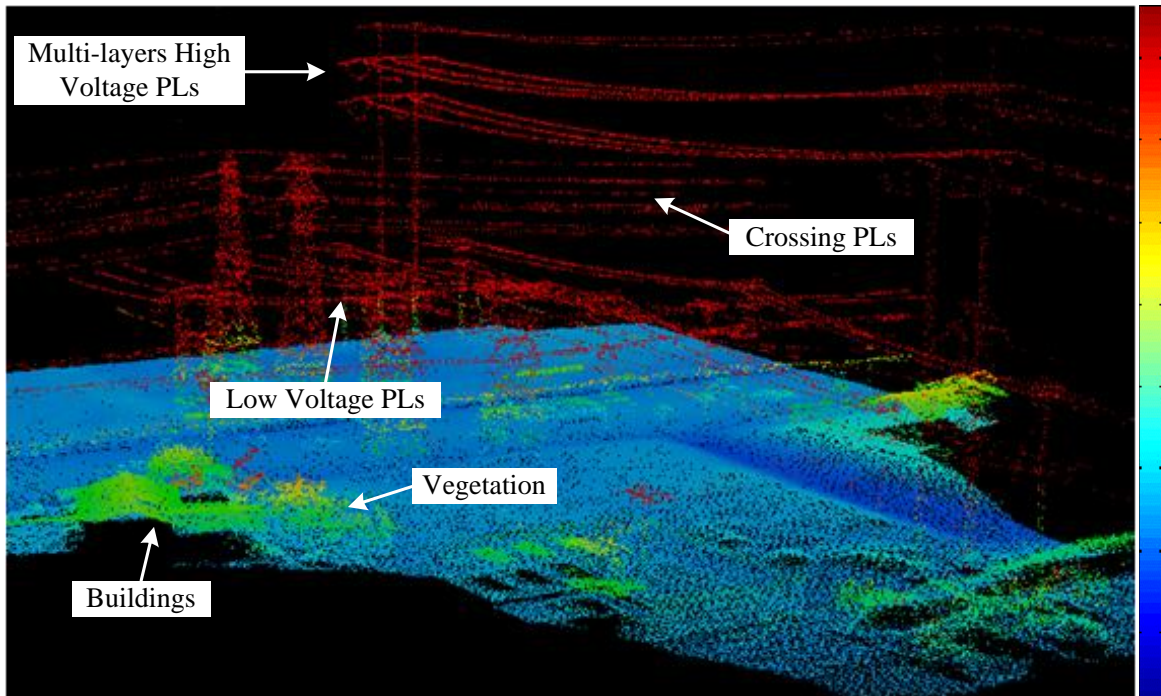
Figure 2.2: PL networks distributed in a complex manner in the urban area: PLs of various voltage types and curvatures are placed closer together and go in different directions. Some PLs cross over other objects such as vegetation and buildings.

Figure 2.3: Vegetation encroachment to PL components in the PL voltage of 69 kV: points representing PLs and vegetation are mixed, so that it is very hard to discern PL points from vegetation points.
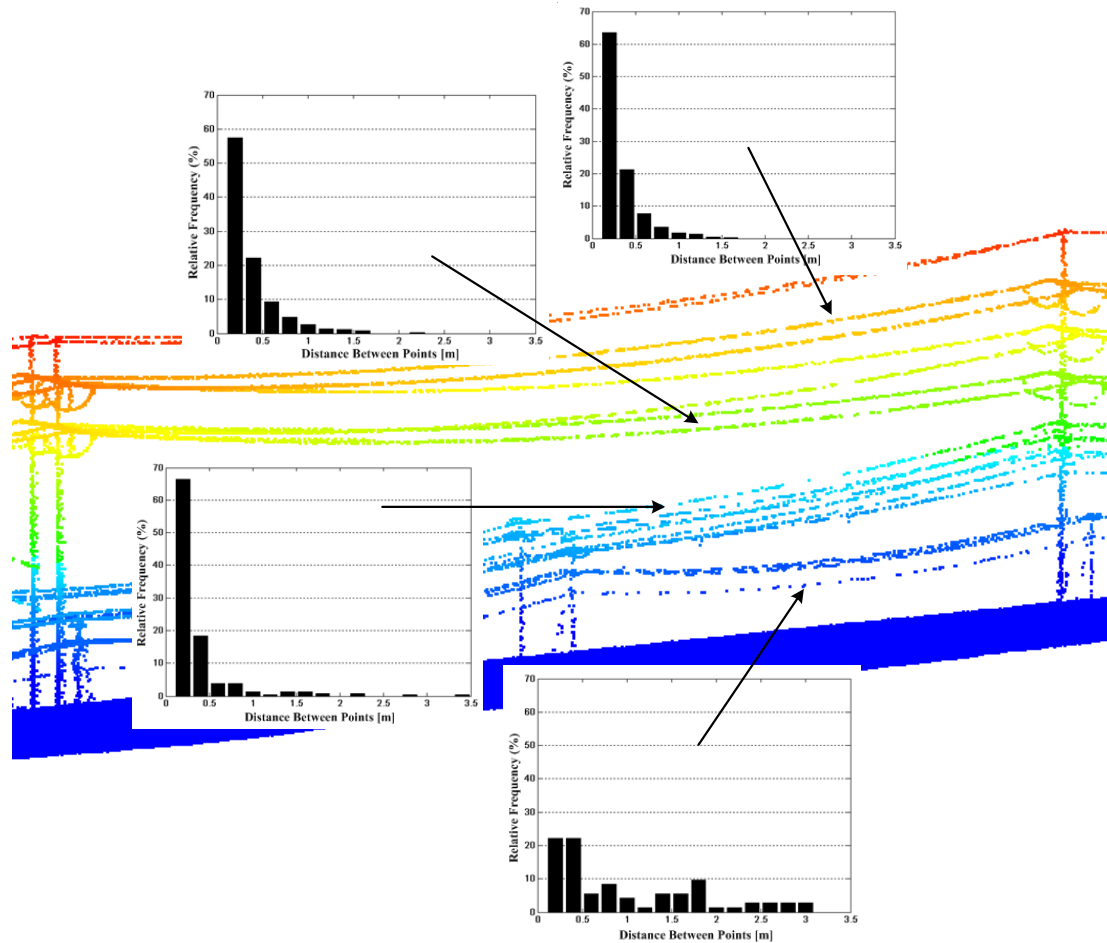
Figure 2.4: Irregular distribution of PL points with varying point density: occlusions of PL-parts by themselves occur due to the distribution of dense arranged lines along the downward height direction.

To alleviate the difficulties in modeling PL objects due to the scene complexity, the technique of data fusion using different data sources such as LiDAR points and imagery data especially thermal image will be useful. In practice, although thermal images are sensitive to ambient conditions such as air temperature and the impact of solar heating, it has been widely used as *a priori* knowledge for the recognition of PL components as well as the investigation of temperature variance for the PL thermal rating. However, the temperature difference between PLs and others

is required to be at least more than 14℃ for effectively detecting PLs (Han et al., 2009). When PLs are detected based on gradients on the image data, the performance of PL detection may be also restricted. This is because the contrast of pixel values between PLs and their backgrounds varies according to the urban and rural area.

2.1.2 3D power line model and its benefits

The PL shape can be approximated by fitting the survey data onto a parabolic form, called a catenary curve, as the PL cable is suspended between two support points and subjected to gravity forces. In general, 3D PL models are extremely useful for determining the as-built condition of PLs in order to deal with the clearance issues in ROW. Where, the evaluation of the as-built condition identifies any changes to the PL by comparing the original design condition to the current condition of ROW. According to Sugden (1994), the catenary curve model for PLs is suitable in performing a multifaceted analysis for normal PL maintenance operations. For example, the design accuracy of conduct sag is normally in the level of approximately 15 cm. If the PL model is reconstructed within the accuracy level, its sag position can be enough used for practical applications such as sag-tension calculations and danger tree analysis (Lu and Kieloch, 2008). Consequently, to mitigate the risks caused by clearance issues and keep the as-built condition, 3D PL models can provide large benefits in terms of three main PL maintenance tasks: vegetation management, thermal rating, and asset management (Franken, 2003; Sohn and Ituen, 2010).

Vegetation management: As vegetation is spatio-temporally grown at all possible scales according to its life cycle, it is not easy to precisely identify potentially hazardous vegetation to PL structures in ROW. For example, vegetation grows 11% faster after drought years compared to pre-drought rates (Orwig and Abrams, 1997). The best way to minimize vegetation-caused PL

outages is to add PL model-based inspections into the regular monitoring cycle of PL system. If a geometric PL model is ready, the accurate clearance area can be easily determined by simulating a conductor blowout based on its maximum designed sag and swing position as well as the potential growth rate of vegetation. The simulation can be more robust when the accurate start and end position of PL models (i.e., POAs) is determined. The reason is that the accurate swing position of conductors depends on the accuracy of POAs.

Thermal rating: A thermal rating of PLs is the process of determining a certain conductor temperature to prevent the unpredictable elongation of conductors. If the conductor sag position drops down to the underlying terrain surface, it might cause a mechanical failure of the PL system as the PLs come into contact with other features such as vegetation and buildings. The conductor elongation is affected by atmospheric conditions as well as various loads including elastic strain, long-time creep strain and thermal strain. Among them, the thermal strain depending on the amount of electric current flow is the most critical factor to the elongation. If the conductor temperature remains high for a longer time period, the conductor strength and tension will suddenly decrease. This sometimes leads to its physical damage which results in a huge power outage when a high wind loading occurs. To avoid a situation like this, measuring the accurate temperature of conductors is very helpful to estimate the allowable amount of current flow within the required minimum safety criteria of PL system. Based on the formulation derived from PL temperature and line sag relationship (Rahim et al., 2010), 3D PL model can play a significant role in estimating the PL sag position with respect to the change of its operating temperature. In addition, the thermal rating analysis ensures the cost-effective maintenance of PLs by avoiding constructing additional PLs to meet electrical power needs. For example, the cost of establishing a new 115 kV steel pole double circuit is 30 times more than one of a thermal re-rating per mile (Franken, 2003).

Asset management: As a PL structure wears out over time, its maintenance should be carried out in a timely manner to prevent electric failures. For instance, as the corrosion of a pylon accelerates quickly after 30 years, older pylons should be inspected regularly within a limited time period to identify their inelastic deformations (Smith and Hall, 2011). Since PLs are successively connected to pylon structures as well as other PL components across the span, it is convenient to inspect any inelastic deformations of PL system by measuring movements of PL positions over time. Therefore, PL models in which the data used for the modeling are collected in the spatio-temporal domain can be effectively used to identify the geometrical anomalies of PL components.

2.1.3 3D building model and its benefits

Buildings as a man-made structure exhibit a range of rooftop types and a complex combination of building parts including roof superstructures. To represent the various building geometries, polyhedral-like models are usually considered to be sufficient for many applications such as Google Earth and Bing Maps (Haala and Kada, 2010). In terms of the modeling methods, the building models are mainly reconstructed based on two approaches: model-driven and data-driven approach. The model-driven method using a parametric modeling scheme adopts pre-defined model types for certain elements such as a gable and hip roof shape. This places some limitations on representing more complex building structures. On the other hand, the data-driven method using a generic modeling scheme allows the arbitrary representation of building shapes, and thus is suitable for more detailed building modeling. For the purpose of precisely analyzing risks between PLs and buildings in ROW, the generic building modeling becomes a more effective approach due to the detailed representation of building rooftops.

PLs are considered as a major source in forming an electromagnetic field at extremely low frequencies such as 50/60 Hz. In recent years, the rapid increase of electric energy utilization has

led to the installation of new PLs inside urban areas, which leads to the increase of the electromagnetic field of PLs near residential areas. This causes public concerns over potential adverse health effects regardless of whether or not a direct link between health risks and electromagnetic fields exists. To reduce the possible health risks from the magnetic field, various regulations related to a minimum distance between PLs and buildings or magnitude of PL voltages near resident area have been formulated. For example, in South Australia, the minimum clearance distance of 20 m for 132 kV and 25 m for 275 kV lines is required. In Florida, US, the magnitude of the electromagnetic field is limited to a range of 15 mT (millitesla) for PLs with a voltage of less than 230 kV, and 20 mT for 500 kV lines (Bakhashwain et al., 2003, Salameh and Hassouua, 2010). Once 3D PL and building models are reconstructed in ROW, safety zones with respect to the probabilistic risks can be formed between them, and then the clearance analysis is carried out. Based on the corresponding regulations for the public safety, the thermal rating is also carried out by adjusting the magnitude of the current flow of PLs. In addition to that, the extension of buildings are easily determined toward the minimization of the impact of PLs' electromagnetic effect on the corridor environment.

2.2 Power line modeling in literature

2.2.1 Power line system overview

A PL system transports electrical energy from distribution facilities, where the energy is derived from generating stations, through transmission line networks to end users such as industries, schools, and homes, as shown in Figure 2.5. The whole PL system is mainly divided into transmission lines, substations, distributing stations and so on. Transmission lines send electrical energy at voltages between 44 Kv and over 735 Kv to a transformer or distributing station. There are two types of PLs, overhead and underground transmission lines. Except in densely populated areas where underground lines are prepared to be placed, overhead lines are normally used. The main reason is subject to a matter of cost, that is, the construction cost is about 5-10 times to have underground transmission lines. Substations provide a site for storing reactors and capacitors for when they are needed for power factor corrections. Distributing stations deliver electrical service to local electrical systems and most of those stations are served at voltage levels of less than 50 kV.

As depicted in Figure 2.6, an overhead PL network is mainly comprised of three components: conductors, insulators and pylons. A basic formation is that a pylon supports three conductors, called three-phase PL system. When three conductors are added to the formation for extending the electrical capacity, it is called a double-circuit transmission line. A space between two pylons denotes a span and neighbouring spans are similar in length. The main components are summarized as follows (Shoemaker and Mack, 2007):
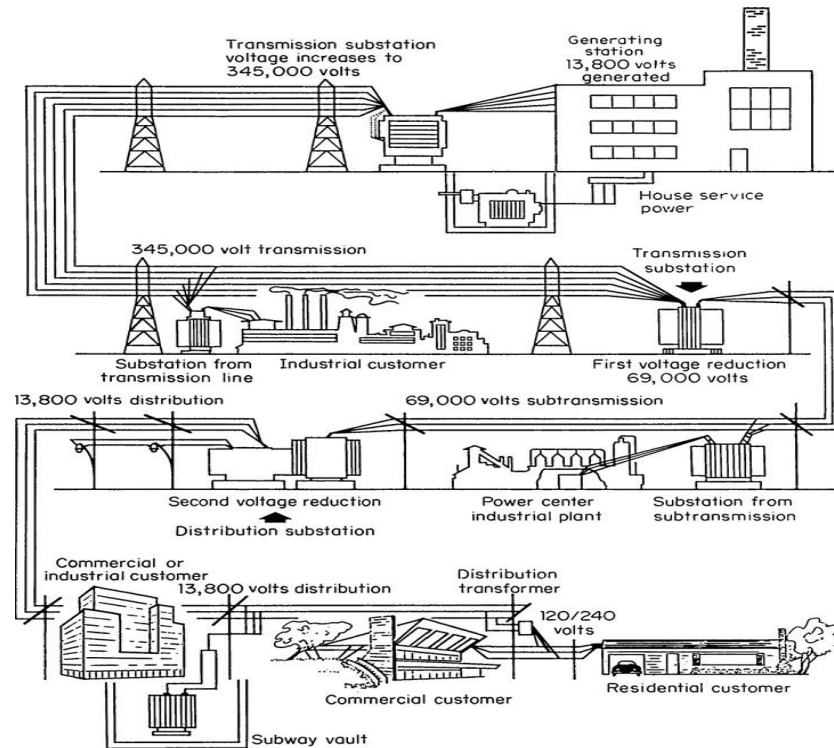
Figure 2.5: Schematic constitution of a general PL network (Shoemaker and Mack, 2007).
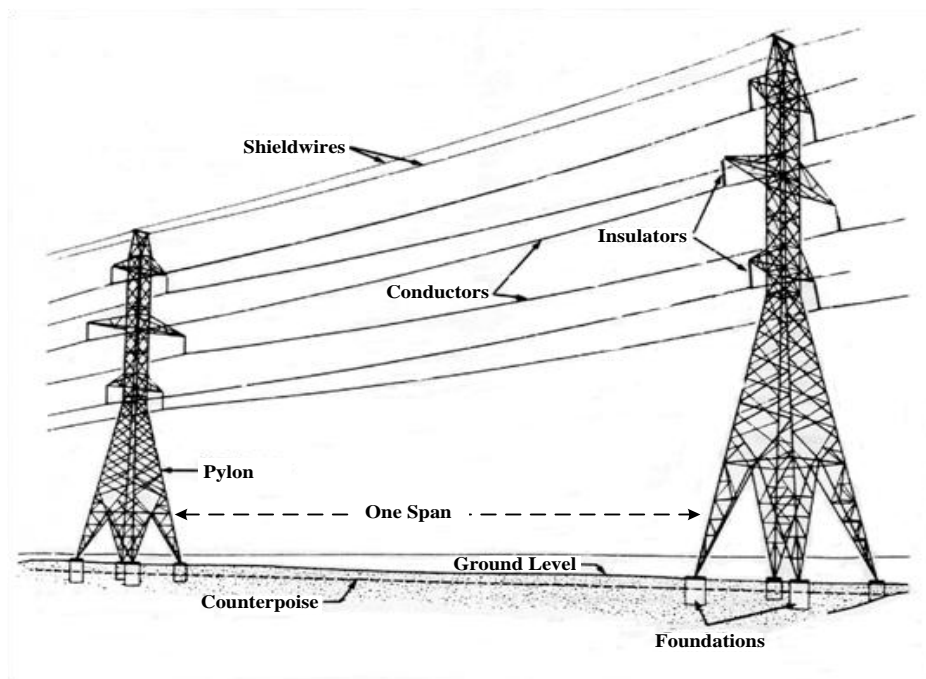
Figure 2.6: Main components of a typical overhead PL network.

Conductors

Conductors provide electrical circuits between supply and user points. These conductors vary in size according to the rated voltage and the number of conductors strung on a pole depends on the type of circuits that are used. According to the electrical capacity of conductors, they are divided into three types: transmission line, sub-transmission line, and distribution line. Normally, a transmission line delivers high voltage current in the range from 138 kV to more than 500 kV and a sub-transmission line medium voltage between 34.5 kV and 161 kV. A distribution line delivers low voltage current in the level of less than 34.5 kV and is used mainly for distributing electricity to public customers. Copper, aluminum and steel are usually used for the conductor material. Since copper is plentiful in nature, its cost is comparatively low, so it is very commonly used for overhead line conductors. Aluminum conductors are also popular due to their light weights. Compared to copper conductors of the same physical size, aluminum conductors have only about 33% of the weight. However, their conductivity and tensile strength is kept relatively weak to 60% and 45%, respectively. Thus, a large width of aluminum conductor is required for the cross section to have the same resistance as copper conductors. Steel conductors are also used because of their high tensile strength (i.e., 3 times higher than that of copper conductor), which are appropriate for a long span construction. However, they are quick to rust, so their endurance is less than that of copper or aluminum.

Insulators

Insulators play an important role in isolating conductors from adjacent conductors as well as from their supporting structure. They are also designed to withstand heavy increases in tension or compression on the corresponding POAs. According to the methods of connecting insulators to conductors, they can be geometrically divided into three categories: post, suspension, and dead-

end insulators. Post-type insulators are vertically or horizontally mounted on the pylon structure and designed to hold conductors with a clamp. This type is effectively utilized for the relatively low voltage transmission lines on the narrow ROWs of city streets. Suspension insulators which have a string of multiple discs are suspended from a pylon and thus allowed for swinging. This type is designed to support high voltage transmission lines by carrying the more weight of the conductors plus the force of the wind. Dead-end insulators are designed to withstand greater stress and strain than suspension insulators. For example, if all the conductors on one side of a span break due to being ice-laden or wind-driven, the insulators are able to retain balance of conductors on the other side of the span. This type of insulators thus permits longer spans as well as high voltage transmission lines.

Pylon

The main role of a pylon is to support conductors along straight stretches of line by hanging the conductors at a safe elevation above the ground. There are a variety of towers in the size and shape to suit various voltage types of transmission lines as well as the terrain to be crossed. The general shapes of pylon are tubular, lattice, and poles which are made of steel, concrete, or wood. For the low voltage lines, the structure is designed to provide a symmetrical conductor arrangement on a single-pole structure, which makes it affordable to build and reliable to operate in the urban area. To support high voltage of transmission lines, pylons have more complicated structures, such as double poles and H-frames.

2.2.2 Related works

Research of the last decade into the field of PL detection focuses on automatic PL scene classification and modeling using 3D point clouds and imagery data. According to the primary

data sources used, the proposed methods can be divided into two categories: (a) 2D image-based and (b) 3D point-based approaches.

The 2D image-based studies apply algorithms to optical images under the assumption that PLs have uniform brightness, linear properties, and are parallel to each other. The method proposed by Yan et al. (2007) began to detect PL candidate pixels based on line detectors using mask and ratio. They traced candidate lines and grouped line segments by linking each segment using a randon transform and a user-driven threshold of angle and distance, and finally applied the Kalman filter algorithm to extract an entire power line. Li et al. (2010) suggested a new method for PL detection from complex and noisy image textures captured by Unmanned Aerial Vehicles (UAVs) through the application of a classic edge detector, the Hough Transform (HT). To reduce background noise and bring out PL edges, a Pulse Coupled Neural Filter (PCNF) was developed for preliminary detection of PLs. Finally, line clustering based on *a priori* information was performed to refine the results of line detection by using a k-means algorithm. The reported approaches based on 2D image analysis strongly depend on image gradients, that is, the contrast of pixel values between PLs and their background. The algorithms are thus sensitive to noise and test regions (i.e., rural versus urban areas), which leads to different contrasts near PLs, thereby decreasing the robustness of results. In addition, due to the lack of 1D (i.e., z-axis) in 2D images, occlusion occurs along the height direction, so it is difficult to detect overlapping PLs.

By using LiDAR data as a primary information source, the 3D point-based approach performs a classification of PL points and the subsequent modeling is based on several unique properties of the LiDAR data and the geometrical characteristics of the PL. An important property of LiDAR data is that it can provide multi-echo information and gives the intensity of the returned laser. This property allows us to roughly separate point clouds into each object class (i.e., PLs, buildings, trees, etc.) based on height and the differences in intensity between the pulses.

Axelsson (1999) proposed a filtering technique for the classification of objects comprising 3D city models. After detecting buildings and ground using MDL criterion and the TIN-based elevation difference, power line points are extracted based on their geometrical properties and data characteristics. In other words, since power lines hanging over the ground surface show linear properties, their points provide multiple echoes derived from the PL and the ground. The results are then refined by isolating the PL points using the Hough Transformation equation. Clode and Rottensteiner (2005) suggested a method for the classification of trees and power lines based on the theory of Dempster-Shafer using only dual return airborne LiDAR data with a point density of about $0.8/m^2$. Three classification cues were used: a first pulse laser intensity image, height differences between the first and last pulse, and a local point density image. The Dempster-Shafer theory was applied to classify input data into one of three classes (i.e., tree, PLs, and others) using the three classification cues. Melzer and Briese (2004) proposed a bottom-up method for reconstructing PLs from LiDAR data. An iterative Hough Transformation was used for extracting line primitives, which are grouped based on a minimum linkage hierarchical clustering method. A PL model was reconstructed using a catenary curve equation whose parameters are estimated using RANSAC. McLaughlin (2006) presents a two-stage method to extract transmission lines from LiDAR data with 1.2-2.4 m point distance on a line: an initial classification based on a Gaussian mixture model, and an estimation of the parameters of the transmission line spans using a catenary curve embedded local affine model. In the initial classification stage, point clouds were classified into three categories using eigenvalue analysis: transmission lines, vegetation, and surface. By using the classification information, the parameters of the catenary curve are initially calculated based on their geometrical relations. Then, the parameters are estimated by fitting the catenary curve to the corresponding PL member points using numerical methods such as a linear squares regression process, thereby reconstructing PL

models. Vale and Gomes-Mota (2007) proposed a new real time solution for data segmentation and anomaly identification algorithms. In each LiDAR sweep, the range data is assigned to one of four different object classes, PLs, obstacles, towers, and ground. If a geometrical mismatch happens due to variations in the laser position, occlusion, or insufficient data resolution, line interpolation occurs by taking into account previous geometrical information. Although the proposed point-based method demonstrated a success rate of more than 72% completeness for the PL extraction rate, its results show an irregularity in data distribution due to the effects of random errors and occlusion, which result in various point density and data gaps on PLs. These sometimes lead to failures in PL modeling completion.

2.3 Building modeling in literature

3D building models are a crucial extension of online mapping services such as Google Earth^{TM} and MS Virtual Earth^{TM} since they provide enriching and interactive visual information that works well with users' eye-brain cognitive pattern interpretations and visualizations. This leads that the photo-realistic 3D building models are used for a variety of applications based on the online mapping platform. For example, environmental planning in support of decision-making (Scherer and Schapke, 2011, Yu et al., 2010), noise modeling for telecommunication operators (Wagen and Rizk, 2003), hazard mitigation for risk management (Hu and Augenbroe, 2012), visualizations for tourists (Glander and Dollner, 2009), interactive measurement for surveyors (Liang et al., 2011), magnetic interferences, flight simulations, cartography and map revision, transportation planning, disaster assessment and so on. However, despite the growing demand for 3D building models, achieving the rapid and accurate creation of realistic 3D models from major data sources such as aerial/space images and LIDAR data remains a challenge. This is mainly

caused by limitations of data representation as much of the data used includes systematic and random errors caused in part by uncalibrated sensor systems, scene complexity, etc. It has been pointed out comprehensive reviews on the extraction of objects including buildings from image and LiDAR data by many researchers (Mayer, 2008; Rottensteiner, 2009; Haala and kada, 2010). Based on the reviews, this section explores research trends in the building reconstruction, especially regularization of noisy building vectors, from LiDAR data as a main data source during the last decade.

Under the assumption that off-terrain points are detected, the modeling process of building objects begins with isolating building points, called building blob detection or building localization. Since the building rooftops are comprised of the combination of planar facets above terrain surface, most of building localization is subject to a plane detection based on e.g. RANSAC (Tarsha-Kurdi et al., 2008) and a height difference between neighboring plane patches (Tarsha-Kurdi et al., 2006). As LiDAR data with high point density in the range of up to 20 points/ m^2 emerge, for example, in the corridor mapping, the building blob detection techniques have been easy to be applied and produce high quality results. By using planar roof primitives as modeling cues, building rooftop modeling is done by establishing topological relations between planar patches and optimally fitting model hypotheses to the primitives. Two different basic modeling schemes, parametric and generic modeling, are mostly used to represent rooftop shapes.

The parametric building model uses a fixed set of standard model types, such as gable and hip roof, in which the topological relations of planar patches are pre-parameterized but their geometry is unknown. Then, the extracted modeling cues are matched to predefined building types and geometric properties of the models such as scale and orientation are estimated as the output. Since this approach relies on the bulk of the data rather than on a subset of building segments, the representation of complex building shapes is also restricted to a composition of

predefined building parts. On the other hand, generic building models allow for the high variation of building types. This means that the parametric relations of planar segments and geometry of rooftop shapes are unknown. Thus, this approach provides high adaptability to complex building types. However, due to the minimum use of a priori knowledge of building shapes, the modeling quality depends heavily on the detection processes of modeling cues. In the automatic modeling approach, it is difficult to completely reconstruct rooftop structures including detailed rooftop components such as chimneys and ventilation fan. Thus, the two modeling techniques are usually performed under the fact that microstructures on the rooftop are not required to be modeled.

In the past few decades, it has been pointed out by many researchers that the *regularization* of noisy building boundaries is an essential step for the generic building modeling. The process of regularization, known as a *line simplification*, is mostly used to extract the boundary vectors by avoiding fragmented line segments and redundant vertices. Moreover, geometric conditions such as symmetry, parallelism, and perpendicular are imposed to the boundary vectors during the regularization process. Various techniques related the regularization of building vectors have been proposed in the literature. In here, according to regularization criterions used, representative studies are categorized and then surveyed in detail. Typical limitations in the studies are not to deal with arc-shape of polygon and their outcomes are also sensitive to a point density which is shown along the boundary lines.

Douglas-Peucker-based simplification

The classical Douglas-Peucker (DP) algorithm has been widely recognized as the most visually effective line simplification algorithm (Ramer, 1972). This simple algorithm starts by constructing a polyline with edge segments, which link *a priori* intial vertices selected from edge points. The process recursively discards the subsequent vertices whose distance from the initial

polyline less than $\zeta > 0$ allowing distance tolerance. It accepts the vertices as part of the new simplified polyline if their distances from the line are greater than ζ, where it then becomes the new initial vertices for further simplification. However, the performance of DP fully depends on ζ and intrinsic topological errors such as a self-intersection are found, which is later improved (Ebisch, 2002; Wu and Marques, 2003). Cho et al. (2004) simply applied the DP algorithm to an urban set of LiDAR data, which results in producing well-simplified boundary lines without considering geometric constraints between the lines. Shan and Lee (2002) and Zhang et al. (2006) extended the line simplification by imposing simple geometric constraints to the polylines derived from the DP. After computing two main orientations of a building, the most of outlines are forced to be parallel and/or orthogonal based on the dominant orientations. It assumes that a building polygon is basically formed as a rectangular shape, so consecutive polylines are perpendicular to one another (Alharthy and Bethel, 2002; Ma, 2005). However, due to the simplicity of approaches, their capability is sensitive to the presence of data noise along building boundaries. In addition, Lach and Kerekes (2008) and Lee et al. (2011) adopt a sleeve-fitting algorithm (Zhao and Saalfeld, 1997), which uses angle tolerances instead of distance tolerance for simplifying irregularly distributed polylines.

Least squares adjustment with geometric constraints

The initial boundaries can be iteratively rectified and fitted well to boundary points as well as imposed by geometric constraints such as linearity, connectivity, and orthogonality based on the least squares adjustment. Ameri (2000) introduced the Feature Based Model Verification (FBMV) for regularizing 3D polyhedral building shapes from DSM and imagery data. During the regularization process, linearity for straightening consecutive lines, connectivity for establishing topology between adjacent lines, and orthogonality for imposing the orthogonal property to

neighbouring lines as well as co-planarity for growing a polygon are used as constraints. Then, the weighted least squares minimization is adopted by incorporating the constraints in order to produce a good regularized description of building rooftop polygons. Sampath and Shan (2007) parameterized a regular building model by the coefficients of a rectangular shape based on a least squares adjustment with only a perpendicular constraint. This results in an over-regularized rooftop shape in the case of building polygon with more than two directions. Xu et al. (2010) and Lee et al. (2011) consider the regularization with less use of orientation constraints as fixing the dominant orientations limits the shapes of building polygons to rectangular shapes. However, this often causes the generation of redundant line segments due to the irregular distribution of boundary points. With a similar approach, Neidhart and Sester (2008) propose a graph-based vertex reduction method that is used to find a polygon with a minimum perimeter, while preserving the geometric properties such as orthogonality of consecutive polylines. The final outlines with a set of straight lines are approximated based on RANSAC and least squares adjustment.

MDL-based verification

According to Rissanen (1999), the basic concept of Minimum Description Length (MDL) theory is to find the most probable model with a global maximum likelihood in the set of possible model classes. Weidner and Förstner (1995) adopted the MDL concept to regularize noisy building outlines extracted from high-resolution DSM. After determining the building boundary points, four consecutive points are selected to be the local unit of the line simplification. With this local point set, ten different hypothetical models are generated with respect to regularization criteria. The criteria are defined by moving two middle points, removing one of the middle points as well as imposing orthogonal property on the consecutive lines. As a result, the regularization

process produces a good approximation of building outlines, but there are several limitations. First, by generating many hypotheses at every vertex, a high computational cost is required. Second, since line simplification is locally performed, the method may produce different results according to the starting vertex. Moreover, due to the local adaptive regularization, it is difficult to achieve a global regularity for entire polylines. Thus, an additional optimization step which globally imposes the geometric constraints to the building model should be involved. Jwa et al. (2008) extended the approach by solving some limitations, resulting in the generation of a global optimal building polygon. Three geometric parameters of building vectors; line directionality, inner angle, and number of vertices, are directly employed in the MDL framework. According to regularization rules defined, the parameters are hypothesized, which results in a number of regularizing model hypotheses. A model minimizing the MDL cost function is finally selected as a global rooftop model among them. Similar ideas are also presented by Taillandier and Deriche (2004) in order to simplify the complex building rooftop shapes. From 3D plane primitives, edges of planes are extracted by intersecting all the planes. The possible arrangement of planes is then hypothesized in the form of 3D graph. Topological and geometrical description with respect to the number of planes, edges, vertices, and line direction are also integrated with the Bayesian formulation. The hypothetical rooftop models are therefore verified based on the MDL framework. In performing MDL-based verification, a general problem is that a model with under- or over-regularized form might be selected in the complex building scene. This is normally due to the failure of keeping a balance between regularization terms in the MDL function. To avoid the problems, weight values for each term are required to be adaptively optimized to control inferential power between the terms.

2.4 Airborne LiDAR system overview

Light Detection And Ranging (LiDAR) is an active remote sensing technology. It uses an artificial energy source, a laser, to sense the corresponding targets by measuring time delay between its emission and return pulse. Since the mid 1990s, a global positioning system (GPS) technology has made it possible to determine the position of a person or object with a high degree of accuracy, which has enabled the development of the LiDAR system for the direct measurement of topographical terrain surfaces (Ackermann, 1999). A typical LiDAR system produces 3D positional data in the Cartesian (XYZ) coordinate system by integrating two main measuring equipments: a laser scanning system and a position and orientation system.
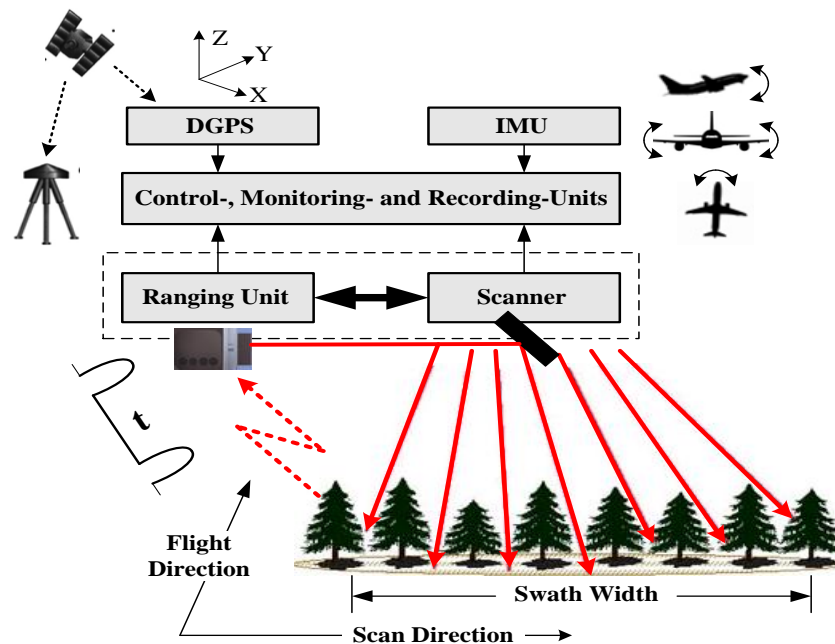
Figure 2.7: The overall diagram of a typical airborne LIDAR system.

As shown in Figure 2.7, each of these systems can be divided into sub-units: a laser ranging and optical scanning unit within the laser scanning system, a GPS, and an inertial measurement unit

(IMU) within the position orientation system. The associated measurements are recorded by a computer unit mounted adjacent to the sensors. For further information, one can refer to literature by Wehr and Lohr (1999), Baltsavias (1999), Shan and Toth (2009), and Geist et al. (2009).

Laser ranging

Laser ranging systems measure the distance between the survey platform and the targets on the ground, and consist of three sub-components: laser transmitter, receiver, and time counter. The laser transmitter continuously emits a number of pulses per second that are normally measured in kilohertz (kHz), called as PRF (Pulse Repetition Rate). Currently, a typical airborne LiDAR systems provided by main manufacturers (Optech, 2013; Riegl, 2013) can generate high PRF up to 800 kHz which leads to a dense point spacing, resulting in the increase of spatial resolution on the ground. However, the PRF is limited by the system's ability to recharge a specific fraction of the pulse's maximum amplitude after emitting a previous pulse. This time length is referred to as pulse duration (pulse width) and its common value is approximately 7 nanoseconds (ns) in most LiDAR systems. The receiver has an optical detector, which senses backscatters from an emitted pulse traveling at the speed of light. The pulse must be returned to the sensor after hitting an object on the ground before the next pulse is emitted, otherwise it will not be recorded. The latest commercial LiDAR system employs photon-counting technology based on single-pulse multi-photon / multi-pulse single-photon detection, which results in the improvement of system performance by increasing the signal reception rate at low-energy.

Scanning system

The primary role of scanning devices is to redistribute laser pulses to cover wider areas with a higher point density. Various scan angles (i.e., Fields Of View), from 40^0 to 75^0, can be adopted

for different mapping purposes. A wider scanning angle reduces the time and costs required for mapping. However, it increases occlusions and error propagations in the range computation towards the edge of scan lines. In typical practical operations, four types of reflective scanning devices are used. They create different scanning patterns on the ground: oscillating mirror, rotating mirror, nutating mirror (palmer scanner), and fiber scanner. The oscillating mirror changes its scan direction at the end of each scan, which yields a zigzag line for a linear scanning pattern. This leads that its operation requires acceleration and deceleration. The rotating mirror and nutating mirror move with a constant angular speed, which produce parallel lines and elliptical shapes (i.e., a non-linear scanning pattern), respectively. This allows for faster scans that produce redundant raging measurements on the same ground area. In the fiber scanner, laser pulses are directly sent into a circular glass fiber array and linearly transmitted to the ground, which forms a parallel scanning pattern. As the scanner uses the small aperture of the fibers without large mechanical movements, it achieves a high scan rate and a high sample point density. However, it requires a very sophisticated calibration procedure.

Positioning and orientation system

Inertial Navigation System (INS) provides high quality navigation information derived from inertial measurements of linear velocity and angular rates in combination with GPS-based positioning techniques. Inertial navigation is defined as navigation using Inertial Measurement Units (IMU) based on Newton's laws of motion. In general, an INS comprises a set of IMUs (i.e., accelerometers and gyros) the platform on which they are mounted, and the computer that performs the calculations needed to transform sensed accelerations and angles into navigation information: position, velocity, and attitude. Gyroscopes measuring the angular rate of the platform with respect to inertial space are divided into two types: mechanical and optical gyros.

Mechanical gyros provide direction according to the angular momentum of a rapidly spinning mass in inertial space analogous to Newton's second law of rotational motion. This device is usually used for strategic military applications or high-accuracy space application, given its accuracy, which is known to be better than 0.0001 °/hr for bias and 50 ppm for scale factor. It is also expensive, compared to the tactical/commercial grade, with bias stabilities in the range 0.1 -

10000°/hr and scale factor larger than 100 ppm (Jekeli, 2001). Optical gyros are operated based on the Sagnac effect, which results in the apparent lengthening or shortening of light propagated in a closed circuit that is rotating with respect to inertial space. The optical gyro is not suitable for the local level stabilization of a platform because it does not use a spinning mass, but it is a valid alternative to the mechanical gyros in a strap-down mechanization in which a platform rigidly attaches to the corresponding reference frame. An accelerometer senses the specific (applied) force. In other words, it does not measure the acceleration associated with free-fall in a gravitational field, but it does sense the reaction, such as the lift provided by a parachute. The high performance accelerometer for military applications has an accuracy of greater than than 1 µg for bias and 2 ppm for scale factor.

The NAVigation Satellite Timing and Ranging (NAVSTAR) GPS is a satellite-based radio-positioning and time-transfer system, designed, financed, deployed and operated by the US Department of Defense (DoD). It was designed as an all-weather, continuous, global radio-navigation system (Wooden, 1985). The GPS satellites have nearly circular orbits with an altitude of about 20,200 km above the earth and a period of approximately 12 sidereal hours. The current constellation (November, 2011) consists of 32 operational satellites (including IIF-1 which is a new generation of updated GPS satellites, launched on May. 2010) deployed in six evenly spaced planes (A to F) with an inclination of approximately 55° and spacing of 60° intervals along the equator (http://tycho.usno.navy.mil/gpscurr.html). The GPS satellites basically transmit two

microwave carrier signals, L1 (1575.42 MHz) and L2 (1227.60 MHz), derived from the fundamental L band frequency (10.23 MHz). In recent years, L5 frequency (1176.45 MHz) for civilian-use signals has been made available to the IIF satellite according to the GPS modernization process, which enhances reliability in receiving GPS signals. The signals carry navigation messages, which include satellite clock corrections and ephemeris and pseudorandom noise (PRN) codes. The PRN codes are divided into various types: Coarse/Acquisition-code (C/A-code), Civillian L2-code (L2C), Precision-code (P-code), and Military-code (M-code). The C/A- and L2C-code are normally used in the Standard Positioning Service (SPS) for civilian use with a noise level range of less than 3 m, respectively. On the other hand, the P- and M-codes are designed to be utilized by the Precise Positioning Service (PPS) for a specialized user such as military personnel with a range accuracy of less than 0.3 m, respectively (Hofmann-Wellenhof et al., 2001).

The GPS/INS performance usually depends on the quality of the GPS measurements because the long-term accuracy of a stand-alone INS is poor, compared to that of GPS. On top of the navigational insufficiency of the stand-alone INS, the GPS positioning errors derived from a signal blockage, multipath, and the effect of the sensor vibration while in motion should be considered. In a practical situation, differential positioning with GPS (DGPS) is to be performed by simultaneously collecting data at two stations, a base and a rover, from each satellite to obtain better GPS/INS navigation information. The benefit of the differential technique is that it facilitates the cancellation of common errors, such as the satellite-dependent and receiver-dependent errors. For example, a satellite clock error is considered a satellite-dependent error and can be removed by the single-difference (SD) mode. A receiver clock error and inter-channel biases, which receiver-dependent errors are eliminated based on the double difference (DD) mode. Table 2.1 shows the parameters characterizing a typical topographic LiDAR system. The next

sections discuss the fundamental formulations related to airborne LiDAR mapping, and error sources when producing 3D positional information.

Table 2.1: Characteristics of a typical topographic LiDAR system

Specification	*Typical values*
Laser wavelength	700 - 1400 nm, near-infrared
Pulse repetition rate (PRF)	~ 800 kHz
Pulse energy	100s μJ
Pulse width (Pulse duration)	~ 7 ns
Beam divergence	0.25 – 2.0 mrad
Scan angle (or Field Of View)	40° – 75°
Scan rate	25 – 90 Hz
GPS frequency	1 – 10 Hz
INS frequency	200 – 300 Hz
Operating altitude	80 – 3500 m (6000 m maximum)
Footprint size	0.25 – 2.0 m (at 1000 m altitude AGL)
Number of returns	~ 4 or unlimited (full waveform)
Ground spacing	0.5 – 2.0 m
Vertical accuracy	5 – 30 cm (at 1000 – 3000 m altitude AGL)
Horizontal accuracy	1/5500 – 1/2000 of flight attitude (m/AGL)

2.4.1 Related fundamental formulations

Figure 2.8 depicts the configuration of the main components of airborne LIDAR systems and the principle of laser point positioning derived from the LIDAR geo-referencing equation described in Equation 2.1 (Toth 2009; Habib 2009).

$$\vec{X}_G = \vec{X}_0 + R_b^m \cdot \vec{P}_G + R_b^m \cdot R_{lu}^b \cdot R_{lb}^{lu} \cdot \vec{\rho} \qquad (2.1)$$
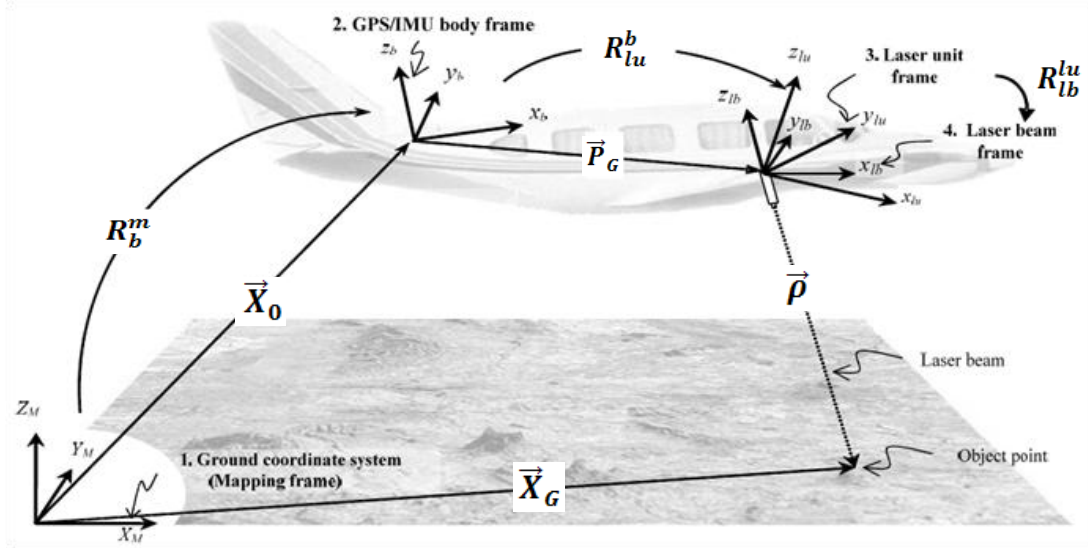
Figure 2.8: The schematic diagram of airborne LIDAR system's configuration and the principle of laser point positioning (Bang 2010).
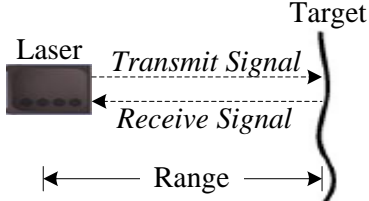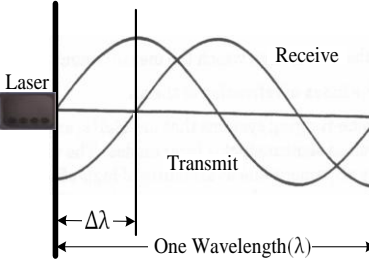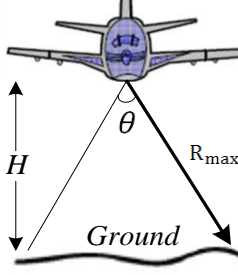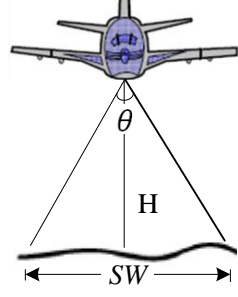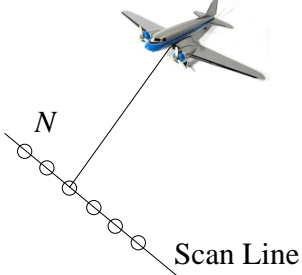
In general, measurements derived from the main components are navigation solutions including position and attitude information derived from the GPS/INS integration, and range information produced from a laser unit. By incorporating the measurements into the LIDAR equation, the positional information of the laser beam footprint is estimated based on the shift and rotation of the associated vectors over the corresponding coordinate systems, where the coordinate frames used in the LIDAR equation are comprised of a ground coordinate frame and three local coordinate frames (i.e., IMU body frame, laser unit frame, and laser beam frame). The LIDAR equation is based on the summation of three shift vectors and the three corresponding rotations: (a) $\vec{X}_0$ between the origin of the mapping frame and the center of IMU body frame, (b) $\vec{P}_G$ (lever-arm) between the phase center GPS antenna and the center of IMU body frame, (c) $\vec{\rho}$ (laser range) between the laser firing point and its footprint, (d) R_b^m between the mapping and IMU body frame,

(e) R_{lu}^b between the IMU and laser unit frame, (f) R_{lb}^{lu} between the laser unit and laser beam frame. As a result, the LIDAR system determines the positional information of the laser beam's footprint $\vec{X}_G$ over the ground based on the spatial relationship between the used sensors.

In the previous research, some fundamental relations and formulations are introduced as major factors in the airborne laser scanning (Baltsavias, 1999; Shan and Toth, 2009). Values derived from these formulations can be used as the main input for the whole airborne laser mapping task which is related to the range from planning a flight mission to obtaining a final product. At the level of flight planning, after selecting the appropriate LIDAR system, the main parameters such as flight altitude and speed are determined by taking into account the quality of the final product. This is due to the fact that the initial parameters in flight planning can directly affect the positional accuracy and resolution of LIDAR data. For instance, according to the information provided by one popular system manufacturer (i.e., OPTECH ALTM series) at a flight altitude of 1200m, the expected positional accuracy (1 sigma) of the point clouds is approximately 0.6m and 0.15m for the horizontal and vertical planes, respectively. However, if flight height increases to 2000m, the accuracy will be downgraded to 1m and 0.25m. After obtaining LIDAR data based on the customer's accuracy requirements, some factors, including the point density/spacing and the accuracy of point position, are also used as *a priori* information for LiDAR data filtering in order to extract the final products, such as DSM and object models (Pfeifer and Mandlburger, 2009). Table 2.2 summarizes the fundamental relations and formulations of laser ranging and airborne laser scanning.

Table 2.2: Fundamental relations and formulations of airborne laser ranging.

Major Factor		Geometry	Formulation	Description
Laser Ranging	Time Pulse Method	Laser — Transmit Signal — Target; Receive Signal; Range	$R = v \cdot t/2$	R : slant range v: the speed of light t: measured time interval
	Phase Comparison Method	Laser; Receive; Transmit; $\Delta\lambda$; One Wavelength(λ)	$R = (M \cdot \lambda + \Delta\lambda)/2$	M: integer number of wavelengths λ: the known value of the wavelength $\Delta\lambda$: the fractional part of the wavelength=$(\varphi/2\pi) \times \lambda$), where φ is the phase angle
Altitude above Ground		θ; H; R_{max}; Ground	$H = R_{max} \cdot \cos(\theta/2)$	R_{max}: maximum slant range θ: angular FOV
Swap Width		θ; H; SW	$SW = 2H \cdot \tan(\theta/2)$	H: altitude θ: angular FOV
Number of Points per Scan Line		N; Scan Line	$N=F/f_{sc}$	F: pulse rate (pulse repetition frequency, PRF) f_{sc}: scan rate

Point Spacing	Across		Δ_{across} $= \theta/N$ $\cdot H/\cos^2(\theta/2)$	H: altitude θ: angular FOV N: number of points in one scanning line
	Along		$\Delta_{along} = v/f_{sc}$	v: forward speed f_{sc}: scan rate
Point Density			PD $= 1/(\Delta_{across} \cdot \Delta_{along})$ $\approx N/m^2$	N: number of points
Footprint Diameter	Nadir		d_{fp} $= 2r$ $\cdot \tan(\Delta\theta/2)$	$r(\approx H)$: distance between laser sensor and surface $\Delta\theta$: laser beam divergence
	Off-Nadir		d_{fp} $= 2r$ $\cdot \dfrac{\tan(\Delta\theta/2)}{\cos(\beta-\alpha)}$	β: scan angle of the laser beam α: angle between surface normal and vertical
Overlapping Factor			$\xi = 1 - e/SW$	SW: swath width e: flight line separation
Horizontal Accuracy			Better than $1/2000 \cdot H$	H: altitude
Vertical Accuracy			Approximately 15 cm at 1200m 25 cm at 2000m	1 sigma

2.4.2 LIDAR error sources

Since the LiDAR system shows complex and highly interconnected configurations of main sensors (i.e., navigation sensors and laser scanning unit), errors derived from each sensor are correlated, and thus it is difficult to clearly determine the source of those errors through a calibration process. The potential error sources affecting the quality of laser point clouds can be divided into two categories: random and systematic errors. A random error which is assumed to follow the normal distribution is a non-predictable error source and its impact depends heavily on the precision of the measurements provided by each sensor. On the other hand, systematic errors are mainly caused by biases due to the insufficient calibration of individual sensors and misalignment between different sensors. Many studies of the LiDAR error budget were performed early on in its development (Baltsavias, 1999; Schenk et al., 2001; Csanyi and Toth, 2007; Bang 2010) and the summary of these studies is tabulated in Table 2.3 (Toth, 2009).

Random errors

This type of error is propagated to the ground point position according to the law of error propagation derived from the LiDAR equation (Equation 2.1). The impact of random errors should be investigated by examining system measurements such as the position and orientation derived from GPS/INS integration and laser range. A position noise randomly affects both of horizontal and vertical coordinate regardless of flight height and scan angle. However, an orientation error contaminates the horizontal coordinate more than the vertical coordinate and the contaminated amount varies with respect to flight height and scan angle. The laser range error normally affects the vertical component of the point in the nadir region.

Ranging error

The range error is caused by the malfunction and false adjustment of the time counter in measuring the pulse transmission time. The atmospheric effect also affects the distortion of the laser pulse's path. In other words, as a laser pulse travels to the ground and back from its laser unit, the value of the laser range could be incorrectly calculated according to the atmospheric status taking into account air-density and variations of pressure, humidity and temperature. In addition, the degree of the intensity of the laser signal with respect to the reflectivity of the surface influences the range's computation. The error effect is usually corrected based on the intensity-based calibration tables provided by a LiDAR manufacturing company. The effect of the ranging error mainly shows in the vertical point coordinate and increases in the horizontal point component along the scan line.

Scanning angle error

The scanning angle error occurs if an instantaneous angular position of the scan mirror rotation is incorrectly measured. The error leads to an anomaly in the laser beam deflection vector with respect to the encoder, which causes a horizontal and vertical shift of the coordinate of the laser point along the scan direction.

Alignment error between sensors

The alignment error is related to a misalignment (i.e., bias) in two components: offsets and boresight angular. The offsets including the lever arm means translation vectors between the sensor frames related to GPS, INS and laser sensor. The boresight angular indicates rotation angle between the INS body frame and laser frame. The bias in the boresight angular is more critical than that in the offsets. This is because the angular bias unlike linear bias derived from the offsets

produces a non-linear form, and thus provides an unexpected and large impact on the point position according to a flight altitude.

Error in navigation solution

This error is derived from the navigation solution introduced by the GPS/INS integration in determining the position and attitude of the sensor platform. The position error is caused by anomalies in GPS measurements, which are caused by cycle slips, multipaths, tropospheric and ionospheric errors, integer ambiguities, and so on. The ground coordinates of the measured LIDAR points are directly corrupted by the error, resulting in a discrepancy between adjacent strips. The accuracy of IMU measurements derived from the attitude of the aircraft is mainly affected by initialization errors, mechanical misalignments, and gyro drifts. To mitigate errors in the navigation solution, proper planning of the airborne survey as well as careful calibration of sensors is required. For example, it is important not to use very long baselines (i.e., more than 25 – 30 km) for the Differential GPS solution in order to reduce distance-dependent errors.

Miscellaneous Errors

Besides the aforementioned main error sources, there are minor error types which should also be considered in order to improve the positional accuracy of LiDAR data. A time synchronization error occurs in the process of fusion of measurement data derived from the navigation and laser sensors. Fluctuation of flight also causes complex 3D position errors of laser points. An error in the coordinate/datum conversion (about 1-5 cm) can occur when LiDAR data are converted into user-preferred coordinate systems, like NAD83 being based on a GRS80 ellipsoid after acquiring LiDAR data based on a WGS84 ellipsoid. A mounting error is related to the rigidity of the

mounting of sensors such as IMUs and laser sensors, and leads to orientation errors. During the

flight, some unexpected bending forces on the carrying plate of sensors can cause mounting errors.

Table 2.3: Major error sources and their impact on the accuracy of LiDAR point positioning (Toth 2009).

Components	Errors	Typical values
Navigation solution (GPS/INS)	Errors in sensor platform position (shift errors)	σ_X, σ_Y: 2 - 5 cm σ_Z: 4 - 7 cm
	Errors in sensor platform attitude	σ_v, σ_φ: 10 - 30 arcsec σ_k: 20 - 60 arcsec
Laser sensor calibration	Range measurement error	σ_r: 1 - 2 cm
	Scan angle error	σ_β: 5 arcsec
	Error in reflectance-based range calibration	[-20 - 10] cm
Inter-sensor calibration	Boresight misalignment between the INS body and laser sensor frames (shifts and angular errors)	σ_{Xb}, σ_{Yb}, σ_{Zb}: <1 cm σ_{vb}, $\sigma_{\varphi b}$: 10 arcsec σ_{kb}: 20 arcsec
	Error in measured lever arm (vector between GPS antenna and INS reference point)	σ_{Xa}, σ_{Ya}, σ_{Za}: < 1 cm
Miscellaneous errors	Effect of beam divergence (footprint)	< 5 cm
	Terrain and object characteristics	-
	Time synchronization	-
	Coordinate system transformations	-
	Atmospheric refraction	-
	Sensor mounting rigidity	-

CHAPTER 3

3D building modeling:
Implicit geometric regularization of noisy
building boundary vectors

This chapter introduces an implicit geometric regularization method for 3D shape reconstruction of building rooftops from noisy airborne LiDAR data. In here, the regularization is a process in which a model deformed by noises is refined by considering geometric regularities that indicate dominant knowledge of rooftop shapes and their patterns such as parallelity, collinearity, and orthogonality. The regularities are also implicitly represented to rooftop models by a set of rules defined during the regularization process without explicitly using hard constraints. The regularization process is performed based on Minimum Description Length (MDL) theory and its cost function is designed by two terms, model closeness and model complexity. Thus, a proper trade-off between two selection criteria is required for generating an optimal model which becomes a goodness-of-fit model with simple and regular shape.

3.1 Introduction

In recent years, as the use of electric energy rapidly increases in urban area, the installation of new PLs has been urgently required. However, this leads to the increase of electromagnetic field of PLs near residential areas, so that potential adverse health effects from the magnetic filed have become social issues. For the public safety in PL corridor area (ROW), as aforementioned in Chapter 2, various regulations related to for example a minimum distance between PLs and buildings at a certain PL voltage are already formulated all over the world. For this, an accurate 3D geometric representation of buildings plays an important role for the effective risk analysis on magnetic interferences to residence buildings based on the regulations. Modeling building rooftops (shape reconstruction) focuses on the physical quality of the reconstructed model elements such as boundary lines, polygons, and volumes, so that local shape details should be captured (Cheung et al., 2002). However, despite the demand for 3D building models, achieving accurate description of buildings from major data sources captured through passive or active sensors such as aerial images and LiDAR data is still a challenging work. This is mainly due to the limitations of data representation as much of the data are normally corrupted by various error sources such as systematic and random errors as well as scene complexity. Thus, in the image data, occlusion of rooftops or their parts by neighbour objects and variation of brightness due to the effect of shadows, noise, and low contrast usually occur. LiDAR point clouds also show irregular distribution with varying point density and data gaps, which cause confusions in interpreting detailed rooftop structures. In spite of aforementioned limitations, a lot of research efforts have been made to reconstruct photo-realistic 3D building models from the major data sources and their comprehensive reviews were provided by Rottensteiner (2009) and Haala and Kada (2010).

In practice, using LiDAR data for this thesis, modeling building roof structures begins with geometric primitives detected as modeling cues which are derived from off-terrain points. Where, the off-terrain points are separated from on-terrain points using an appropriate filtering process. The primitives mean a quantitative symbolic description transferred from qualitative knowledge stored in raw data such as spatial behaviour of data, which are usually composed of corners, lines and planes (Ameri, 2000; Belgiu and Thomas, 2013). As a result, the whole shape of building rooftops is mostly approximated by establishing topological and geometric relationship between primitives detected. However, as the primitives are inevitable to be corrupted by noisy data, reconstructing fine building rooftop models becomes a very difficult task. As mentioned in the previous chapter, based on the use of the primitives, there are two basic modeling schemes, parametric and generic modeling. The parametric modeling is performed by fitting a candidate model derived from a fixed set of standard model types such as gable and hip shape to the associated primitives. In this approach, the topological relations of primitives are pre-parameterized and their geometry is only unknown. However, there is a limitation in representing complex building shapes if they are not available in a database of predifned building types. On the other hand, reconstruction based on the generic modeling allows us to represent high variation of building types. That is, as parametric relationship between primitives and their geometry are unknown, it is possible to express variation in the structure of objects based on a set of geometric parameters that is not fixed. However, there is a principal disadvantage of generic modeling compared to parametric modeling. Due to the minimum use of *a priori* knowledge of building shapes, the modeling quality with a high level of detail is heavily subject to the result of detection of primitives, resulting in the increased sensitivity to data noise.

In the generic modeling approach, it has been pointed out by many researchers that regularization is essential step for the recovery of rooftop shapes with regular patterns from noisy

primitives (Weidner and Forstner, 1995; Ameri, 2000; Ma, 2005; Sohn and Dowman, 2007; Lee et al., 2011; Sohn et al., 2013). The regularization is a process in which a model deformed by noises is refined by considering geometric regularities that indicate dominant knowledge of rooftop shapes and their patterns. Most of building rooftops modeled as a wire-frame structure (i.e., CAD model) shows specific regularities between line or plane segments such as parallelity, collinearity, and orthogonality. Besides, rooftop boundaries should be delineated by avoiding redundant fragmented line segments and vertices (Brunn et al., 1995). Consequently, the final shape of building rooftops becomes a goodness-of-fit model with simple and regular shape.

In this chapter, we adopted the data-driven generic modeling to recover detailed rooftop components from airborne LiDAR data with the purpose of performing the precise risk analysis in ROW. For its regularization process, a new method, implicit geometric regularization, is proposed to achieve desired results of shape reconstruction of building rooftops from noisy primitives. The implicit means that geometric regularities are represented to rooftop models by implicitly determining (data-driven) a set of rules during the regularization process instead of explicitly using hard constraints. In the literature, many researchers have introduced different regularization techniques. However, these research efforts have gained only limited success in constrained environments requiring many pre-specified thresholds to control the geometric regularity or mainly focusing on minimising residuals between boundary observations and models. Most of problems considered in this chapter will be solved by performing the proposed regularization process in the Minimum Description Length (MDL) framework, resulting in the generation of polyhedral-like building models with geometric regularities.

3.2 Motivation

It is discussed that a coarse generic rooftop model derived from noisy primitives is to be refined based on a set of regularization rules defined. Where, the used term, model, denotes the hypothetical description of a real object. To rectify the coarse model, a model selection procedure for determining which model is a best description of given data is required. It is also inevitably confronted with problems on what is an acceptable degree of models in representing a dominant part of data. If a model which only fits well to the data is selected, its over-fitting is unavoidable due to measurement errors, called model selection problem. This implies the need for hypothetical representations capable of characterizing global and universal description for the given data (Georgeff and Wallace, 1985). In the case of prismatic modeling, a set of hypotheses with regular shapes is pre-determined by using limited model parameters, so that the model selection problem is manipulated by fitting each hypothesis to the corresponding primitives based on the criterion function. However, in the generic modeling, as the set of hypotheses is not available, a set of possible hypotheses in the different forms, instantiation (example), is required to solve the model selection problem caused by the regularization process.

In this study, primitives used for the generation of instantiations are edge segments which are derived by a successive chain of noisy boundary points. Related concerns are that sequences of primitives show very irregular forms and too redundant edge information exists. In order to deal with these issues, model selection criteria should be defined in the regularization framework. The first useful criterion is related in measuring the degree of how to fit well a model to data, goodness-of-fit, which can be formulated based on the principle of maximum likelihood. The maximum of likelihood is achieved when the observed sequence is represented by using as many parameters as possible (Myung, 2003). However, the criterion only following maximum likelihood principle definitely fails to produce the desired result due to the over-fitting problem.

The most common way to correct the problem is to adopt a combined criterion by adding a term of model complexity. This is motivated by Ockham's razor, a simple explanation of the facts is better than a complex one (Hansen and Yu, 2001). Therefore, a proper trade-off between two selection criteria is required for generating an optimal model which becomes the higher goodness-of-fit model to the corresponding data and at the same time the simpler description with small number of model parameters.

Based on the two selection criteria, the theory of MDL is commonly used as a generic solution to solve the model selection problem (Grunwald, 2005). The most benefit taken from the MDL-based regularization is that it is not to require explicit constrains using pre-specified thresholds in imposing geometric regularities on the model. Weidner and Förstner (1995) adopted the theory of MDL to regularize noisy building outlines extracted from high-resolution DSM using MATCH-T. The used hypotheses that were created in accordance with the defined rules of hypothesis generation were verified using a MDL cost function which is designed based on the two selection criteria. An optimized model was finally selected among a set of hypotheses if it minimizes the MDL cost function. Although the method was successfully applied for the building shape regularization, two major limitations are observed; (1) locality and (2) limited encoding scheme for the model complexity. First, since the procedure of optimal model selection is conducted over a local sequence of points, the regularization results are subject to the starting local point set and their geometric regularities are not achieved in the entire solution space. Second, as the model complexity is only governed by the number of the vertices of hypotheses, a hypothesis with the same number of vertices and different shape might be also selected as an optimal model. To overcome the limitations, this study that is motivated by the study of Weidner and Förstner (1995) which is discussed in detail in the later section proposed a newly required modeling regularization scheme in the MDL framework. The following sections look inside the

proposed MDL-based regularization of noisy building vectors and give detail discussions on its formulations.

3.3   3D prismatic building modeling

In this section, the proposed method focuses on shape reconstruction of flat rooftops, called prismatic building rooftop model, which is parallel to the ground level and its 3D vertices are placed at the same height. Figure 3.1 schematically represents the workflow of regularization process for prismatic building modeling from noisy building outlines.
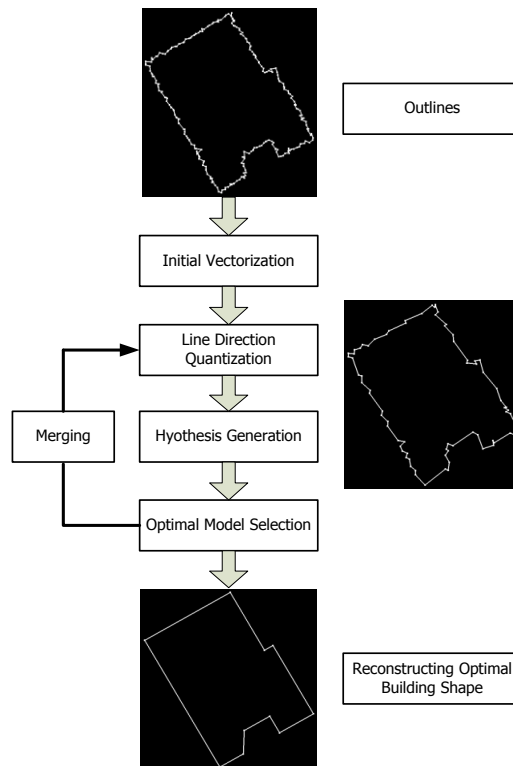
Figure 3.1: The schematic diagram of the proposed regularization process for prismatic modeling of building rooftops.

3.3.1 Mathematical formulation of MDL

The MDL theory has its root in measuring information for communication channel introduced by Shannon (1948) and finding the best prediction for statistic and inductive inference proposed by Solomonoff (1964). Due to the uncertainty of the information, it can be converted to a probability of occurrence. Let *P(x)* be the probability of occurrence by random selection of $x \in \Re$, the information, *I*, of *x* can be represented as:

$$I(x) = \log_2 \frac{1}{P(x)} = -\log_2 P(x) \tag{3.1}$$

Rissanen (1983 and 1999) developed the MDL principle for the optimal model selection based on several important aspects such as the use of no *a priori* knowledge and the inference of hypothetical model classes instead of a single specified model. The basic concept of MDL is that an optimal model is selected by minimizing a computable description length (DL) with a bit unit, which consists of two terms; model closeness (i.e., goodness-of-fit) and model complexity. The computation can ultimately provide a practical advantage that avoids the search of an appropriate test statistic for a validation process (Barron et al., 1998). The issue on how to express the MDL terms in the mathematical form can be derived from a Bayesian framework (Vitanyi and Li, 2000), such that

$$P(H|D) = \frac{P(D|H)P(H)}{P(D)} \tag{3.2}$$

Given a hypothesis *H* and observed data *D*, $P(H|D)$ denotes the posterior probability which is a conditional probability of *H* on *D*. $P(D|H)$ means likelihood for *D* given *H*. $P(H)$ and $P(D)$ is a

prior probability of H and marginal probability of D, respectively. By taking the negative logarithm at the both side of Eq. (3.2), it is written as

$$-\log_2 P(H|D) = -\log_2 P(D|H) - \log_2 P(H) + \log_2 P(D) \tag{3.3}$$

At this points, maximizing $P(H|D)$ in the Bayesian framework is equivalent to minimizing the negative log probability $-log_2 P(H|D)$. As a hypothesis testing is relatively performed in the same data domain, the term $log_2 P(D)$ becomes a constant value and can be ignored. Comparing to the Bayesian framework, it also turns out that prior information for $P(H)$ is not required in the MDL framework. Therefore, a total description length $\mathcal{L}_{tot}$ can be formulated by the summation of two terms, $-log_2 P(D|H)$ and $-log_2 P(H)$, such that

$$\mathcal{L}_{tot} = \lambda \mathcal{L}(D|H) + (1-\lambda)\mathcal{L}(H) \tag{3.4}$$

The first term $\mathcal{L}(D|H)$ indicates model closeness between H and D, which measures the degree of model suitability in the given data D and quantified by $-log_2 P(D|H)$. The second term $\mathcal{L}(H)$ expresses the model complexity of characterizing a global representation using a set of model parameters and quantified by $-log_2 P(H)$. λ and $1-\lambda$ are weight values for balancing the model closeness and the model complexity. Assuming that an optimal model representing the data is the one minimizing its description length, the model selection process allows a model H to be converged to the optimal model H^* by achieving a good trade-off between the two terms as follows:

$$H^* = \arg\min_{H \in \Phi} \{\lambda \mathcal{L}(D|H) + (1-\lambda)\mathcal{L}(H)\} \tag{3.5}$$

Development of model closeness and model complexity

The first term, model closeness, is optimized for the good data attachment to the corresponding model. As the data $D = \{x_1, \dots, x_n\}$ representing n measurements usually exhibits the irregular distribution due to random errors, the measurement errors can be assumed to be following a Gaussian-distribution $x \sim N(\mu, \sigma^2)$ with expectation μ and variance σ^2, and its density function $P(x) = \frac{1}{\sigma\sqrt{2\pi}} e^{-\frac{(x-\mu)^2}{2\sigma^2}}$. By using the statistical model of data, the degree of fit between a model and data can be measured by $L(D|\mu, \sigma^2)$, and then the term of model closeness becomes in the form:

$$
\begin{aligned}
L(D|\mu, \sigma^2) = -\log_2 P(D) &= -\left(\log_2 e^{-\frac{\sum(x-\mu)^2}{2\sigma^2}} + n\log_2 \frac{1}{\sigma\sqrt{2\pi}}\right) \\
&= \frac{1}{2\ln 2} \sum \left(\frac{x-\mu}{\sigma}\right)^2 + n\log_2 \sigma + \frac{n}{2}\log_2 2\pi
\end{aligned}
\tag{3.6}
$$

Where, μ and σ denote *a priori* information with respect to a PL model *M*. In the given *D*, the first criterion is determined by minimizing Eq. (3.6) with respect to μ. If all the hypotheses are assumed to have the same σ, the last two terms as constant values can be ignored. This is because they are independent on μ. Thus, the term of model closeness $\mathcal{L}(D|H)$ is to be simply rewritten as $\frac{\Omega}{2ln2}$. Where, Ω denotes the weighted sum of the squared residuals between φ and D, $[D - \varphi TPD - \varphi$ in the matrix form.

$$
\mathcal{L}(D|H) = \frac{\Omega}{2\ln 2}
\tag{3.7}
$$

The second term, model complexity, is related to the degree of shape complexity and its associated term of model complexity is composed of three geometric factors;

- the number of vertices N_v

- the repeatability of identical line direction N_d

- the quantized inner angle transition $N_{\angle\theta}$

By using the three factors, an optimal model is chosen if its polygon vectors have smaller numbers of vertices, as many as possible identical line direction, and smoother or more orthogonal inner angle between adjacent lines.

The probability for N_v can be formulated from that a vertex is randomly selected as a member point of a model and then $P(v) = \frac{1}{N_v}$. Its description length becomes $log_2(N_v)$ based on Eq. (3.1). Since the optimal model has the number of minimum vertices, that is no-redundant vertices, N_v', its description length is to be $N_v'log_2(N_v)$. Similarly, the probability for N_d, P(d), can be $\frac{1}{N_d}$ and its description length is $log_2(N_d)$. By considering the required number of polylines' directions N_d', information for the line directionality is measured by $N_d'log_2(N_d)$. In this study, line directions $\theta_i = \{0° \leq \theta_i \leq 180°\}$ is quantized by eight directions $\{\theta_i: i=1, ... , 8\}$ based on Compass Line Filter (CLF) suggested by Sohn et al. (2008) as shown in Figure 3.2. Note that the first orientation of CLF is the horizontal direction, and from which the others are subsequently displaced at a constant angle equal to $\Delta\theta$ (i.e., 22.5°). Given line segments belonging to each section of CLF, the representative direction θ_i^{REP} is calculated using lines' length as a weight.

Lastly, we also use the angle formation of CLF for the quantization of inner angles. An inner angle $\angle\theta$ at two consecutive line vectors is quantized by assigning a certain penalty value to one

of a set of angle range specified. As depicted in Eq. (3.8), the penalty values $\gamma_{i=0,1,2}$ are heuristically determined to have the minimum value of 0 (i.e., favoured regularity) if $\angle\theta$ closes to $90°$ or $180°$, while the maximum value of 2 (i.e., un-favoured regularity) is assigned to the very acute inner angle. This is because the occurrence of acute inner angles at the two consecutive building vectors is rare in practice. Therefore, the probability for $N_{\angle\theta}$ can be derived from that an inner angle at a vertex is located in one of quantized angles and then $P(\angle\theta) = \frac{1}{N_{\angle\theta}}$, and its description length is $log_2(N_{\angle\theta})$. In the optimal model, the cost imposed by penalty values $N'_{\angle\theta}$ is $\sum_{k=1}^{N'_v} \gamma_{i=0,1,2}$ and the description length for the inner angle transition is to be $N'_{\angle\theta} log_2(N_{\angle\theta})$.

As a result, the description length for term of model complexity $\mathcal{L}(H)$ is obtained by the summation of three geometric factors as shown in Eq. (3.9).

$$\gamma_{i=0,1,2} = \begin{cases} 2 & \text{if } 0° < \angle\theta \le 11.25° \\ 1 & \text{if } 11.25° < \angle\theta < 78.75°, 101.25° < \angle\theta < 168.75° \\ 0 & \text{if } 78.75° \le \angle\theta \le 101.25°, 168.75° \le \angle\theta \le 180° \end{cases} \tag{3.8}$$

$$\mathcal{L}(H) = N'_v log_2 N_v + N'_d log_2 N_d + N'_{\angle\theta} log_2 N_{\angle\theta} \tag{3.9}$$
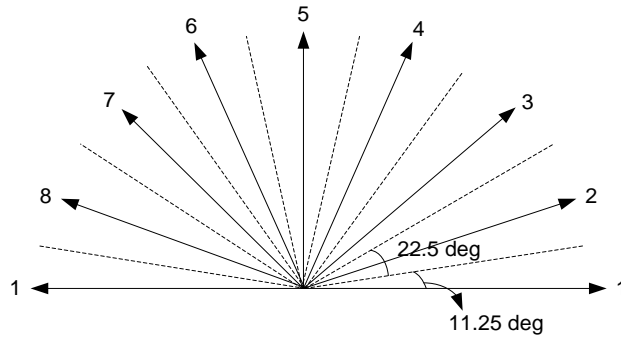
Figure 3.2: Illustration of CLF: A set of quantized line directions with $22.5°$.

3.3.2 Initial vectorization

In the step of initial vectorization, after ordering building boundary points by using a modified convex-hull method, an initial building outlines are reconstructed with linked edge segments obtained by Douglas-Peucker algorithm (Douglas and Peucker, 1973).

3.3.3 Line direction quantization

Orientations of polygon slopes are quantized using CLF (Figure 3.2). All line directions $\{\theta\}$ are measured by $x sin\theta - y cos\theta = d$ and assigned into one of eight CLF numbers, where θ indicates the angle between a line segment and *x-axis*, and d is the line distance from the origin. Finally, the representative line directions with respect to each CLF number are calculated by weight-averaging cumulative directions belonging to the same CLF number.

3.3.4 Hypothesis generation

For each vertex, many regularizing model hypotheses are generated in four different ways. As illustrated in Figure 3.3, A Floating Line (FL) can move along the Guiding Line (GL) passing through FP and GP by replacing the FL's direction with CLF's ones. By intersecting the FL and GL, a new vertex is computed for hypothesizing a regularized model.
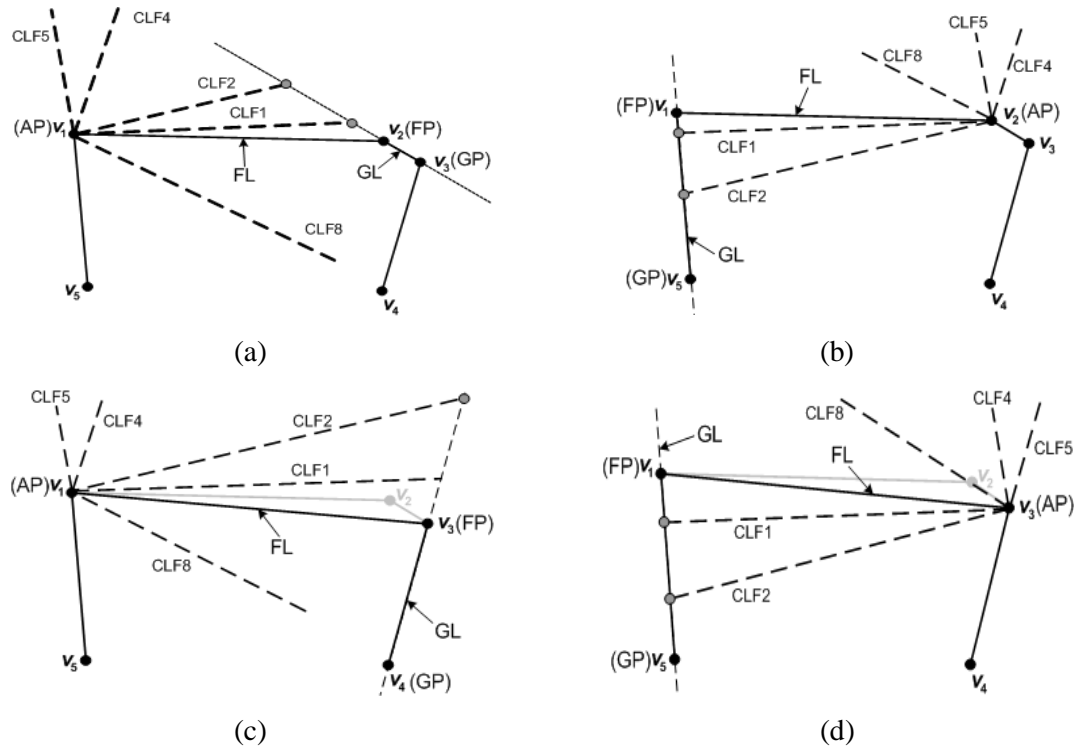
Figure 3.3: The possible alternative hypotheses at three points (AP: Anchor Point, FP: Floating Point, and GP: Guiding point) based on Compass Line Filter (CLF): (a) by moving V_2, (b) by moving V_1, (c) by eliminating V_2 and moving V_3, (d) by eliminating V_2 and moving V_1.

3.3.5 Optimal model selection

Figure 3.4(a) shows initial closed polygon formed by using boundary points extracted based on modified convex-hull algorithm after building detection. Figure 3.4(b) is the initial simplified polygon simplified by DP and initial DL value for the null hypothesis is calculated. In the next step (c), after computing {DL} for the entire vertices, the optimal hypothesis to produce the minimum DL, which is smaller than the null hypothesis, is selected (see the dotted box in Figure 3.4(c)). In Table 3.1, the null hypothesis's DL (Figure 3.4(b)) is larger than the one in Figure 3.4(c) because the configuration eliminating one of vertices from building outlines mainly contributes to the optimal configuration. If neighboring line's directionality has the same CLF

value, a simple merging procedure is performed as shown in Figure 3.4(d). The last step (Figure 3.4(e)) presents the final optimal outlines after recursively conducting the processes illustrated in Figure 3.4(c) and (d) until the minimum DL obtained at the current iteration is larger than the one at the previous iteration.

(a)   (b)   (c)

(d)   (e)
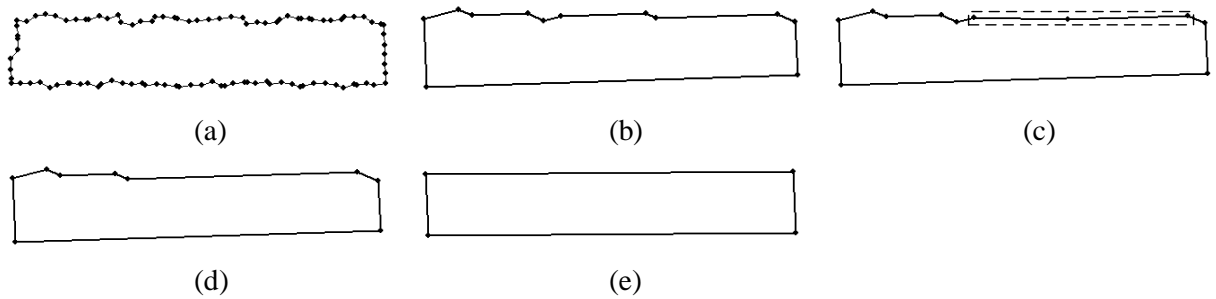
Figure 3.4: Principal steps of the regularization of irregular building boundary lines: (a) initial shape, (b) vectorization based on Douglas-Peucker approach, (c) reconstruction of lines within dotted line, (d) merge, (e) final optimal configuration.

Table 3.1. The values of DL elements in each step of Figure 3.4.

Step	N_P	N_D	$Q_{\Delta\theta}$	$L(M)$	$\Omega/2ln2$	DL
(b)	12	4	3.33	34.65	22.61	57.26
(c)	11	4	2.66	30.55	23.62	54.17
(d)	9	4	3.11	25.53	24.26	49.79
(e)	4	2	0.0	6.00	15.82	21.82

One of the key issues of the proposed method is its ability to change the regularization level of irregular building polygon as illustrated in Figure 3.5. This can be achieved by changing weight value λ in the MDL cost function (Eq. (3.4)). Each optimal model is derived from the same initial building polygon (Figure 3.5(a)).
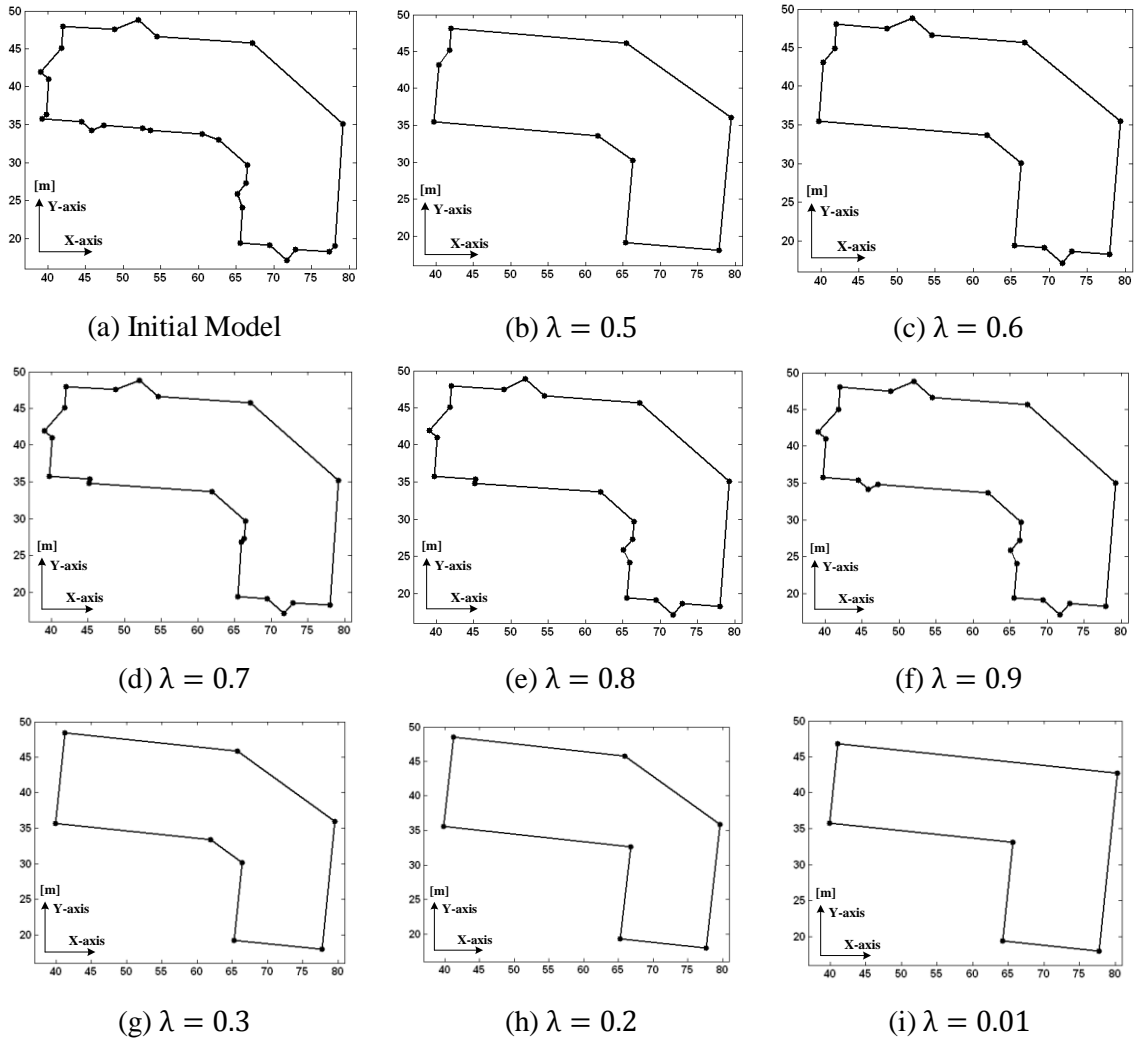
Figure 3.5: Level of detail of optimal prismatic models according to the change of weight value λ.

The initial model is extracted by DP algorithm as a common line-simplification algorithm, resulting in a sequence of connected vertices with geometric random errors. Figure 3.5(b) illustrates the regularized optimal shape at the default weight value (λ = 0.5). As the weight in the model closeness increases from 0.6 to 0.9, the level of detail in representing the building shape increases (Figure 3.5(c) to 3.5(f)). This means that the building shapes are optimized to data with

more vertices and line directions. On the other hand, the increase of weight $(1 - \lambda)$ in the model complexity from 0.7 to 0.99 allows more simple representation of the polygon (Figure 3.5(g) to 3.5(i)). In practice, according to the user preference, this modeling scheme can be useful for various applications. For example, detail modeling for decision-making on construction (Scherer and Schapke, 2011) and coarse modeling for an urban planning (Yu et al., 2010)

3.4 3D polyhedral rooftop modeling

Once building outlines are generated using the prismatic modeling discussed in the previous section, they can provide meaningful shape information for subsequent polyhedral building rooftop modeling. That is, the outlines with geometric regularities can be used as significant primitives representing main attributes of rooftop structures such as orientations of rooftop vectors. Thus, the use of primitives that are newly detected inside building is constrained to *a priori* knowledge derived from the outlines. This leads that a rooftop structure with noisy vectors is effectively converged to its optimal model with regular shape based on the proposed regularization framework. Note that this section mainly focuses on the geometric regularization of noisy building rooftop models which are generated by the previous research (Sohn et al. 2008). Figure 3.6 shows the whole workflow of 3D rooftop modeling process including the regularization step proposed.
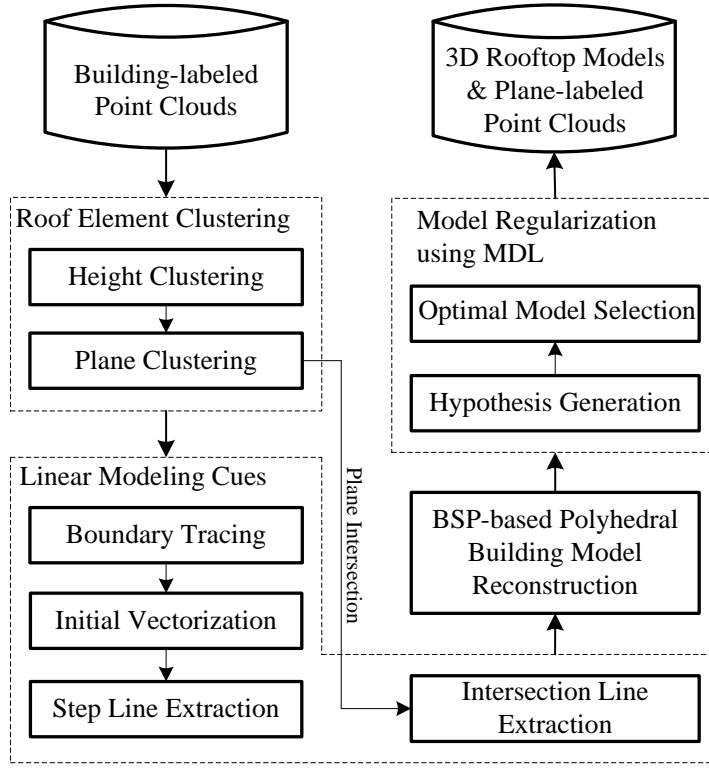
Figure 3.6: The whole workflow of polyhedral-like building rooftop modeling.

3.4.1 Roof element clustering

Buildings exhibit a range of rooftop types and a complex combination of building parts including roof superstructures. This places some limitations on extracting meaningful modelling cues directly from building-labelled point clouds. To reduce the complexity in feature extraction, the first step is to partition building points into each homogeneous rooftop region based on two similarities: height and plane similarity. In the height clustering, let $R = \{P_i \mid i=1,2,\dots n\}$ represent a rooftop region with n numbers of points and consists of m numbers of height segments $R = \{S1, S2, \dots, S_m\}$. Height difference at each point is computed from its neighbour points connected in Triangular Irregular Network (TIN). If it is less than a certain threshold, Pi belongs to the same height cluster. As a result, the segments satisfy with the property $R = \bigcup_{i=1}^{M} S_i$, $S_i \cap S_j = \{\}$,

$\forall i \neq j$. Once a set of height clusters is extracted, the plane clustering process is performed over each height cluster S_i, which is decomposed of k numbers of plane clusters $\{\pi_1, \pi_2, ..., \pi_k\}$. We adopt random sample consensus (RANSAC) algorithm to obtain the best plane segments as suggested in some previous studies (Ameri and Fritsch, 2000; Tarsha et al., 2008). First, three points are randomly selected. These points are used as seed points to generate an initial plane segment. Then, more points are captured by using a tolerance distance ζ between π_i and P_j, and plane parameters (a,b,c) are updated recursively. This process continues until each plane has the maximum probable inlier points and all points that belong to S_i are assigned into plane clusters.

3.4.2 Linear modelling cue extraction

After plane segments are detected, two different types of line primitives (intersection and step lines) are extracted. The intersection line is simply generated by intersecting between adjacent planar segments. To extract step lines, plane boundary points are traced. This process is accomplished by using a modified convex-hull method, in which the topology between member points is defined based on TIN structure. Then a local height discontinuity is investigated to detect step edge pixels among boundary points between adjacent planes. Then the process of initial vectorization is performed to generate linear modelling cues. Given a sequence D={P1, …, Pn}, $P_i \in \mathbb{R}^2$ of n boundary points in the plane, the polyline segments are formed as a successive chain $C= \{\overline{P_1 P_2}, ..., \overline{P_{n-1} P_n}\}$. The initial simplification of polylines is performed by obtaining a chain C' with m fewer segments. To achieve this goal, we adopt Douglas-Peucker (DP) algorithm which has been recognized as an effective line simplification method (Ramer, 1972). By using a line segment $\overline{P_i P_j}=\{1 \leq i, j \leq n \mid i \neq j\}$, if the norm from a vertex to $\overline{P_i P_j}$ is less than tolerance $\zeta > 0$, the vertex is removed, while a vertex shows the maximum norm is determined as an inlier point to the line segment . This procedure continues until the norms of remaining vertices are less than ζ. Note

that the degree of irregularity to be handled in DP algorithm depends on ζ. DP is effective to eliminate erroneous vertices in a simple manner. However, it does not provide a mechanism to make given polylines being regular shape patterns that is maximizing Gestatic laws (orthogonality, parallelity and symmetricity) in addition to simplication.

3.4.3 BSP-based polyhedral building model reconstruction

Once all modelling features (lines and planes) are extracted as described in the previous sections, topological relations amongst modelling features for each height segment are constructed using Sohn et al. (2008)'s algorithm. Sohn et al. (2008) concentrated on a topological construction with fragmentary modelling features. They proposed BSP-tree as its solution to globally recover modelling topology from incomplete features. A partitioning optimum is achieved by maximizing planar homogeneity produced through a recursive intersection between lines and associate planes. The process generates a hierarchical binary tree, in which each node (terminal) represents planar polygons that provides the information of topological relations among its adjacent planar segments. A final model is produced to combine similar planar segments in BSP-tree.

3.4.4 Model regularization using MDL

A most bottleneck of BSP-tree for rooftop modelling is caused by an "accidental cause" that occurs in line-line intersection for constructing planar topological relations. That is, an error in line feature inherited from line extraction process might lead to errors in geometry and under-/over-generation of vertices in rooftop models. Thus, it is required to rectify those errors. It could be done by line simplication algorithm. However, our goal is to make given rooftop vectors being a regular shape pattern in addition to eliminating erroneous vertices; combining line simplication

with regularization. A shape regularity is defined as being as shape pattern that shows orthogonal, parallel and symmetric relations between lines as similar to Gastaltic laws. This prior knowledge on shape regularity is often implemented using a set of deterministic rules such as "IF-THEN" rules. However, in our approach, the shape regularity means more than pre-specified rules, but implicitly derive rules (possible shape regularity) with given initial rooftop vectors. The proposed method does not require pre-determined threshold constraining the regular shapes, rather determining optimal shape through MDL-based model selection process.

Hypothesis generation

Figure 3.7 shows a situation where a number of model hypotheses is produced at P_2 in a polygon $\Pi_A = \{P_1,\ P_2,\ P_3,\ P_4,\ P_5,\ P_6\}$, to which another polygon Π_B ($\{P_3,\ P_4,\ P_7\} \in \Pi_B$) is connected. We label three vertices $\{P_2,\ P_3,\ P_4\}$ as Anchor Point (AP), Floating Point (FP), and Guiding Point (GP). Using these vertices, we drive two basis lines, Floating Line (FL = [AP, FP]) and Guiding Line (GL = $\{[$GP, FP$] \in (x,\ y) \in \mathbb{R}\ /\ \rho = x cos\theta + y sin\theta \}$) in two different orientations, clockwise and counter-clockwise. Where, θ indicates the angle between a line segment and x-axis, and ρ is the line distance from the origin. For each vertex, a number of model hypotheses are generated by moving FP along GL based on a set of line directions. These line directions are quantized globally from given entire rooftop vectors based on the CLF and refined by the least-square adjustment. Figure 3.7(b) and 3.7(c) illustrate how another sets of model hypotheses are produced when FP is merged with adjacent vertices (P4 or P7) belonging to Π_B. Therefore, based on the rules defined, various hypothetic models are generated and erroneous vertices produced by "accidental causes" occurred in BSP are gradually eliminated.
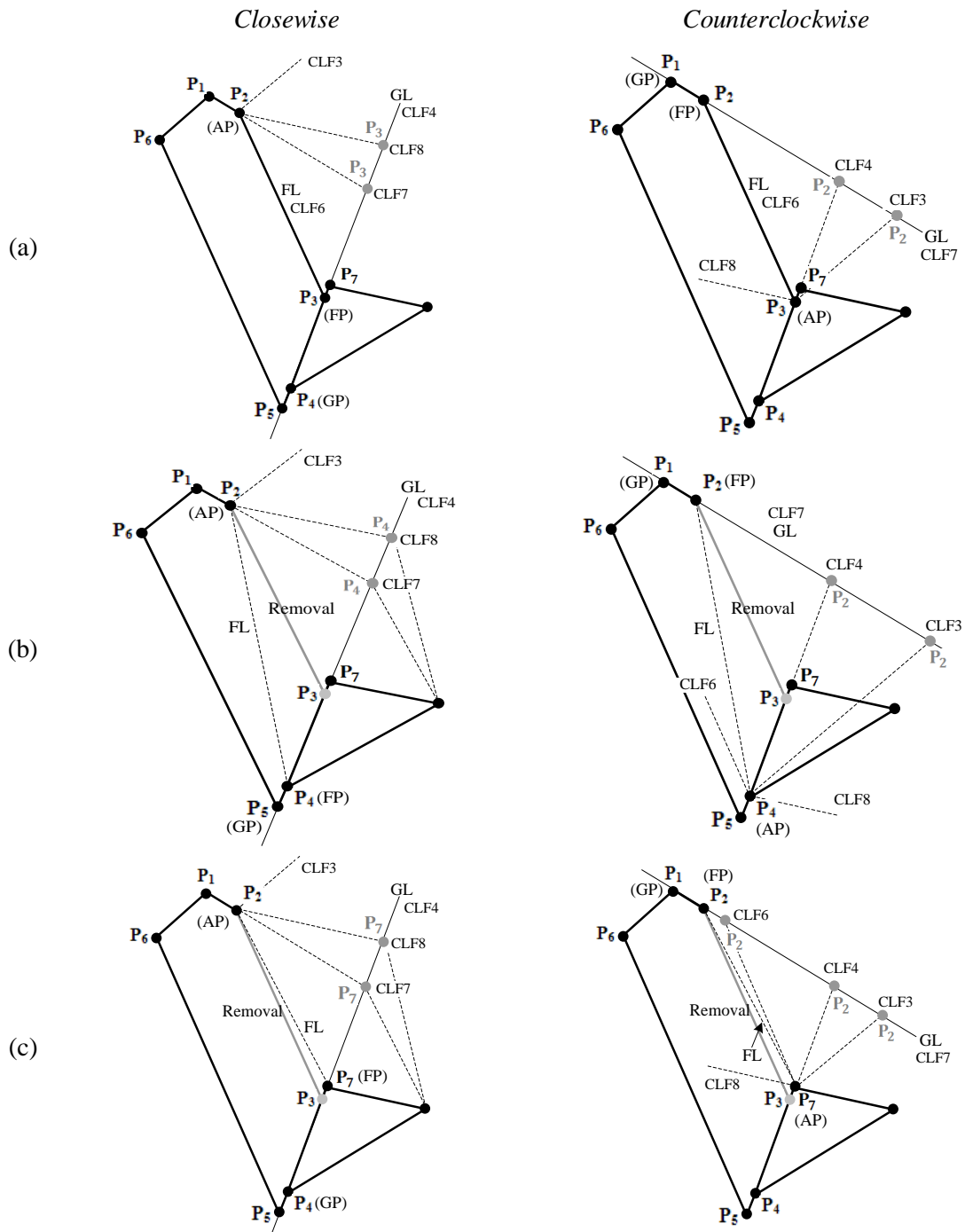
Figure 3.7: Possible alternative hypotheses by assigning three vertices as AP, FP, and GP: (a) moving FL = {P2, P3}, (b) eliminating the line {P2, P3} and moving FL = {P2, P4}, (c) eliminating the line {P2, P3} and moving FL = {P2, P7} in clockwise and counter-clockwise, respectively.

Optimal model selection

Figure 3.8 depicts an example of the whole procedure of polyhedral building rooftop modeling. The process starts with classified building map from raw LiDAR data (Figure 3.8(b)). Using this classified points, building point clouds are then segmented into height clusters (Figure 3.8(c)) based on a height discontinuity, which is subsequently segmented into planar patches using RANSAC (Figure 3.8(d)). Then, intersection (Figure 3.8(e)) and step (Figure 3.8(f)) lines are extracted. The extracted linear modelling cues are introduced to the BSP-based modelling to produce initial rooftop vectors (Figure 3.8(g)). Finally, the regularization process is performed by rectifying geometrical distortions between adjacent plane/line segments (Figure 3.8(h)) based on the MDL framework as depicted in Eq. (3.5). The fine rooftop model is produced as shown in Figure 3.8(i).
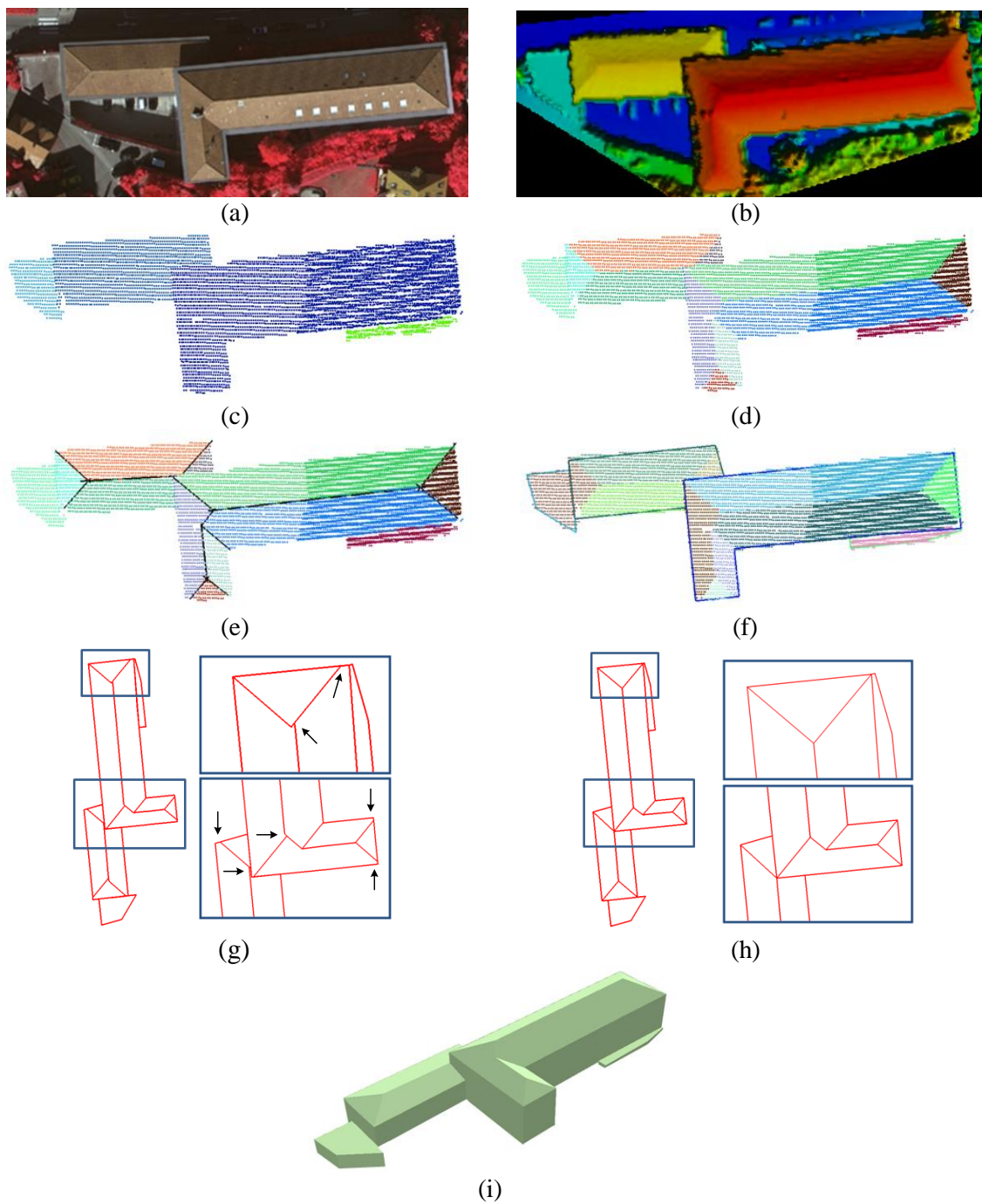
Figure 3.8: Results in reconstructing an optimal rooftop model: (a) aerial image, (b) LiDAR data, (c) height clustering, (d) plane clustering, (e) intersection line extraction, (f) step line extraction, (g) BSP-based building reconstruction with distortion errors indicated as arrows, (h) MDL-based shape regularization, and (i) 3D polyhedral building model.

3.5 Experimental results

3.5.1 Comparative study

Many geometric regularization approaches have been found in the literature. Amongst them, we selected three representative regulators from the literature for comparing their performance over noisy building outlines. These include Douglas-Peucker's algorithm (Douglas and Peucker, 1973) for conventional regularization using hard constrain such as user-driven distance tolerance, Rule-based Rectification (Sampath and Shan, 2007) using perpendicular constraints which is pre-specified, and Local Minimum Description Length (Weidner and Forstner, 1995) for verifying model hypothesis. In this section, we briefly describe the selected techniques whose performance will be later compared to a new regularization method proposed in this study.

Iterative Polyline Simplication

The classical Douglas-Peucker (DP) line-simplification algorithm has been widely recognized as the most visually effective line simplification algorithm (Ramer, 1972). This simple algorithm starts to construct a polyline with edge segments which link *a prior* initial vertex selected from edge points. The process recursively discards the subsequent vertices whose distance from the initial polyline less than $\zeta > 0$ error tolerance, which is the norm value between line and point, but accepts the vertex as part of the new simplified polyline if it is farther away from the line larger than ζ, which becomes the new initial vertex for further simplification. The starting points, which can be initial vertices, are vertices with maximum and minimum coordinate according to horizontal direction. After detecting all initial vertices, the process continues until the initial polyline from all initial vertices are less than ζ. Finally, the interesting point, corner vertex, and simplified polyline are extracted from building boundary points based on processing split and merge step, recursively. Note that the output polyline can have different shape according to user-

driven tolerance. For example, if ζ has large value, the shape of building can be over-simplification.

Rule-based Rectification

Sampath and Shan (2007) developed a rule-based regularization for refining coarse building boundaries extracted by segmentation between building and non-building, grouping, and tracing building outlines from airborne LiDAR point clouds. The method mainly consists of two-step regularization processes. The extracted building boundary points are grouped according to existing on similar line segments. Then, the second step is to further rectifying outlying points with perpendicular and parallel constraints which is pre-specified. In here, a coarse building boundary is obtained by DP, thereby eliminating noisy boundary points. After dividing slopes into two groups in horizontal and vertical direction, a simple least square adjustment is performed to regularize boundary lines with irregular shape. Since the slope direction is mainly divided into two directions, in case of the building polygon with more than two directions, the proposed regularizing process is not working well. However, this approach can rapidly provide the good solution for regularization in the building with simple shape.

Model Hypothesis-Verification

Weidner and Förstner (1995) regularized nosy building outlines extracted from high-resolution DSM using MATCH-T based on a local Minimum Description Length (LMDL). The MDL principle is a well-known optimization theory to obtain a good balance between model likelihood and model complexity based on Occam's razor. Starting from the initial building boundary obtained from the DP algorithm, the method selects four consecutive points as a local unit of the polyline regularization. With this local point set, ten different hypothetical regularization models are generated (Figure 3.1). The hypotheses are generated in order to impose the orthogonal regularity between consecutive lines, either by moving two middle points or to

enhance the simplicity by removing one of the middles points. Weidner and Förstner (1995) suggested a cost function for the hypothesis verification as

$$DL = -\frac{\Omega}{2}\ln 2 + \frac{(N_p - N_c)}{2}lbN_p \qquad (3.10)$$

In Eq. (3.10), Ω is the weighted sum of the squared residuals between D and H. H's complexity in the last term of Eq. (3.9) depends on the number of unknown parameters, N_p (i.e., the number of vertices associated to generate H), and constraints, N_c (i.e., the number of parameters to constrain the orthogonality. The optimal hypothesis, H^*, is determined by simultaneously minimizing Ω and the number of vertices used to generate H. Because of local-based approach, this method can produce different results according to starting point among building boundary points when regularization process is performed. That is, the shape of regularized polygon can be changed according to the starting point of the procedure. In order to achieve the global geometric relation of resulting polygon, another global hypothesis such as orthogonality and parallelity is needed.

An example for the performance evaluation of four regulators including three existing techniques and our proposed method shows in Figure 3.9. Based on the initial vectorization process, initial building boundary vectors (Figure 3.9 (b)) are extracted from raw LiDAR data (Figure 3.9 (a)), which shows very irregular shape. From the initial vectors, the DP method (Figure 3.9 (c)) mostly represents a detailed building shape. However, since the method only focuses on the line-simplification using pre-determined threshold, its final shape is not able to express other geometric regularities such as parallel and orthogonal properties. The Sampath-Shan approach generates a well-regularized building shape (Figure 3.9 (d)) because it is a very suitable method for regularizing a rectangular shape based on only two main directions. A small line segment is observed in the boundary vector. It can be considered as a noise. This is because its length is less than average point distance, so the detailed representation of building polygon is not

meaningful. That is, it is not a significant part of building polygon. Weidner-Forstner method produces a fully simplified building shape (Figure 3.9 (e)). However, due to the local regularization process, its final shape is not able to express a parallel property among vectors. On the other hand, the proposed method reconstructs a completely regularized building boundary shape (Figure 3.9 (f)).

(a)	(b)	(c)
(d)	(e)	(f)
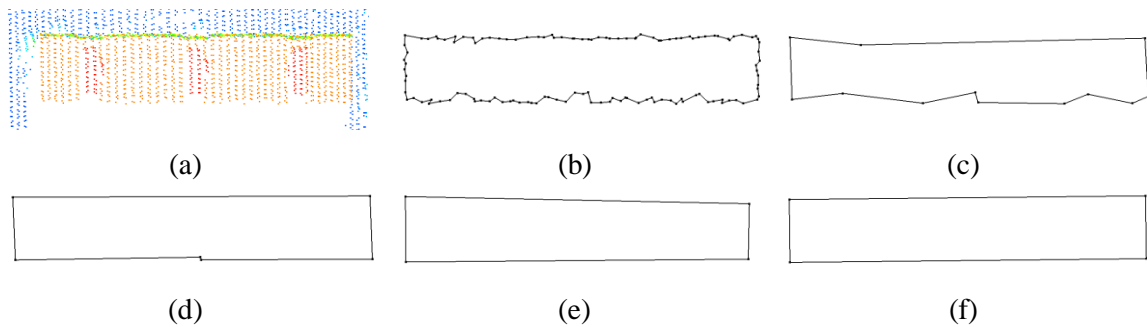
Figure 3.9: The results of regularization from building boundary vectors: (a) LiDAR data, (b) building boundary vectors, (c) Douglas-Peucker algorithm, (d) Sampath-Shan algorithm, (e) Weidner-Forstner algorithm, and (f) the proposed implicit geometric regularization.

3.5.1.1   Data set

The performance of the four regulators was evaluated using an urban area including 74 buildings, which is located in Ilsan of South Korea. As shown in Figure 3.10, the test area (450m × 550m) contains typical modern-looking buildings with various shapes such as rectangle, L, I, and T-shape. Laser point data are acquired from the Optech's ALTM-3070 system at an altitude of about 1200 m above ground level on July 28, 2005. An average point density is approximately 1.4 (points/m^2) which is equal to 0.84 m point spacing. The 3D positional accuracy of the point clouds is approximately less than 0.25 cm. Reference building vectors were manually captured from a high-resolution airborne imagery taken from the Intergraph Z/I Imaging's DMC (Digital Mapping Camera) with the ground sampling distance of 0.20m, resulting in the digital map with 1:1000 size of topological features.

(a)   (b)
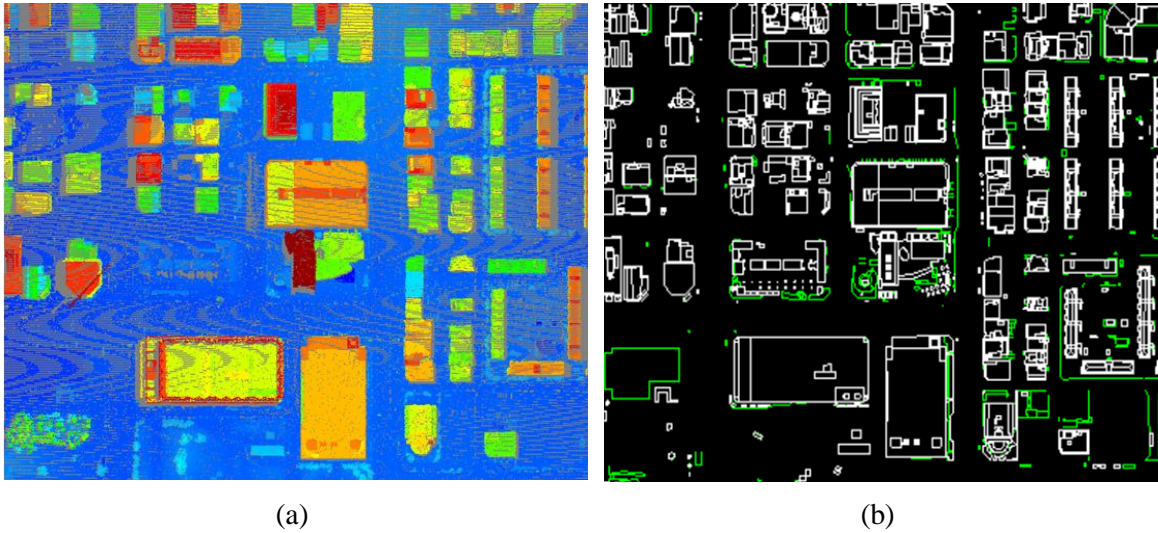
Figure 3.10: Test data set: (a) Raw LiDAR data and (b) digital map with 1:1000 size of topological features.

3.5.1.2   Quality assessment

In order to evaluate the quality of the reconstructed models produced by the four regulators, an error matrix is developed for each building polygon as depicted in Table 3.2. The matrix is composed of four factors which describe the difference between reference (R) and extracted (E) model with respect to (a) vertex (VD), (b) inner angle (IAD), (c) area (AD), and (d) centroid (CD). The VD denotes the difference in the number of vertices. In the IAD, after angles in CLF are quantized with 10 degree which results in the generation of 18 bins, inner angles at a vertex are allocated into each bin. The IAD thus expresses the difference in the number of bins allocated. The AD is the difference in the area of polygon. Lastly, the CD indicates the difference in the geometric center of polygon. For each factor of error matrix, scores which are used to judge the qualities of models regularized are calculated as the average value of entire buildings. Note that the score closer to zero indicates the regularized shapes close to the corresponding reference.

Table 3.2: Error matrix

#	Category
1	Vertex Difference **(VD)** Difference between R and E model w.r.t. the number of vertex $=\|N_{RV} - N_{EV}\| / N_{RV}$
2	Inner Angle Difference **(IAD)** Difference between R and E model w.r.t. the number of allocated bins quantized by 18 angles $=\|N_{RIAD} - N_{EIAD}\| / N_{RIAD}$
3	Area Difference **(AD)** $[m^2]$ Difference between R and E model w.r.t. area of polygon $=\|A_R - A_E\|$
4	Centroid Difference **(CD)** [m] Difference between R and E model w.r.t. geometric center of polygon $=\|C_R - C_E\|$

Figure 3.11 illustrates the results of performance evaluation for four regulators with respect to four factors of error matrix over the test data. The DP efficiently eliminated the most of noisy polygon vertices when a threshold value is properly determined (Figure 3.11(a)). Where, the threshold value was determined by the summation of average point distance (~ 0.84 m) and positional accuracy of LiDAR data (~ 0.25 m). However, the method failed to produce shapes with regular patterns that are controlled by geometric constraints such as repetition of identical line direction, angles, and lengths, orthogonality, and parallelity (Figure 3.11(b)). This is due to the fact that DP's regularity optimization is achieved only by minimizing maximal distance from hypothesized model, but there is no mechanism to augment polygonal regularity. Unlike other regulators, DP's line vectors are also directly extracted by connecting consecutive boundary points, so that final vertices are not governed by a set of adjustable parameters. This leads that the centroid of DP's pylons is close to one of reference (Figure 3.11(d)). The overall performance of Sampath-Shan's method shows better than one of DP and Weidner-Forstner algorithms. However,

due to the use of pre-fixed simple regulation rules, there are limitations to achieve more regularized shapes governed by aforementioned geometric constraints. Weidner-Forstner algorithm mostly suffers from the locality problem in applying regularization rules to polylines, so that there is no guarantee that a final form has a global regular shape. This degrades the most factors of error matrix. The performance of proposed method is outstanding compared to the other regulators, which can be clearly shown in Figure 3.11. It can be concluded that the newly driven regularization scheme efficiently contributed to remove noisy vertices and augment the orthogonal and parallel properties between polylines in the global framework. Figure 3.12 shows prismatic building models generated by the proposed method, which are overlaid on the corresponding 2D imagery.
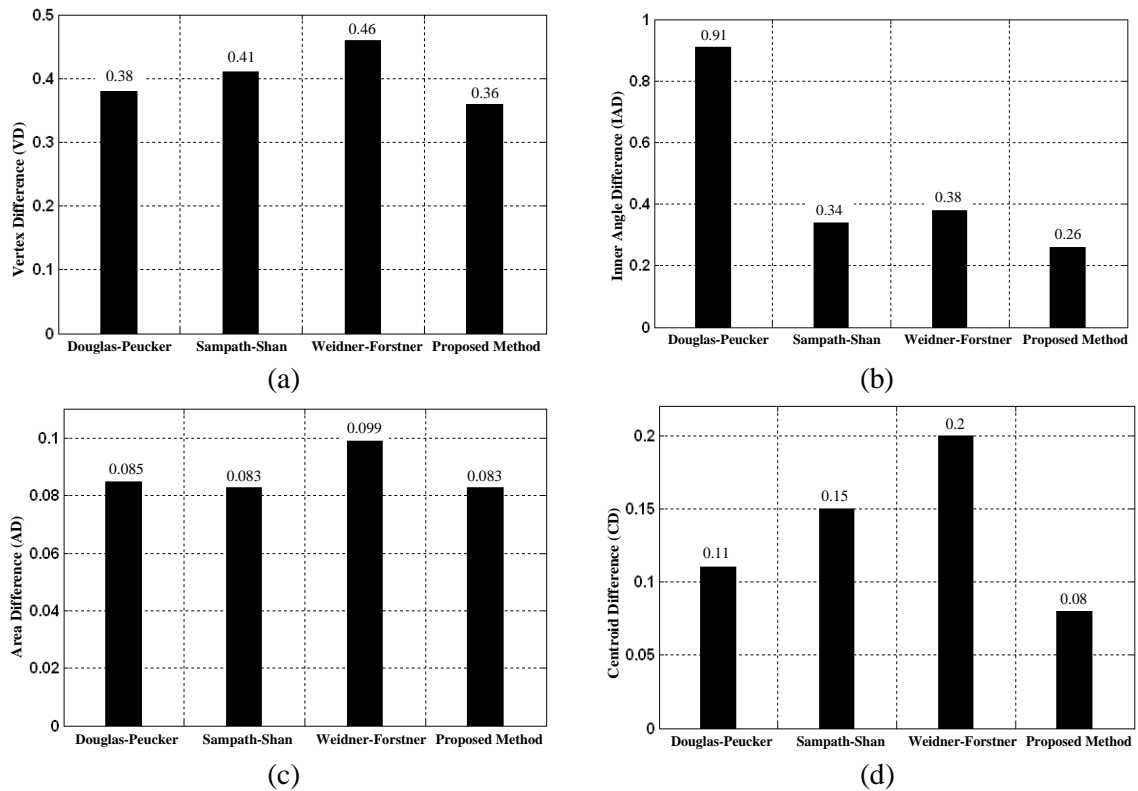
Figure 3.11: Performance evaluation of four regulators w.r.t. four categories: (a) Vertex Difference (VD), (b) Inner Angle Difference (IAD), (c) Area Difference (AD) and (d) Centroid Difference (CD).
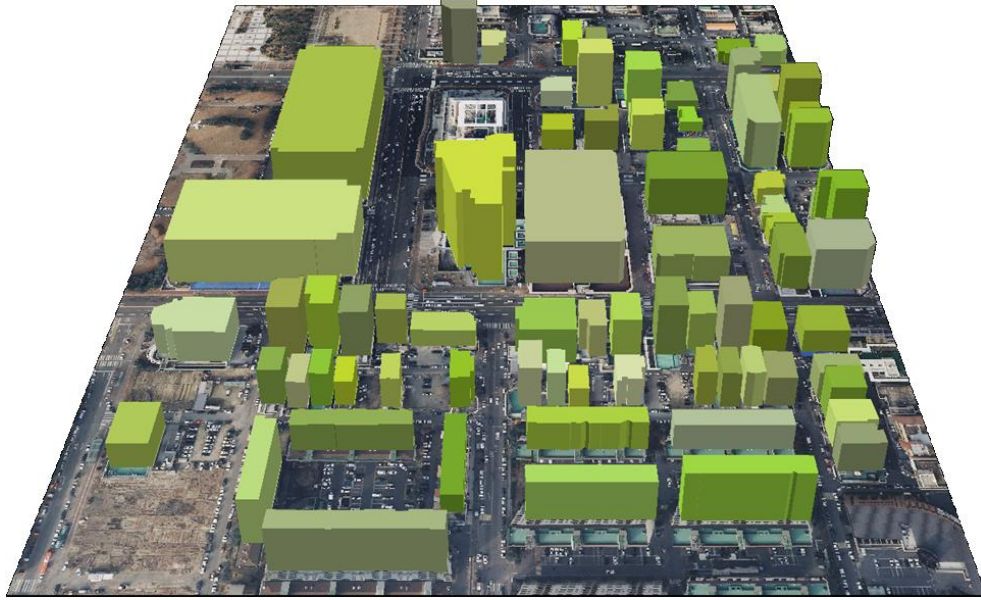
Figure 3.12: 3D prismatic building models generated by the proposed implicit geometric regularization in the MDL framework over Ilsan test area in Korea.

3.5.2 ISPRS benchmark test

3.5.2.1 ISPRS test data

The performance of the proposed method was evaluated and visualized with five real data sets (Figure 3.13) which are provided from ISPRS Commission III, WG3/4 and used for the ISPRS test project on urban classification and 3D building reconstruction. Figure 3.13(a) illustrates typical European building types showing various degrees of shapes including gable, hip roof, and their mixed structures, which is located in Vaihingen, Germany. The area is divided into three sub-data sets with respect to primary building types. Area 1 (120m × 180m) contains historic buildings with complex shapes. Area 2 (135m × 185m) is characterized by long-connected buildings (i.e., ~ 65m length). Area 3 (140m × 215m) includes a normal residential area with various sizes (i.e., from 35m^2 to 625m^2). Figure 3.13(b) shows Toronto urban area in

Canada, where typical modern buildings containing various structures from a simple shape (i.e., rectangle, L, I, T-shape) to very complex multistore buildings are positioned. The region is divided into two sub-sets: Area 4 (410m × 535m) contains a mixture of low and high buildings (i.e., from 5m to 145m above the ground level). Area 5 (410m × 550m) is distinguished by a complex cluster of high-rise buildings (i.e., ~ 21,000 m^2 of cluster area).

(a)

Area1　　　　　　　　Area2　　　　　　　　Area3

(b)

Area4　　　　　　　　　　　　Area5
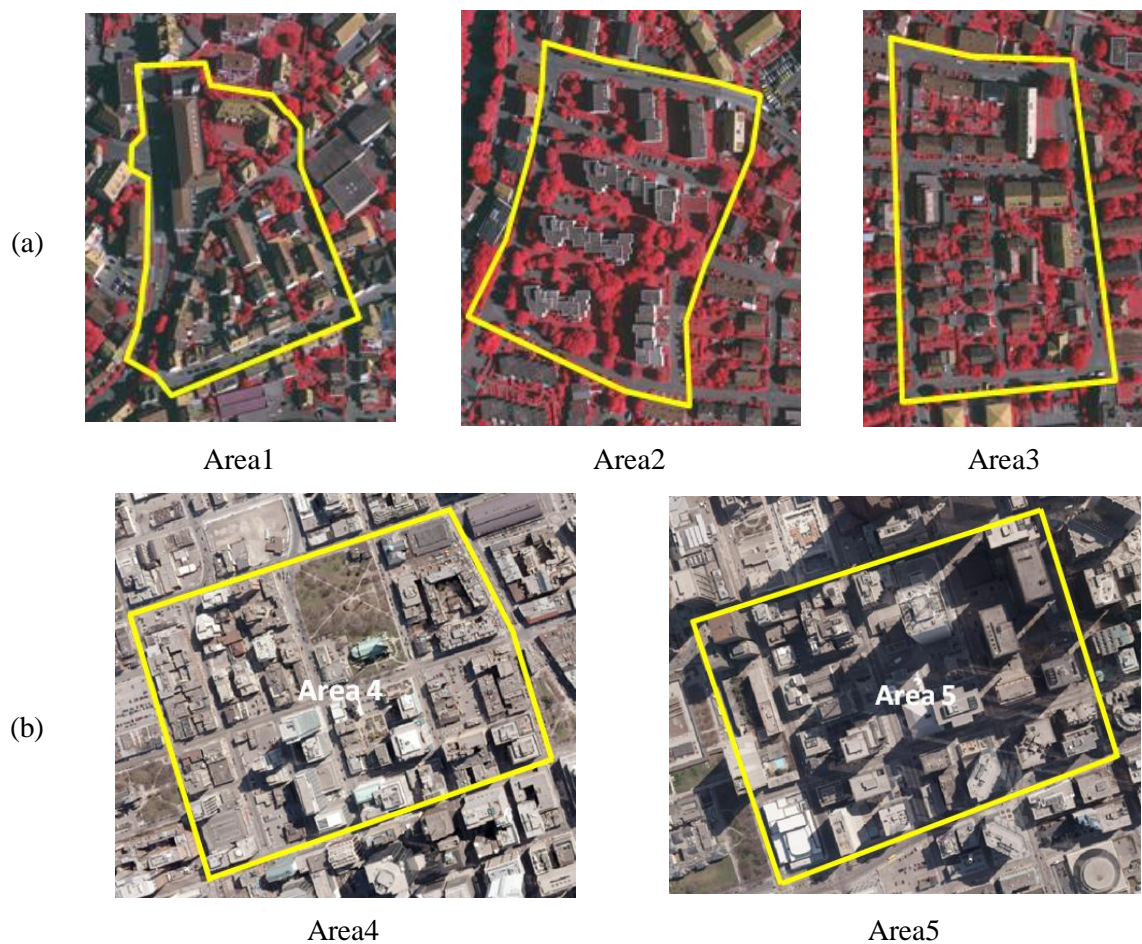
Figure 3.13: Five ISPRS test data sets (yellow colour line): (a) Vaihingen in German and (b) Toronto in Canada.

The Vaihingen LiDAR data set was acquired by Leica ALS50 system at an altitude of 500m above ground level in August 2008. 10 strips are overlapped with 30% rate and an average point density is approximately $6.7/m^2$ (~ 0.39 m point spacing). For the Toronto data set, Optech's ALTM-OPION M system was operated and the ALS data acquisition was carried out at an altitude of 650m in February 2009. The test area includes 6 strips with about $6/m^2$ average point density (~0.41 m point spacing). Total 206 building objects are located in the test areas. The 3D positional accuracy in both LiDAR data representing the buildings is approximately less than 15 cm provided from a mapping company.

3.5.2.2 Quality assessment

For the quality assessment of proposed method, the evaluation result on building rooftop modeling is reported from the ISPRS Commission III, WG3/4 by comparing extracted models with the corresponding references. A more detailed description on the evaluation can be found in Rottensteiner et al. (2012) and the website, http://www. commission3.isprs. org/wg4/. The evaluation is mainly performed by two criteria: the analysis on (a) geometric errors of models and (b) segmentation quality.

The first criterion is utilized to examine how well each extracted vertex V_e close to its reference V_r. This is simply performed by measuring Euclidean distance $d(V_e, V_r)$ between conjugate paired vertices in result and reference. Note that the pair's relations are established if *d()* is less than a tolerance distance d_t (i.e., 3 m). The Root Mean Square (RMS) error, $RMS_d = \sqrt{\frac{\sum d^2}{N}}$, of a set of *d(p,q)* is then calculated using the number N of conjugated pair. Based on the RMS value, two different evaluations are used and their results are shown in Figure 3.14: (a)

RMS from V_e to V_r, $RMS_{d(V_e \rightarrow V_r)}$, which denotes the nearest V_r at each V_e, (b) RMS from V_r to V_e, $RMS_{d(V_r \rightarrow V_e)}$, which indicates the closest V_e at each V_r.

(%) Accumulation of Conjugate Paired Vertices

Subset	Total RMS
Area 1	0.75 [m]
Area 2	0.77 [m]
Area 3	0.77 [m]
Area 4	1.00 [m]
Area 5	1.07 [m]

RMS $(V_e \rightarrow V_r)$[m]

(a)

(%) Accumulation of Conjugate Paired Vertices

Subset	Total RMS
Area 1	0.80 [m]
Area 2	0.50 [m]
Area 3	0.60 [m]
Area 4	0.85 [m]
Area 5	0.89 [m]

RMS $(V_r \rightarrow V_e)$[m]

(b)
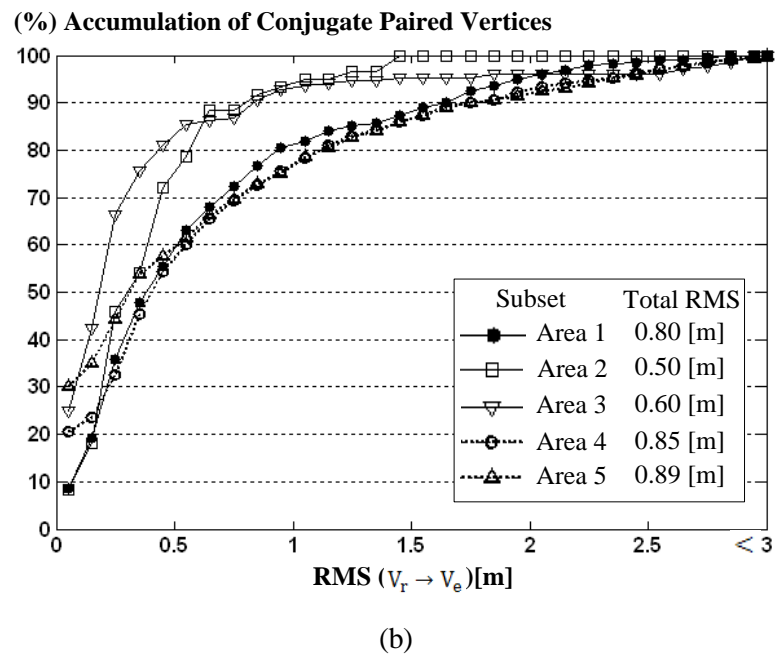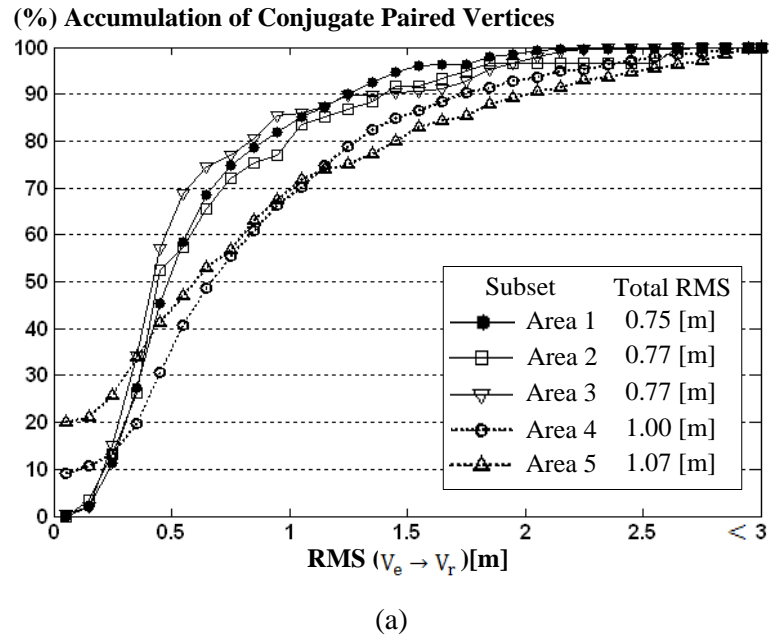
Figure 3.14: The results on positional accuracy of the boundary polygon: (a) RMS of extracted vertices w.r.t. reference and (b) RMS of reference vertices w.r.t. extracted vertices.

As a result, results derived from the two evaluations mean the positional quality of vertices in extracted polygons. If the extracted polygons fit well to the corresponding reference models, the accumulation rates in the histogram of RMS show the high values within small RMSs of distance between V_e and V_r. Overall, more than 70% of extracted vertices V_e is located with less than 1.0 m RMS. If the positional accuracy of data (i.e., ~0.15m) and average point distance (i.e., ~0.4m) as well as building scene complexity including occlusion are taken into account, the result can be considered as a reasonable solution. In most of test area, the result of $RMS_{d(V_r \rightarrow V_e)}$ is better than one of $RMS_{d(V_e \rightarrow V_r)}$. The reason is that the proposed method provides under-simplified models with redundant vertices compared to the reference. This leads that multiple V_es may correspond to a V_r, so that overall accuracy (i.e., RMS) can suffer.

Next, to evaluate overall building reconstruction performance, a confusion matrix which consists of three categories (i.e., completeness (Cm), correctness (Cr), and quality (Qa)) is introduced and each category is formulated by three factors: (a) TP (True Positive) which is the number of building objects that are found in both the reference and the result, (b) FN (False Negative) which is the number of building objects that are found only in the reference, but not in the result, (c) FP (False Positive) which is the number of building objects that are found only in the result but not in the reference. By using the ratio among the three factors, the completeness can be defined by TP and FN, which denotes the detection rate of objects. The correctness can be formulated by TP and FP, which shows how well the extracted models match to the associated reference models. The quality is derived by three factors and indicates the overall quality of results. The three categories are defined as:

$$\text{Completeness (\%)} \quad = \frac{\text{TP}}{\text{TP+FN}} \times 100$$

$$\text{Correctness (\%)} \quad = \frac{\text{TP}}{\text{TP+FP}} \times 100 \qquad\qquad (3.11)$$

$$\text{Quality (\%)} \quad = \frac{\text{TP}}{\text{TP+FP+FN}} \times 100$$

The overall performance analysis is tabulated in Table 3.3. The confusion matrix is applied to three different geometries: (a) area of buildings, (b) number of polygons with more than 50% overlap with reference, (c) number of polygons with more than 10 m^2. In the area level, the completeness and correctness of building models extracted show more than 90%. This means that the most of resulting building models are properly overlapped to the corresponding reference models with small portion of FPs (i.e., overall 1.9%). However, the results fail to describe detailed boundaries of buildings when we observe the FN with relatively high portion of 9.8%. This is mainly caused by the limitations of data in representing the structures of buildings due to for example occlusions. Since the laser last return information is usually used for the building modeling, the extracted models also tend to shrink compared to reference vectors. Additionally, the regularization process sometimes causes errors such as over-simplification of detailed boundary lines. This is because the proposed method is performed under the assumption that LiDAR data usually show irregular distribution. In the polygon level, firstly, polygons with at least 50% overlapping to their reference are considered for the evaluation, which results in 77.3% completeness and 96.4% correctness. As detail building models including superstructures in reference are provided, non-matched polygons which are found in reference but not in result are found. This leads to produce the relatively low completeness. Next, polygons covering an area of more than 10m^2 in reference compared with resulting polygons, resulting in 89.9% completeness and 98.2% correctness. This is very promising results with high success rate as LiDAR data

usually have a limitation in describing building parts including superstructures compared to high-resolution images with centimetre-level ground sampling distance.

Table 3.3: Overall quality of building rooftop modeling.

Sub-Set	# Building	# Plane	Area			Polygon(50%overlap)			Polygon(10m^{2}area)		
			Cm	Cr	Qa	Cm	Cr	Qa	Cm	Cr	Qa
Area1	38	288	88.8	99.5	88.4	88.2	98.5	87.0	89.9	98.2	88.4
Area2	15	69	90.2	99.8	90.0	73.9	100	73.9	90	100	90
Area3	57	235	88.8	99.7	88.5	84.7	100	84.7	89	100	89
Area4	58	967	89.5	98.2	88.1	75.5	97.5	74.1	83.5	97.5	81.8
Area5	38	640	93.8	93.5	88.1	64.4	85.8	58.2	86.1	85.7	75.2
Total	206	2199	90.2	98.1	88.6	77.3	96.4	75.6	89.9	98.2	88.4

Figure 3.15 visualizes a final outcome of the proposed regularization approach reconstructed from the ISPRS test data sets. The two representative buildings of each sub-data set are selected: complex roof shapes integrated with a gable structure for Area1, long-connected buildings for Area2, typical resident buildings for Area3, complex modern buildings with multistory for Area4, high layer buildings for Area5. Due to the presence of irregularity in the LiDAR data distribution, the initial boundary edges of buildings contain geometric distortions. However, the proposed method successfully corrects the most of the distortions by removing redundant edge segments and imposing geometric constraints to line vectors in the MDL framework as shown in Figure 3.15(c). Figure 3.16 shows all reconstructed building models overlaid on the corresponding aerial images.

A 4		
A 5		
	(a)	(b)	(c)
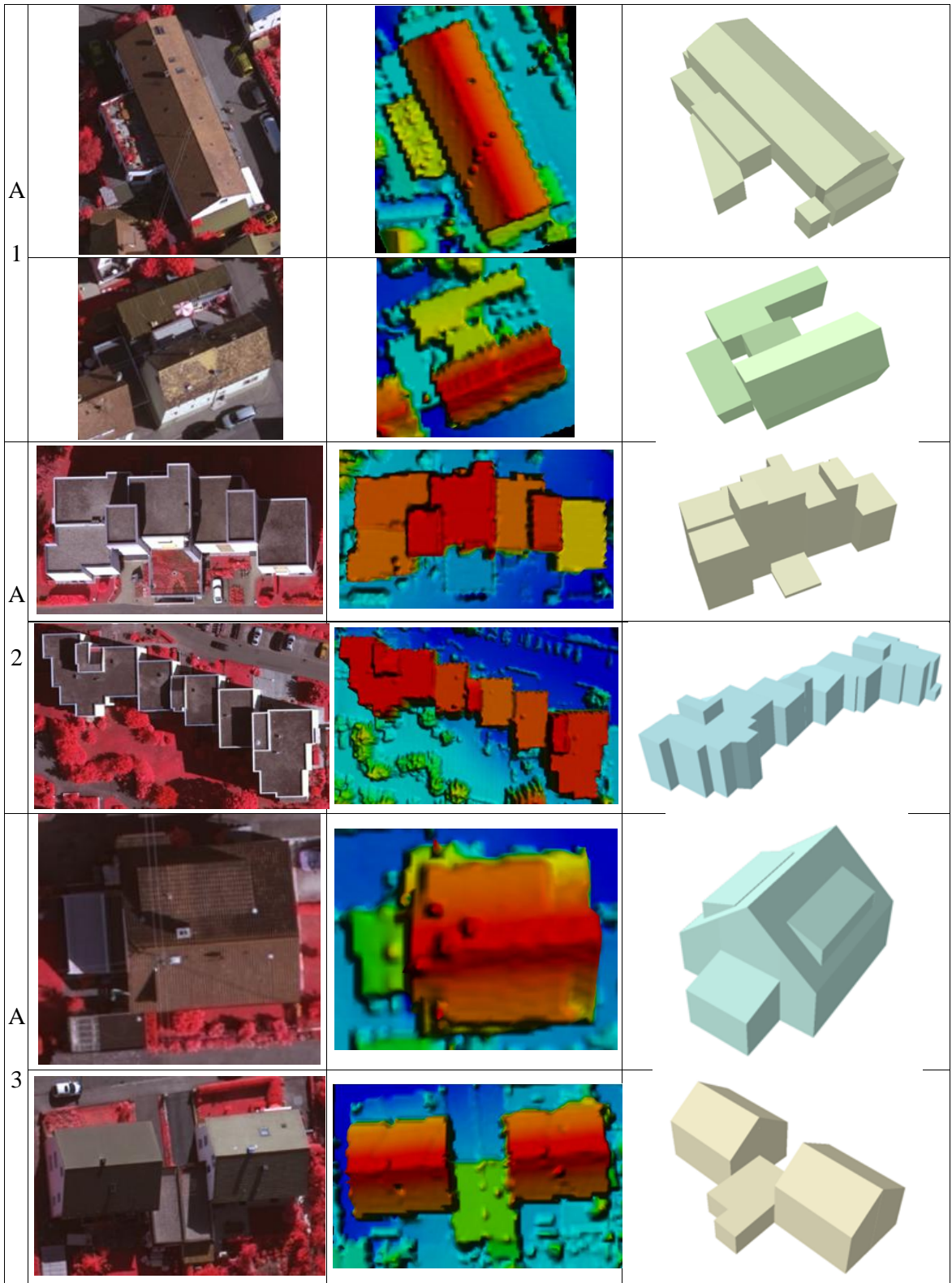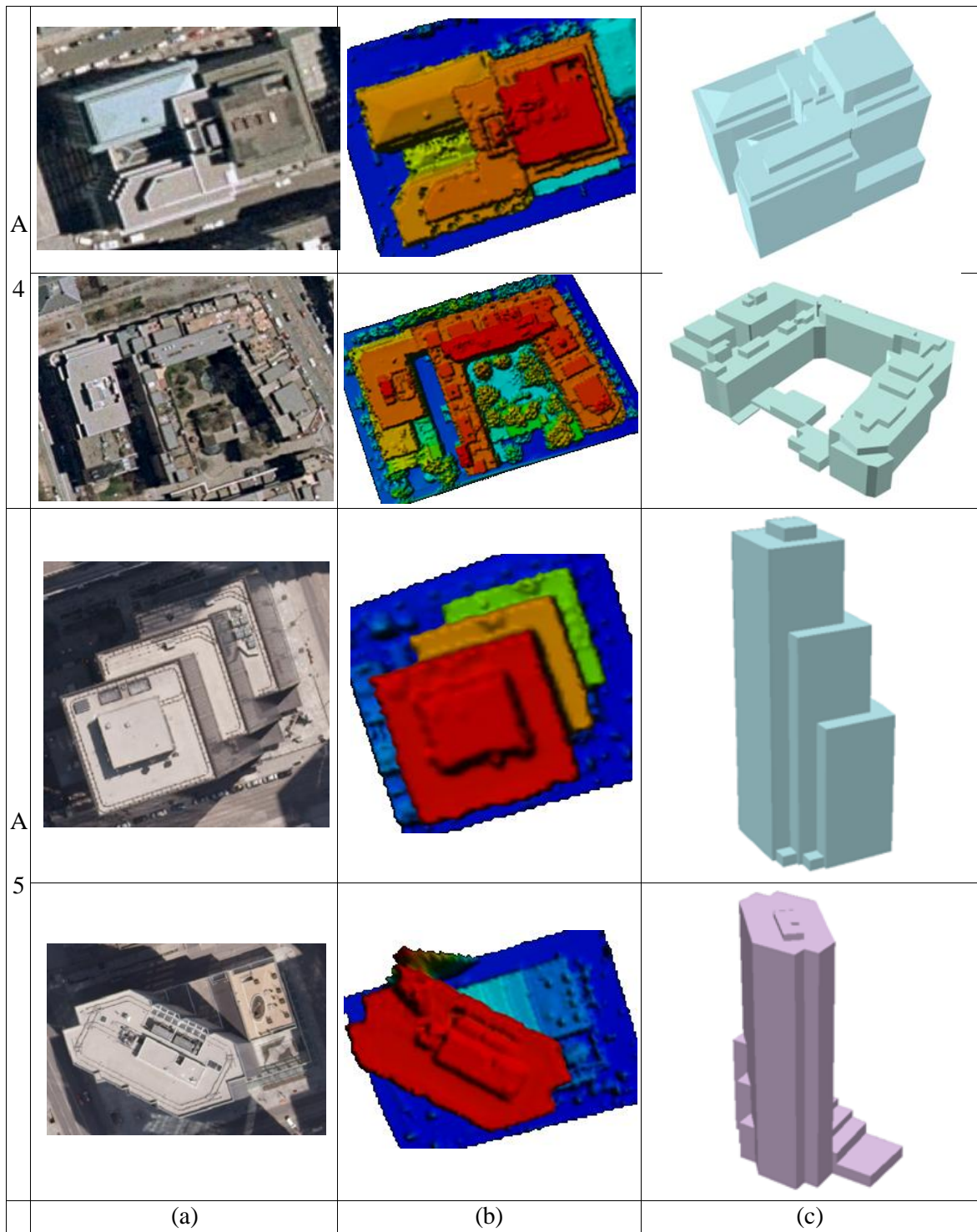
Figure 3.15: Reconstructed building models with complex roof structure: (a) airborne images, (b) LiDAR point clouds, and (c) perspective view of the reconstructed 3D building model.
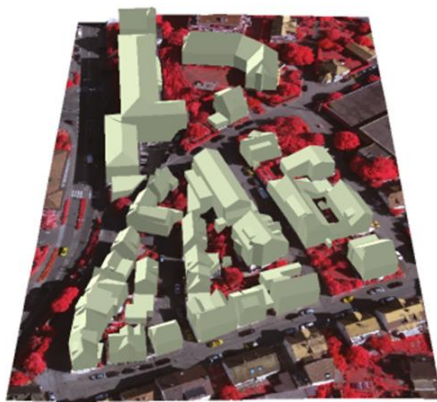
(a) Area1
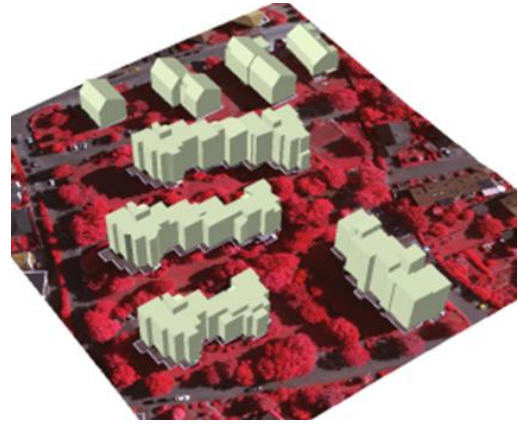
(b) Area2

(c) Area3

(d) Area5

(e) Area4

Figure 3.16: Perspective view of 3D building reconstruction results: (a), (b), and (c) Vaihingen in Germany and (d) and (e) Toronto in Canada.

Figure 3.17 illustrates limitations of the proposed method, which mainly occur from plane clustering (Figure 3.17(a) and 3.17(b)) and detailed representation of polygon (Figure 3.17(c)) including arc segments (Figure 3.17(d)) in X-Y plane.

(a)

(b)

(c)

(d)
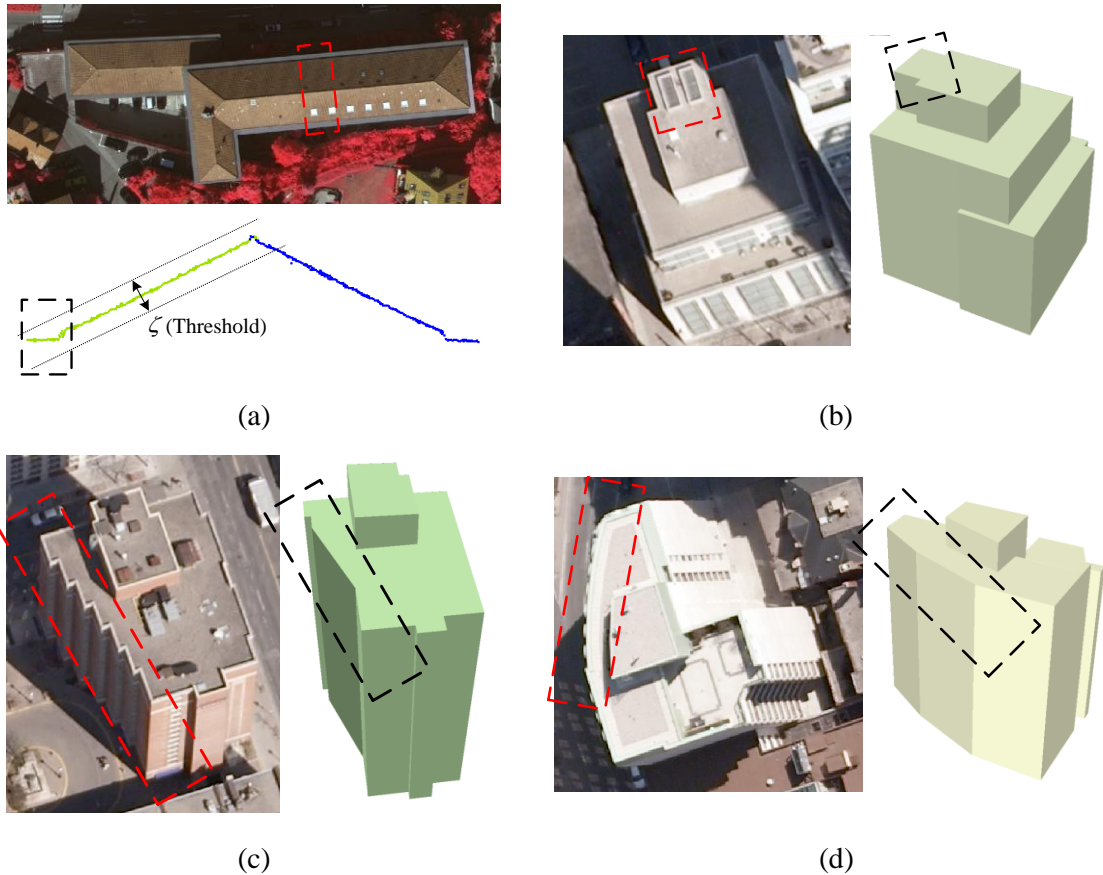
Figure 3.17: Examples of the limitations of 3D PL reconstruction due to plane clustering ((a) and (b)), over-simplification (c), arc-segment extraction (d).

In Figure 3.17(a), when the plane clustering process is performed using building points, the detected polygon is over-segmented by merging adjacent planes due to the use of fixed error tolerance. The similar situation occurs in the height clustering as shown in Figure 3.17(b). If the height discontinuity between neighboring planes is smaller than the threshold used, the

corresponding planes are merged into one plane. As depicted as Figure 3.17(c), extracting polylines with small length (For instance, about 1 m) is a big challenging task. This is because the quality of line extraction normally relies on existence of sufficient data rather than performance of algorithms in the data-driven approach. Thus, there is a limitation to accurately collect edge evidences and it is hard to recover the polylines. In Figure 3.17(d), since the proposed method is carried out under the assumption that a polygon is composed of discrete line segments, there is a limitation to extract arc segments, which are approximated by linear fragments in this study.

Chapter 4

3D power line model reconstruction: Piecewise catenary curve model growing

This chapter describes a new method for 3D power line (PL) model reconstruction, called Piecewise Model Growing (PMG), which is a hypothesis verification and its optimal model propagation process. The process starts to detect PL candidate points from raw ALS data. Then, an initial catenary model generated over the candidate points piece-wisely grows to capture all PL points of interest and thus converted into a full PL 3D model. That is, abstract information of irregularly distributed PL points is to be converted into the more geometric form using a catenary curve model. The important issue in PMG is able to reduce the complexity in processing PL modeling by using hypothetical PL models as guide lines. Furthermore, it enhances the efficiency of the PL modeling process by simultaneously capturing PL points and modeling PLs. This is in contrast to the general approach that *a priori* information such as labelled PL points in incorporated into the PL modeling process.

4.1 Introduction

Three-dimensional (3D) modelling of power lines (PLs) is one of the most critical processing steps in PL management. The main reason for this is that PL models can ensure accurate and time- and cost- effective maintenance of the safety operations of PL infrastructure. The 3D PL model-based management strategy is supported by the fact that potentially hazardous situations including vegetation encroachments, which often result in electrical shock hazards, fires and outages, should be manipulated at the appropriate time. At present, the state-of-art techniques are used to reconstruct PL models, and still require human intervention, which hinders the rapid response needed for effectively managing PL risks. Therefore, achieving the automation of PL modelling is one of main goals for the rapid PL risk monitoring. This chapter describes a new method for automatic 3D PL reconstruction, called Piecewise Model Growing (PMG), from airborne LiDAR data. The proposed method is developed based on a data driven approach, which starts by detecting PL candidate points at the point level. These points are converted into the catenary curve model, which piece-wisely grows to capture all PL points of interest and thus produces a full PL 3D model. The important aspect of the PMG method is its ability to enhance the efficiency of the PL reconstruction process by simultaneously capturing PL points from the raw data set and modelling a PL feature. In most existing studies, the step for classifying PL points is conducted prior to the PL modelling process. This results in an increase in the processing time and delays the rapid delivery of the clearance report used to detect and deal with dangerous situations in the ROW. In addition, *a priori* information such as pylon position and PL voltage type is not necessary to support the PL modelling process, thus there are no constraints at the beginning of the proposed approach when the airborne LiDAR data are obtained. Consequently, the model-based geometrical information obtained from a catenary curve model can provide various benefits to improve the robustness of the PL modelling process.

In this chapter, the definition of a PL model is given first. Then, the whole workflow of PMG method is briefly introduced and detail discussions are provided in the subsequent sections. An evaluation of the proposed approach over an urban area that contains a complex PL scene concludes this chapter.

4.2 PL models

In general, a PL is modeled as a catenary curve that is defined by a hyperbolic cosine function (McLaughlin, 2006). Figure 4.1(c) shows the geometry of the catenary curve that is formed by generating a plane intersecting with a vector normal to the tangent vector derived from positions such as P_1 and P_2. As this hyperbolic cosine function is projected in horizontal (X-Y) and vertical (X-Z or Y-Z) planes respectively, we define a PL model using two different geometric forms, line equation with implicit form, $L(\theta, \rho)$, in horizontal plane and a catenary curve equation with explicit form, $C(a, b, c)$, in vertical plane as:

$$L(\theta, \rho): \quad \rho = X\cos\theta + Y\sin\theta \tag{4.1}$$

$$C(a, b, c): \quad Z = a + c\cosh\left(\frac{X - b}{c}\right) \tag{4.2}$$

where θ and ρ are the angle of line's normal vector and X-axis and the distance between the line and the origin respectively; a and b are parameters for translation of the origin; c is a scaling factor denoted as the ratio between the tension and the weight of the hanging flexible wire per unit of length; X, Y and Z are the coordinates of the points in 3D space. Note that X-coordinate is replaced by Y-coordinate when the angle closes to 90 degree (Y-axis) in order to avoid a

singularity in estimating the model parameters. Additionally, the catenary curve is generated along the line orientation calculated in horizontal plane. Thus, a PL model can properly generated without its shape deformation which may occur by the use of data projected into a certain plane (X or Y plane) in estimating parameters of catenary curve.
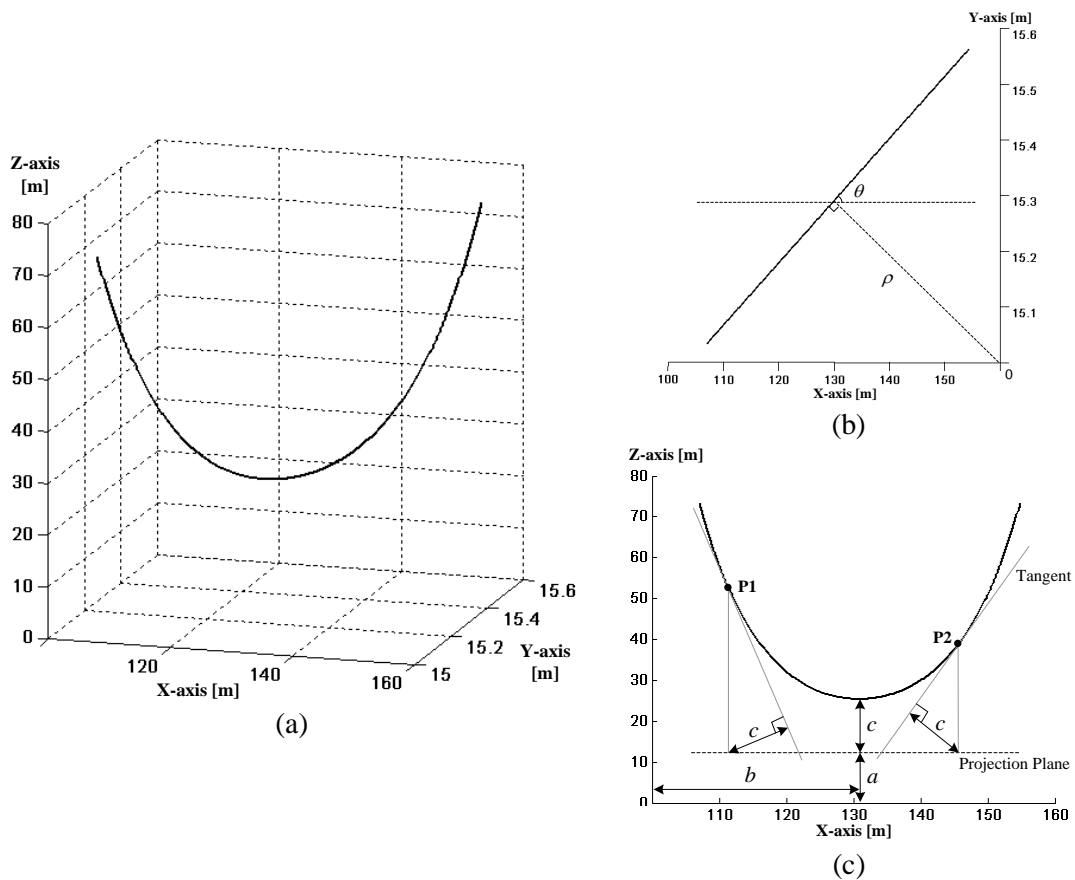
Figure 4.1: 3D PL model geometry: (a) 3D perspective view of the PL model, (b) line form in the horizontal projection, and (c) catenary curve form in the vertical projection (McLaughlin, 2006).

Compared to the use of two catenary curves $(a_1, b_1, c_1, a_2, b_2, c_2)$ in the previous research, the use of line and catenary curve (θ, ρ, a, b, c) has been found to be an effective way for 3D PL modeling as follows: (a) It is able to reduce correlations among parameters, so that the reasonable positional

accuracy of PL models on the order of 10 cm is obtained (Chan and Lichti, 2011). (b) As the angle parameter is explicitly estimated, information on the orientations of PLs is easy to be obtained. It helps us to readily identify the existence of any external forces such as wind blowing to PLs using the variation of the orientations. (c) Due to the reduction of number of model parameters, it allows us to use smaller number of PL points in generating PL models.

To estimate the parameters of the PL model, the line and catenary curve equations can be written as statistical linear models based on the Gauss-Markov theorem. In this regard, the two residual vectors of y_L and y_C between airborne LiDAR points and $M(L, C)$ are described in matrix form as:

$$y_L = A_L \xi_L + e_L; \quad e_L \sim N\left(0, \sigma_0^2 P_L^{-1}\right) \tag{4.3}$$

$$y_C = A_C \xi_C + e_C; \quad e_C \sim N\left(0, \sigma_0^2 P_C^{-1}\right) \tag{4.4}$$

Where if m and n denote the number of parameters and observations respectively, y_L and y_C are $n \times 1$ observation vectors; A_L and A_C are $n \times m$ Jacobian matrix of L and C respectively; ξ_L and ξ_C are the unknown $m \times 1$ parameter vectors of L and C respectively; e_L and e_C are $n \times 1$ observation error vectors of L and C respectively, which follows a probability density function with expectation, 0, and weight matrix, P_L and P_C; σ_0^2 is a variance of unit weight.

If we linearize Equation 4.1 and 4.2 with respect to the parameters, Ξ (θ, ρ, a, b, c), and arrange them as the form of the Gauss-Markov observation model (Equation 4.3 and 4.4), the linearization form is expressed as follows:

$$\rho^0 - X\cos\theta^0 - Y\sin\theta^0 = \left.\frac{\partial L}{\partial \theta}\right|_0 \Delta\theta + \left.\frac{\partial L}{\partial \rho}\right|_0 \Delta\rho \tag{4.5}$$

$$Z - a^0 - c^0 \cosh\left(\frac{X-b^0}{c^0}\right) = \left.\frac{\partial C}{\partial a}\right|_0 \Delta a + \left.\frac{\partial C}{\partial b}\right|_0 \Delta b + \left.\frac{\partial C}{\partial c}\right|_0 \Delta c \tag{4.6}$$

The least squares method estimates unknowns, ξ_L and ξ_C, which consist of the correction of the model parameters in the line ($\Delta\theta$, $\Delta\rho$) and the catenary curve (Δa, Δb, Δc). The solutions are obtained by minimizing the sum of the squares of the residuals derived from difference between the model and its associated observations (Wolf and Ghilani, 1997). As a result, the optimal model parameters, $\widehat{\Xi}$, for L and C can be obtained by applying the estimated corrections to initial approximations, $\Xi_0(\theta^0, \rho^0, a^0, b^0, c^0)$. The best estimates are the following formulations:

$$\hat{\xi} = \left(A^T P A\right)^{-1} A^T P y, \qquad \widehat{\Xi} = \Xi_0 + \hat{\xi} \tag{4.7}$$

4.3 Piecewise catenary curve model growing

The PMG can be described as a model-based hypothesis verification and propagation function that can be used to transfer discrete and abstract information of irregularly distributed PL points into the a more geometric form. The important issues in PMG is the early detection of PL seed elements, and piece-wisely gathering unlabelled points from the elements by using hypothetical PL models as guide lines, which reduces the complexity of the search and processing steps for the PL reconstruction. As shown in Figure 4.2, the method starts to detect PL candidate points (CPs) from raw ALS data which are potentially located on wires. The detected CPs are converted into line segments and used as seed elements in order to estimate the catenary curve parameters of the initial power line model. Producing new hypothetical models successively propagates the initial model, which is done by changing the catenary's sag points from the initial parameter to a different location. A stochastic constrained non-linear adjustment method with added parameters is developed to estimate the optimal parameters of the PL model which piece-

wisely grows by gathering all the PL points of interest and thus produce a 3D model of the full PL. Finally, we also introduce a statistical test to differentiate actual power lines from linear features extracted from non-power line objects.
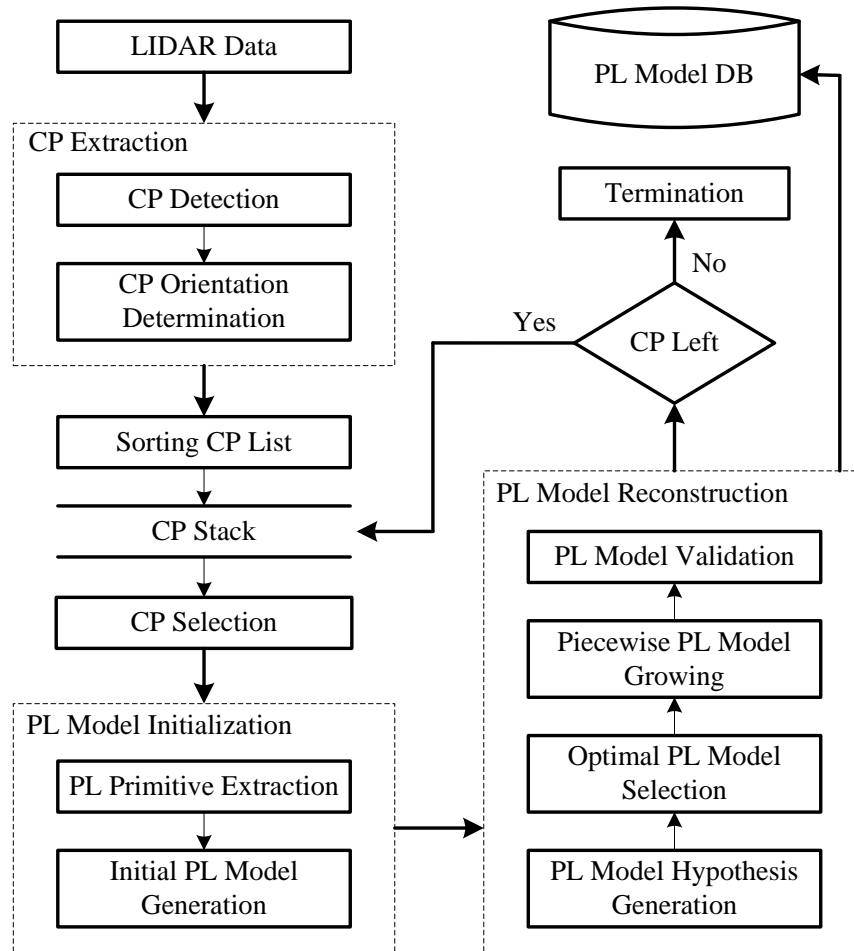
Figure 4.2: Proposed approach for automatic 3D reconstruction of PL models.

4.3.1 Extracting PL candidate points

The first step of PMG is to detect CPs that potentially represent PLs from the given ALS data. The CPs are used as seed points to form PL primitive models, which are allowed to piece-wisely grow to reconstruct the final PL models. We assume that PLs are comprised of a set of

small straight-line segments. Thus, a CP detected with high confidence possesses a strong geometric property as straight line. For extracting CPs, three different operators are used to extract linear feature from the ALS points (i.e., Hough-Transform, eigenvalue analysis, and point density analysis) are combined to compensate for the limitations imposed by each algorithm. A 3D voxel space covering the given ALS point clouds is created. Each operator is applied to an individual voxel. The voxel size is pre-specified by taking into account the average point density of ALS point clouds.

4.3.1.1 CP detection

The first operator is the well-known Hough-Transformation (HT). The HT is the one of the most popular algorithms used to extract linear features due to its simplicity and global optimization properties (Duda and Hart, 1971). In order to speed up the operation, we project ALS points onto an X-Y plane and apply the HT to each voxel to convert the projected points into the line parameter domain (i.e., slope and y-intercept). We take the maximum voting score accumulated in the HT space as indicating a degree of the presence of linear features in the voxel. As the second operator for CP detection, the eigenvalues are calculated from the covariance matrix between x, y, and z of the ALS points. Supposing that the computed eigenvalues are $\lambda 1$, $\lambda 2$, and $\lambda 3$, a combinatorial measurement of the eigenvalues suggests the type of features that a point of interest belongs to such as: $\lambda 1 \approx \lambda 2 \approx \lambda 3$ for scattering points, $\lambda 1, \lambda 2 \gg \lambda 3$ for points on surfaces, and $\lambda 1 \gg \lambda 2, \lambda 3$ for linear structures. We compute $(\lambda 1 - \lambda 2)/(\lambda 1 - \lambda 3)$ to measure the degree of the presence of linear property in the voxel. Linear features might be found in non-PL objects including building roof edges, fences and tree stems. To reduce the commission errors caused by non-PL objects, we introduce a point density analysis as third additional criterion to determine CPs. It is assumed that the point density of each voxel containing PL features shows a

lower value, while higher values emerge for non-PL features. Once the linear properties are calculated by using the three operators, we detect CPs by thresholding the three operator measurements. The optimal threshold values used in three operators are determined by training sample data.

4.3.1.2   CP orientation determination

After CPs are detected, the Compass Line Filter (CLF) suggested by Sohn et al. (2008) calculates two attributes (i.e., line orientation angle and straightness) for each CP. As shown in Figure 4.3, the CLF was designed to assign each line segment to one of eight discrete orientation angles, $\{\theta_i : i = 1, ... ,8\}$, where the orientation of the first compass line is horizontal, and from which the others are displaced at an angle equal to $22.5°$. For the determination of the initial PL direction, a voxel is created from each CP, within which a set of CP member points, D, are collected and D's variance-covariance matrix, Σ_{DD}, is calculated. The member points are horizontally projected. A hypothetical line (i.e., $\{H_i : i = 1, ... ,8\}$), where slope is given by CLF, is fitted to the horizontally projected member points. Ω_i can be defined as the sum of the squared residuals between the hypothesis and observations. H_i is modeled as linear by using line equation, $\rho_i = x\cos\theta_i + y\sin\theta_i$, where θ indicates the angle between the hypothesis and x-axis and ρ is the orthogonal distance from the origin. Then, Ωs are calculated for the whole hypotheses and the hypothesis with the lowest Ω value is finally selected as the best hypothesis, H*, which is defined as

$$H^*(\theta; \Omega) = \underset{\forall\{H_i\}_{i=1,...,8}}{\arg\min(\Omega(H_i))} \tag{4.8}$$

$$\Omega(H_i) = [D\text{-}H_i]^T \Sigma_{DD}^{-1} [D\text{-}H_i] \tag{4.9}$$

The line orientation information detected by fitting hypothetical quantized lines to local voxel space plays an important role in clustering similar CPs with the same line orientation and converting them into a PL line primitive which will be used as a seeded line for a complete PL reconstruction.
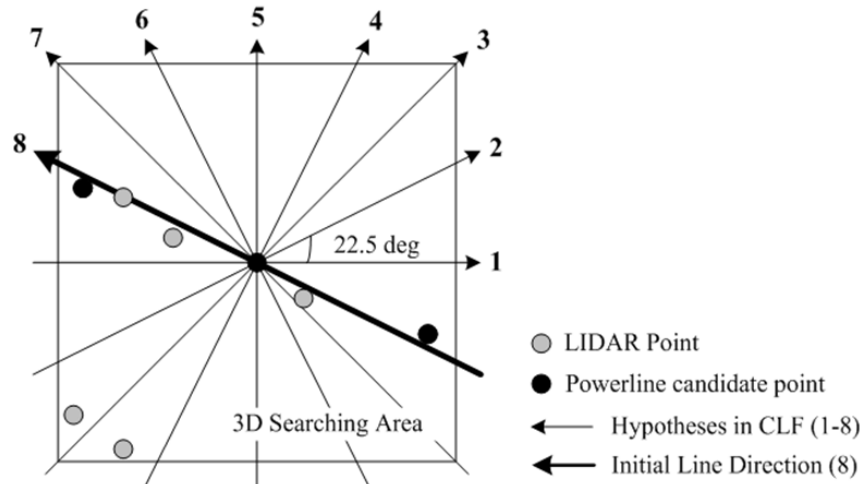
Figure 4.3: Allocating an initial PL orientation into each CP based on the Compass Line Filter (CLF).

4.3.2 PL model initialization

Extracting a CP enables the identification of potential PL points. However, the CP does not provide group information, which means it does not indicate which CPs belong to the same PL. Moreover, a CP might be coarsely detected by the rather simply designed thresholding method described in the previous section. Thus, only relying on CPs for extracting PL primitives (i.e., segment of catenary curve) would be problematic. To address this problem, we describe the segmentation method used to augment the CP detection results by grouping neighbouring points from selected CPs which form a segment of the PL's catenary curve and thus provides an initial PL model. We refer these newly detected points as PL Primitive Points, abbreviated to PP.

4.3.2.1 PL primitive points extraction

To detect PP, we adopt the one-outlier testing technique (Snow and Schaffrin, 2003), which is one of the most commonly used outlier detection techniques for many applications in photogrammetry and image processing (Abedini et al., 2008; Kersten and Baltsavias, 1994; Lu et al., 2003). The one-outlier testing assumes that only one outlier at a time is present in the data set, and thus requires successive evaluations of the reduced dataset if an outlier is detected and removed. The formula is based on the linear model in Equation 4.1 and is extended by adding an outlier vector, δ, to the parameter list. If the j-th observation in k numbers of the observations is evaluated by means of hypothesis testing, the model for the one-outlier testing is as follows

$$y = A\xi + \eta_j \delta^{(j)} + e, \quad e \sim N(0, \sigma_0^2 \Sigma) \tag{4.10}$$

where $\delta^{(j)}$ represents the hypothesized outlier quantity associated with the j-th observation and η_j is an n×1 unit vector which has only the non-zero element, 1, at j-th position, that is $[0,\ldots 0, 1, 0,\ldots,0]^T$. The corresponding quantity for the outlier vector of the j-th point is computed by

$$\tilde{e} = y - A\hat{\xi} \tag{4.11}$$

$$Q_{\tilde{e}} = I - A[A^T A]^{-1} A^T \tag{4.12}$$

$$\hat{\delta}^{(j)} = \left[Q_{\tilde{e}_{jj}} \right]^{-1} \tilde{e}_j \tag{4.13}$$

where $\tilde{e}$ and $Q_{\tilde{e}}$ are the predicted residual vector and its corresponding cofactor matrix, respectively. For the outlier test of the j-th point, the associated test statistic, T_j, can be derived

from the F distribution in which it is determined if the two data sets come from the same data set by comparing the corresponding variances. Thus, T_j is leading to the following equation

$$T_j = \frac{R_j}{(\Omega - R_j)/(n-m-1)} \quad \sim T_{F(\alpha;1,n-m-1)} \tag{4.14}$$

where $R_j = (\hat{\delta}^{(j)})^2 (Q_{\tilde{e}})_{jj}$ is a variance related to outlier quantity; $\Omega = \tilde{e}^T \tilde{e}$ is the sum of the squared residuals derived from Equation 4.11. Therefore, the null hypothesis is accepted if the test statistic is less than its associated critical value, that is, $T_j \leq T_F$.

This approach is mainly composed of three steps: (a) ordering process, (b) outlier testing in the horizontal domain, and (c) outlier testing in the vertical domain. At the first step, the CPs are sorted according to their Ω (goodness-of-fit) computed by using Equation 4.9. Then, the CP with the minimum Ω is selected for PP detection. As can be seen in Figure 4.4, starting from the selected CP_i (i.e., a green coloured dot), a 3D search window W_{out} is generated with an user-driven size; for example, a window that is 10m (length)×2m (width)×8m (height), where length and width are the values for line direction and its orthogonal direction, respectively. In the search window W_{out}, there might be many PLs, not all of which are related to a PL of interest. In Figure 4.4, there are four PLs captured in W_{out}. We are interested in PL #1, including the selected CP_i, which has to be separately segmented from the other PLs in the next two steps. For the outlier testing in the horizontal domain, as shown in Fig. 4.4(a) and 4.4(b), the data domain in W_{out} is projected onto an X-Y plane and the points, which have similar geometrical properties as the PL #1 in the X-Y domain, are clustered as the same group based on the one-outlier testing method. As depicted in Figure 4.4(a), a small search space, W_{in}^H, is created with dimensions 1m (length)×0.3m (width)×8m (height), for example. In here, the width size is normally decided by

taking into account the position accuracy of the ALS data because the performance of the horizontal-wise separation can be affected by the width value. Then, points belonging to W_{in}^H are assigned as CP member points, P_{in}, (i.e., inliers) in order to compute the critical value of T_F^H using Equation 4.14 for the acceptance of T_j. The one-outlier test is performed using the iterative method by adding one point from W_{out} to the inliers and computing its T_j. Thus, each point satisfying $T_j \leq T_F^H$ is accepted as P_{in}. As illustrated in Figure 4.4(b), the proposed method enables the separation of the member points from PL #1 and PL #3 (solid dots) from the ones belonging to PL #2 and PL #4 (empty triangles).

A similar process for the aforementioned horizontal outlier test is applied for the outlier testing in the vertical domain. Once the horizontal outlier test is finished, a search window for vertical-wise separation, W_{in}^V, is created having dimensions of, for example, 10m (length)×1m (width)×0.3m (height) (see Figure 4.4(c)). The height value of W_{in}^V can also be determined by considering the position accuracy of the ALS data for vertical-wise separation with which the critical value of T_F^V for the outlier testing is determined. Points accepted during the previous process are now tested as the final P_{in} by comparing T_j to T_F^V. In Figure 4.4(c) and 4.4(d), the outlier testing method in the vertical domain can separate line #1 (solid dots) from line #3 (empty rectangles). Finally, the P_{in} of the PL of interest (i.e., PL #1) can be found, and then used as a primitive for reconstructing the associated PL model. As it has been discussed so far, the outlier testing is essential for extracting a reliable PP, in particular to deal with a difficult situation where multiple lines are present in given a search space.
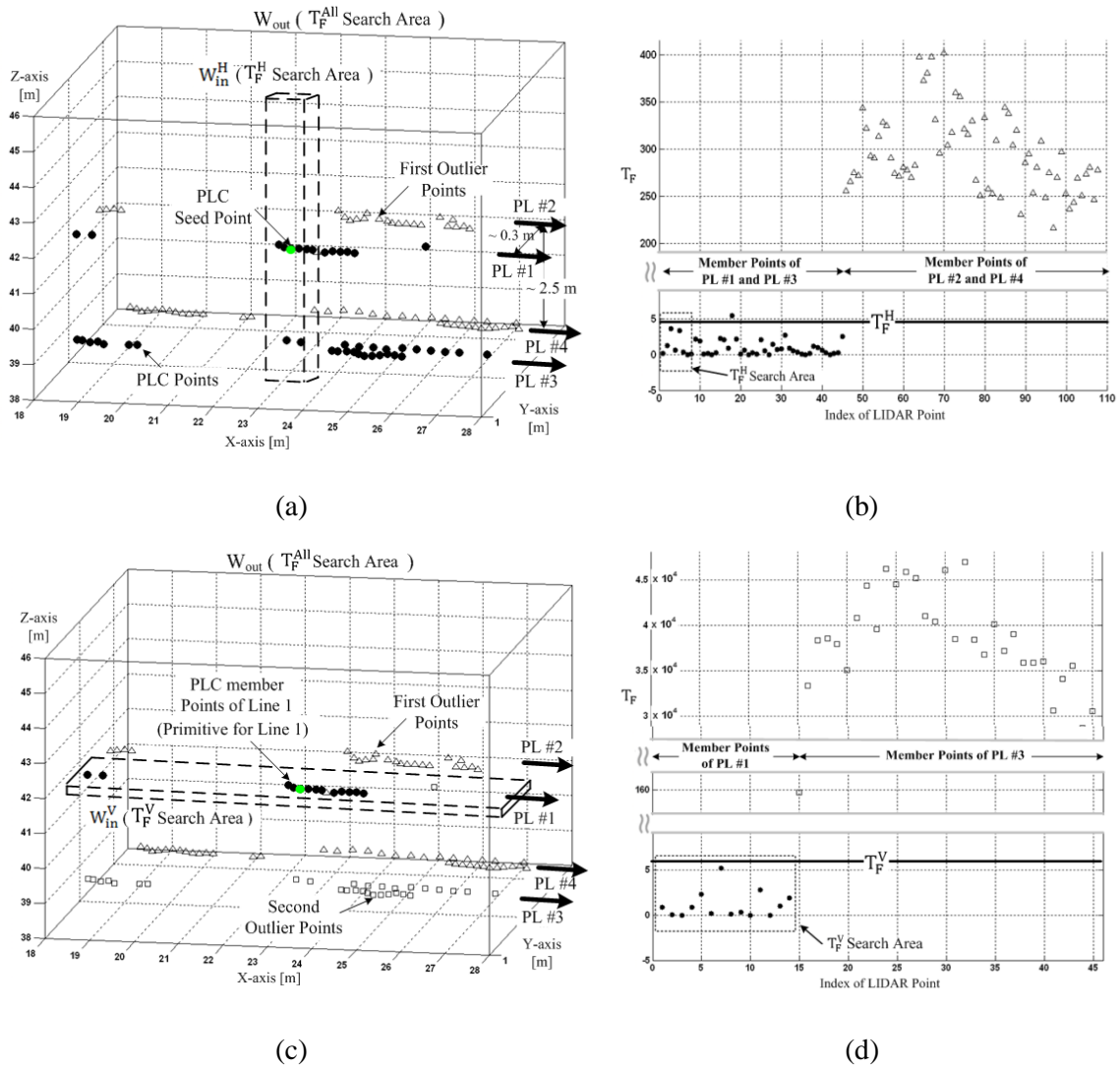
Figure 4.4: PL primitive points are extracted based on one-outlier testing in the horizontal domain (a) and (b); in vertical domain (c) and (d).

4.3.2.2 Initial PL model generation

Once a PP is obtained by the one-outlier testing process, the PP is converted into an initial PL model, $M(L, C) = M(\theta, \rho, a, b, c)$ introduced in Equation 4.1 and 4.2. However, if the PP includes an insufficient number of observations for estimating the parameter of M, a poor estimation might occur due to the irregularity of point distribution with random noise, which

causes the PL to grow in the wrong direction in the successive collection of CPs surrounding the PP. To avoid this problem, sufficient redundant observations are needed to derive a more accurate estimation of the initial PL model. Figure 4.5 schematically illustrates an example of the linear model extension to capture more CPs. Let θ_1, N_1, and V_1 indicate line direction, PL points, and the voxel-like search space covering an initial PP, respectively. Based on θ_1, V_1 is predicted for the forward and backward direction of θ_1, and for generating a new searching space, V_2', with a user specified length and data-driven width. Then, the new CP N_2, which is located within V_2' is captured, and is used to estimate and rectify the new model parameters θ_2 and V_2. Consequently, a new initial PL model M_{ext} is generated from a new set of primitive points PP_{ext}, including the new CP set, $\{N_1, N_2\}$ if the number of PP_{ext} is more than the pre-specified threshold.
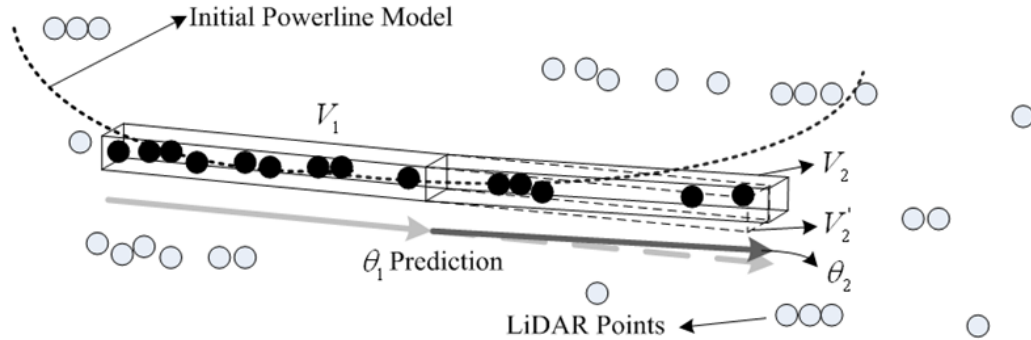
Figure 4.5: Linear propagation of voxel search space to increase redundancy of observation and initial PL model extracted.

4.3.3 PL model reconstruction

The proposed piecewise modelling approach estimates the model parameters, starting with the smallest measurements available, which are progressively refined as the measurements used for parameter adjustments increase. An implicit assumption made in this piecewise modelling is

that "smooth model transition" occurs, which assumes that there is no large deviation between the estimated model (i.e., current local model) and the targeted global model (i.e., true model). With this assumption, we can obtain the correct PP_{ext} by simply extending the physical dimensions of M and thus producing the corresponding M_{ext}. Unfortunately, the assumption of "smooth model transition" is not applicable to our case. As can be seen in Figure 4.6, a very small number of ALS measurements might be available for generating initial models at early growing iteration steps due to the effects of occlusions, shadows, and system errors. In this case, the estimated model has deviated from the targeted global model as shown in Figure 4.7(a) and failed to capture the correct PP_{ext} by simply extending physical dimensions of M. In the next section, we consider a PL model verification and its optimal selection to mitigate limitations derived from the irregularity of data distribution, thereby reconstructing a full PL model.

4.3.3.1 PL model hypothesis generation

To resolve the aforementioned locality problem, we propose incorporating a hypothesis-testing optimization into the piecewise model growing process. Instead of relying on a single initial model, M, a set of different growing models, $\{M_i'\}_{i=0}^N$, are hypothetically generated from M and each model, M_i, is hypothesized to approximate the targeted global model. Suppose that an initial PL model, $M(L, C) = M(\theta, \rho, a, b, c)$, is established with a given PP by Equation 4.1 and 4.2 and M's parameters are estimated as $(\theta_0, \rho_0, a_0, b_0, c_0)$ with its variance estimated to be $(\sigma_\theta^2, \sigma_\rho^2, \sigma_a^2, \sigma_b^2, \sigma_c^2)$ by Equation 4.7. Given M established with a PP, a hypothetical model, $M_i'(L_i', C_i')$, is generated by intentionally changing the initial sag position of the catenary curve, b_0, along the line direction of project curve, θ_0. Note that L_i' in M_i' is fixed as L (i.e., $L_i' = L$) and its initial parameters, (θ_0, ρ_0), are not altered in any of the hypothesized models. Thus, M_i' is produced only

by hypothesizing C_i' and thus the parameters of the hypothetical catenary curve of C_i' created by changing the sag position of C is described as

$$\begin{cases} a = a_0 + e_a \\ b = b_0 + db_i + e_b, \\ c = c_0 + e_c \end{cases} \qquad \begin{bmatrix} e_a \\ e_b \\ e_c \end{bmatrix} \sim N \left(\begin{bmatrix} 0 \\ 0 \\ 0 \end{bmatrix}, \sigma_0^2 \begin{bmatrix} \sigma_a^2 & & \\ & \sigma_b^2 & \\ & & \sigma_c^2 \end{bmatrix} \right) \qquad (4.15)$$

Where, we assume that the error vector, $e = [e_a \ e_b \ e_c]^T$, has normal distribution, N, with the statistical assumption, E(e)=0. In Equation 4.15, db_i is a dummy term used to change the initial sag position of b_0 to generate a hypothetical catenary curve model of C_i' that is given as $db_i = \{i = 0,1,2, \dots N | \Delta_{const} \times i\}$ where Δ_{const} is a constant value. Using Equation 4.15, N numbers of hypothetical model, $\{M_i'\}_{i=0}^N$, are produced, where the null hypothesis is a PL model with $db_0 = 0$ (i.e., $C_0' = C$).

4.3.3.2 Optimal PL model selection

Since the same PP is used for estimating the parameters of all the hypothesized models, the ordinary least squares method would not produce different estimation results for M even though b_0 is changed to M_i'. To address this problem, we adopt a non-linear least squares estimation with stochastic constraints to estimate the parameters of $\{M_i'\}_{i=0}^N$. The Gauss-Markov linear model with stochastic constraints is a well-understood theory used to integrate additional observation equations that come from another measurement (i.e., a different source than the original ones) in the form of stochastic constraints (Cothren, 2005). In particular, the stochastically constrained parameters are often used when the parameters must conform to some relationships arising from geometric characteristics of the corresponding model (Mikhail and Ackerman, 1983); in our case,

the adjusted parameters must conform to the overall geometric characteristics caused by changing b_0. To adopt the stochastically constrained least square estimation, we modify the normal catenary curve model by introducing two additional parameters, (a_1,c_1), to Equation 4.2. For convenience in notation, a hypothetical model, M_i', is denoted as the modified catenary curve model, C', without model index subscript, i. Thus, C' can be described as:

$$C'(a, b, c, a_1, c_1) = a + a_1 + (c + c_1)\cosh\left(\frac{X-b}{c+c_1}\right) - Z = e \quad e \sim N(0, \sigma_0^2 P^{-1}) \tag{4.16}$$

Equation 4.16, (a, b, c) shows the stochastically constrained parameters as $(\sigma_a^2, \sigma_b^2, \sigma_c^2)$ and (a_1, c_1) are introduced to estimate the corresponding supplementary quantity created by changing b_0 in Equation 4.15. The arrangement of Equations 4.15 and 4.16 in the form of the Gauss-Markov model with stochastic constraints can be expressed as the following matrix form:

$$\begin{bmatrix} y \\ z_0 \end{bmatrix} = \begin{bmatrix} A_1 & A_2 \\ K & 0 \end{bmatrix} \begin{bmatrix} \xi_1 \\ \xi_2 \end{bmatrix} + \begin{bmatrix} e \\ e_0 \end{bmatrix}, \quad \begin{bmatrix} e \\ e_0 \end{bmatrix} \sim N\left(\begin{bmatrix} 0 \\ 0 \end{bmatrix}, \sigma_0^2 \begin{bmatrix} P^{-1} & \\ & P_0^{-1} \end{bmatrix}\right) \tag{4.17}$$

where l is the number of constrained parameters; z_0 is the $l \times 1$ observation vector related to constraints; K is the $l \times l$ design matrix formed by the linear relationships between parameters and constraint observations; A_1 and A_2 are the associated coefficient matrices of size $n \times l$ and $n \times (m - l)$, respectively; e_0 is the $l \times 1$ random error vector of constrained parameters with weight matrix P_0; ξ_1 and ξ_2 are original and additional parameter vectors of size $l \times 1$ and $(m - l) \times 1$, respectively.

The parameters of all hypothetical models, $\{C_i'\}_{i=0}^N$, are estimated by Equation 4.1 and 4.16. An optimal model, C'^*, is selected which gives the minimum residuals between the model and PP, that is

$$C'^* = \arg\min_{\{C'_i\}_{i=0}^N} D(C'_i, PP) \qquad (4.18)$$

where D( ) is a function used to measure the average orthogonal distance between the model and given points. Figure 4.6 illustrates an example of selecting C'^* from hypothetical models, $\{C'_0, C'_1, C'_2, C'_3, C'_4\}$, that are generated by moving the sag position from db_0 to db_4 from b_0 where C'_0 is null hypothesis.
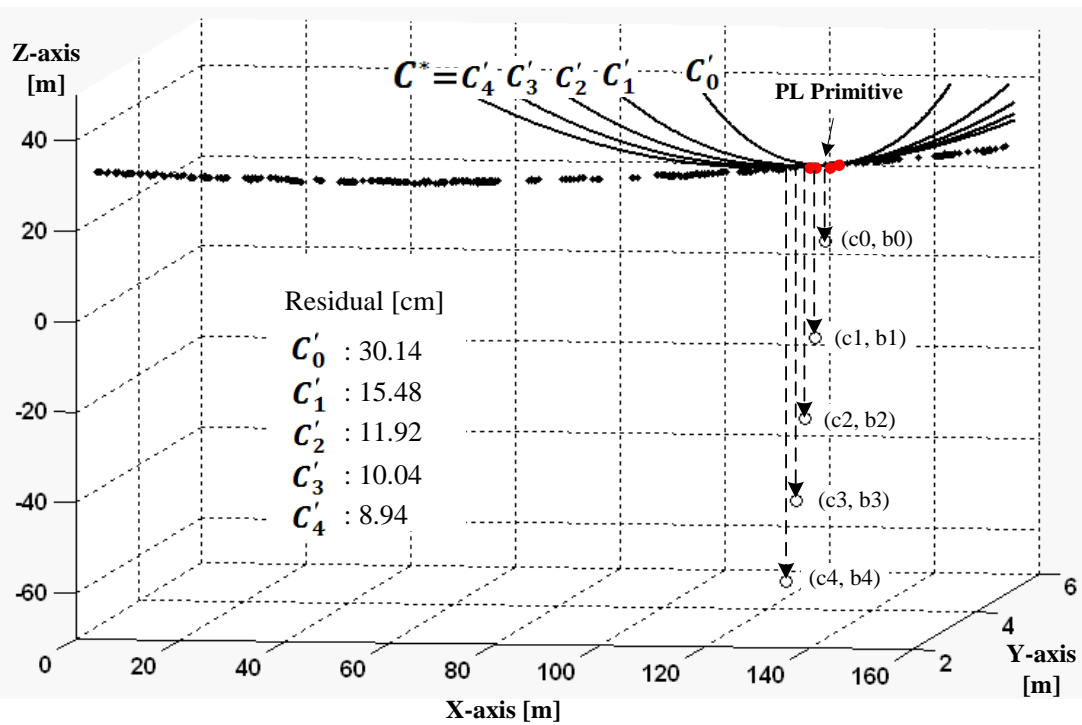
Figure 4.6: Possible alternative hypotheses from C'_0 to C'_4 determined by moving the sag position from b0 to b4 at the current PL primitive (red color) and the selection of the optimal power line model ($C'_4 = C'^*$) with the minimum residual.

4.3.3.3 Piecewise PL model growing

The PMG is accomplished by generating multiple hypothetical models and selecting an optimal model, which gives the best fitting result at each iteration step. Once C'^* is determined by the optimal hypothesis selection process, a 3D voxel (i.e., M_{ext}) is extended from C'^* based on its estimated model parameter and prespecified voxel size, with which the new ALS points, PP_{ext}, are obtained. M_{ext} and PP_{ext} are used as the null hypothesis for the next modelling growth. This process continues unless the null hypothesis (i.e., C_0') is not selected as the optimal model (i.e., C'^*). If C_0' is selected as C'^*, the growing process based on the hypothesis testing is terminated. In this case, new ALS points are collected as the model is grown through the extension of the physical dimensions of the current model. The parameters of extended model are estimated using the ordinary least square method from Equations 4.3 to 4.7. This non-hypothesis-testing process continues until the extended model captures no additional ALS data. Figure 4.7 illustrates an overall process of the progressive model growing. In Figure 4.7, the PL model is grown using a hypothesis-testing process that selects optimal models from (b) to (d). After (d), the non-hypothesis-testing process begins to extend the models from (e) to (h). As the non-hypothesis-testing process is terminated, a final PL model is reconstructed, in which the entire ALS points belonging to the model are detected, as shown in Figure 4.7(h).
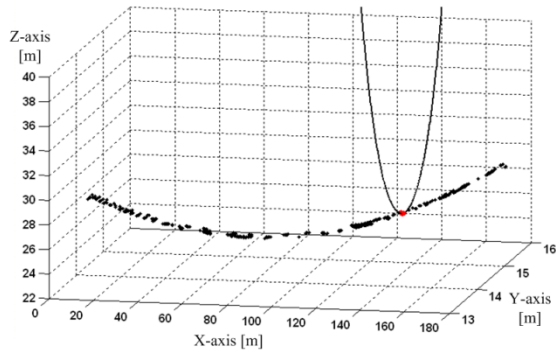
(a)
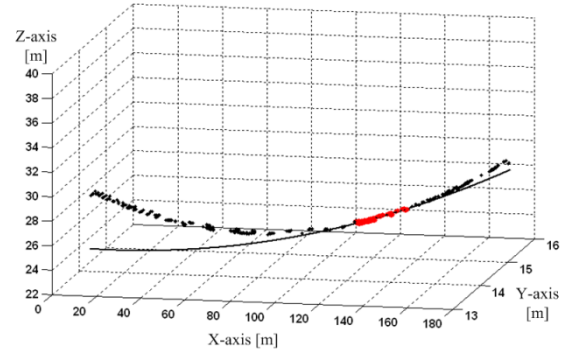
(e)
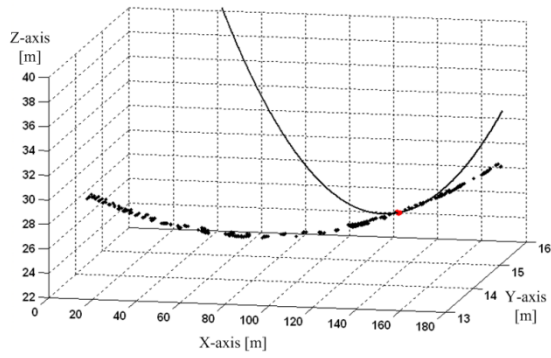
(b)
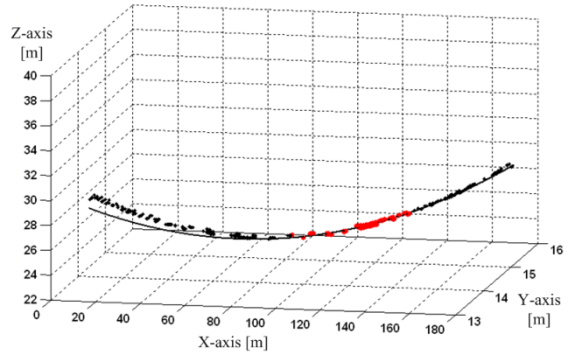
(f)
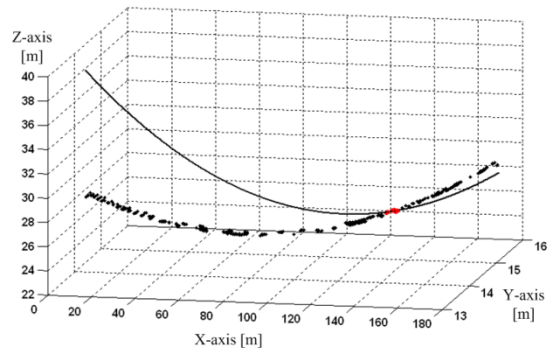
(c)
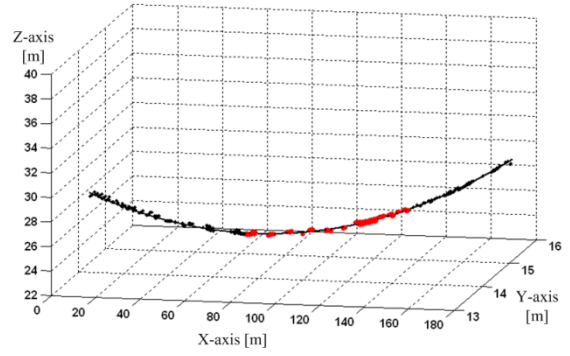
(g)
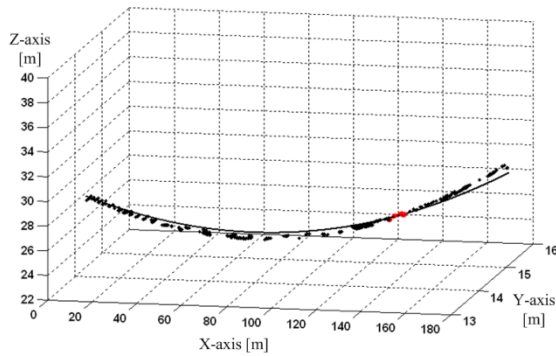
(d)
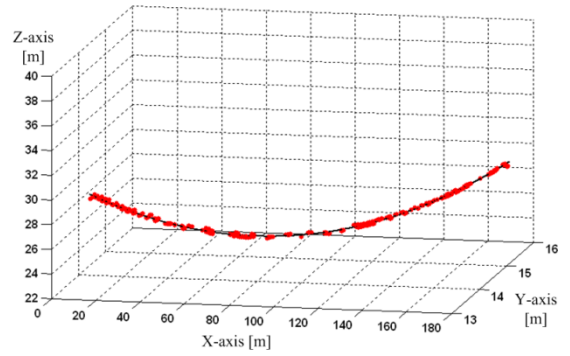
(h)

Figure 4.7: Optimal PL model generation (black coloured line) and its corresponding PL points (red coloured points); (a) initial PL model, (b), (c), and (d) PL models from hypothesis-and-test, (e), (f), (g), and (h) PL models from non-hypothesis-and-test, (h) final PL reconstruction.

4.3.3.4 PL model validation

In PMG, the line primitive, PP, must grow from a CP to produce a complete PL model. Thus, if a CP is wrongly detected from a non-PL object, it results in a commission error in the PL modelling results. To resolve this problem, PMG incorporates a PL model validation process to investigate if the PL model generated from a CP represents a true PL object. We create two cylinders around the PL model where the inner cylinder has radius of r_{in} (0.5m) and is surrounded by the outer cylinder, which has a radius of r_{out} (1m) as shown in Figure 4.8. These two cylinders are used as searching spaces to capture the member points of each cylinder. In general, the PL is isolated from its surroundings in all directions and thus most of the points found in the cylindrical search are located in the inner cylinder, while very few points are present in the outer cylinder. However, this is not a valid assumption for non-PL objects that are spatially connected to their surroundings in certain direction and thus the number of points captured in the outer cylinder increases relative to the PL's case. The model validation system used to classify PLs into two classes (i.e., PL and non-PL primitive) is conducted by analyzing the different characteristics between PL and non-PL objects with respect to the spatial distribution of ALS points captured in two cylinders.

In a way similar to that proposed by Kittler and Illingworth (1986), we measure the residuals between the ALS points captured by the two cylinders and the PL model given. A range histogram is created in two parts, each of which is formed with the member points of two cylinders respectively and modeled with a normal distribution. Then, we measure the probabilistic

error, H, caused by modelling the residual histogram into two normal distributions based on the following formulation.

$$H = \frac{1 + \log 2\pi}{2} - q_{in}\log q_{in} - q_{out}\log q_{out} + 0.5 \times (q_{in}\log\sigma_{in}^2 + q_{out}\log\sigma_{out}^2) \qquad (4.19)$$

where N_{in}, and N_{out} are the number of points that are captured by inner and outer cylindrical search spaces respectively; q indicates probability; $q_{in} = \frac{N_{in}}{N}$, $q_{out} = \frac{N_{out}}{N}$; σ_{in}^2 and σ_{out}^2 are variances obtained by using the corresponding observation in each search space. After measuring H for the PL model, the PL is accepted as valid model if H is less than pre-specified, H_T, otherwise it is rejected. H_T is pre-computed as 0.514 using Equation 4.19. This value is obtained based on the assumption that the points in cylindrical searching space are located with the same accuracy in the inner and outer cylinder (i.e., $q_{in} = q_{out}$ and $\sigma_{in} = \sigma_{out}$) and consider σ_{in} to have a vertical accuracy of 15cm horizontally and 10cm vertically for the LIDAR data for the corridor mapping (Ussyshkin and Smith, 2007).
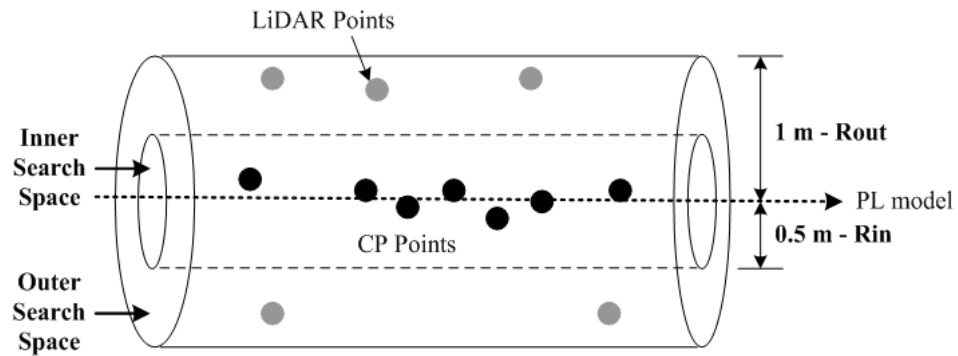
Figure 4.8: Two cylindrical search spaces generated for PL model validation.

4.4 Experiments and results

The performance of the proposed progressive model growing method was evaluated with real ALS data. The test data contains a complex PL corridor scene which is located in the east of Folsom, California, USA and covers 638.3m (length) × 117.3m (width). Figure 4.9(a) shows the Folsom data where the ALS points are colourized according to their corresponding object classes. The classification was manually conducted using TerraScan software to produce the reference data for evaluating the performance of the proposed method. The PL systems in the Folsom data show a high degree of scene complexity, which would cause difficulties in PL reconstruction. The scene contains various PL voltage types (a mixture of low and high voltages), which include transmission, sub-transmission and distribution lines. Accordingly, the scene has a broad range of PL lengths and distances between PLs and catenary curve characteristics. Moreover, some different types of PLs run in parallel or some cross each other in different directions.

(a)

(b)

(c)
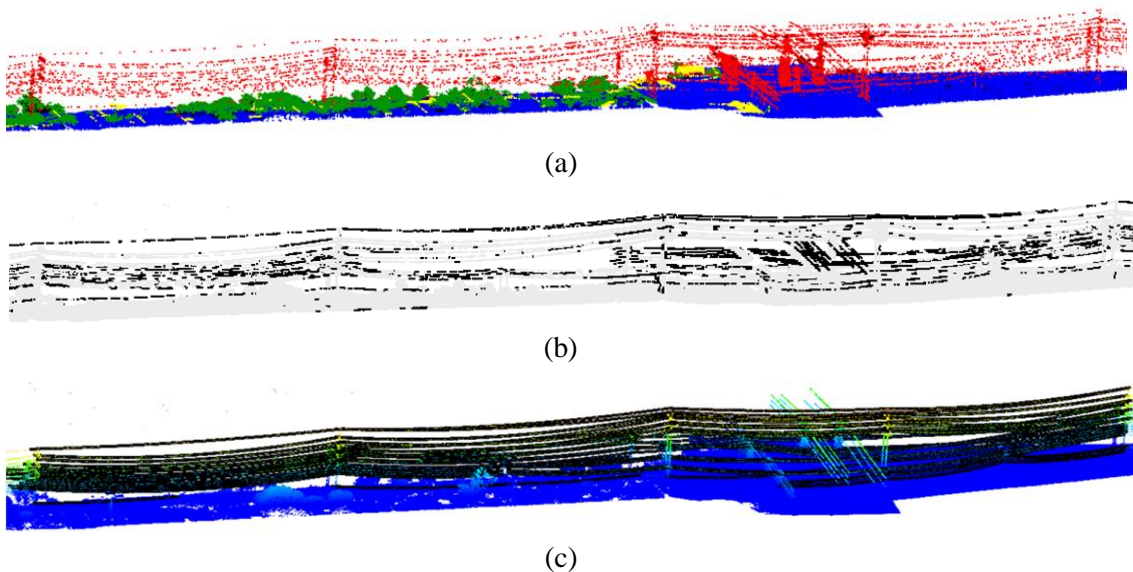
Figure 4.9: (a) Raw airborne laser scanning data set, (b) CP detection results (black color), and (c) 3D PL reconstruction (black color) in the whole urban area.

The Folsom data was acquired by Riegl's LMS Q560 laser scanner, which recorded 4-5 multiple returns from a single shot in August, 2007. The ALS system was attached to a helicopter-borne platform at an altitude of 121.9m above ground level with a speed of 23.15m/s, and utilized a scanning mechanism with a rotating polygon mirror and a ground-measuring pattern with parallel scanning lines. Its swath width is 190 m and the size of the laser beam foot print is 6.1cm with 0.5mrad of laser beam divergence. Approximately 1.8 million laser points at an average point density of 16 (points/m^2) were collected and the point distance on the PLs ranges from sparse (0.83m) to dense (0.11m) with an average distance of 0.32m.

4.4.1 Overall PL modelling performance analysis

We evaluated the detection rate of CP extraction by comparing the result with classified PL points in Figure 4.9(a). The detection rate was measured for two criteria, completeness and correctness, by counting the following three factors: (a) TP (True Positives), which are the number of CP points that are commonly found in both the reference and the result; (b) FN (False Negatives), which are the number of CP points that are found only in the reference, but not in the result; (c) FP (False Positives), which are the number of CP points that are found only in the result, but not in the reference data. These evaluation measures are described as:

$$\text{Completeness (\%)} = \frac{\text{TP}}{\text{TP} + \text{FN}} \times 100$$

$$\text{Correctness (\%)} = \frac{\text{TP}}{\text{TP} + \text{FP}} \times 100$$

(4.20)

A total number of 56,396 points were labeled as PL points in the reference data. Figure 4.9(b) presents the CP detection results, which detected 25,303 CP points using the proposed detection

algorithm. As we compared the reference data to the CP detection result, TP, FN, and FP are counted as 19,182, 37,214, and 6,121 points, respectively. By Equation 4.20, the completeness was measured as 34.0% and the correctness was measured as 75.8%. As shown in the comparison results, the proposed CP detection method intends to produce a higher rate of correctness by producing fewer FP, while more FN leads to lower rate of completeness. The large amount of FNs in CP detection is mitigated as PL models are properly grown. The relatively low amount of FP is eliminated through the PL model validation procedure and contributes to speeding up the modelling process.

The results of PL reconstruction obtained by the PMG method are shown as thick black lines (i.e., PL result) in Figure 4.9(c) and its quantified success rate is presented in Table 4.1. 151 PLs along the main direction were manually detected to produce a reference map for the PL models. Relying on intensive visual inspection, we carefully classify the modelling results produced by PMG into five different categories: complete, partial, under, over modelling and un-detection. A PL model produced by PMG was considered as a complete modelling if the model passes through the location of POA (Point of Attachment) where the model is connected to its corresponding insulator. An investigator visually checked the location of the POA. However, in many cases, it was hard to find the exact location of the POAs. In this case, we inferred the POA's locations based on our heuristic knowledge to judge if it passes at or around the POA. A modelling result was recognized as partial modelling if a reconstructed model reconstructed did not reach its POA location, as under-modelling if two or more PLs were modelled as one model, as over-modelling if the actual PL was split into many models, or as an un-detected error if it was completely missed by PMG. Table 1 shows the overall PMG performance with the five classes of modelling results and shows that the PMG achieved a 96% complete modelling rate with a 4% error rate. All

models were reconstructed from PL objects and none of the models generated were from non-PL objects.

Table 4.1: Overall PMG performance of PL reconstruction.

	Total	Complete Modelling (CM)	Partial Modelling (PM)	Under Modelling (UM)	Over Modelling (OM)	Un-Detection (UD)
Number	151	145	2	0	3	1
Rate (%)	100	96	1.3	0	2.0	0.7

We also evaluated the quality of the modelling results by comparing the PL points (56,396 points) that were manually classified to the ones captured by PL models reconstructed by PMG. A total of 60,434 points were collected by the 151 PL models generated, in which 56,100 points were recognized as TP, while 296 and 4,335 points were recognized as FN and FP respectively. Thus, a completeness of 99.5% and a correctness of 92.82% were measured by Equation 4.20. These results demonstrate that PMG is able to achieve a high success rate for both completeness and correctness. A relatively high rate of FP detection compared to FN occurred since the complete models over-grow beyond POA. FN detection was mainly caused by partial modelling errors. Another measure of the modelling performance that was investigated is the root-mean-square error (RMSE) of the residuals between manually classified PL points and PL models produced by PMG. Over 145 complete PL models were obtained, and the RMSE in the X-Y-Z (3D) plane was measured as 5.2cm, while RMSE in X-Y (2D) plane was measured as 2.9cm. The maximum 3D RMSE found for each PL was measured as 7.8cm, which is less than the typical positional accuracy of the ALS data used for PL corridor mapping (Ussyshkin and Smith, 2007). The high modelling accuracy obtained by PMG demonstrated its potential to automate the modelling process.

4.4.2 Sub-scene based performance analysis

The performance of a modelling algorithm using remote sensing data usually varies in accordance with scene complexity; higher performances are achieved over images with lower complexity. To analyze the sensitivity of PMG performance to scene complexity, we divided the Folsom test data into 7 sub-scenes, each of which represents one span of a specific voltage type shown in Figure 4.10. The variety of voltage types in 7 sub-scenes ranges from a 7kv low voltage distribution line to a 230kv high voltage transmission line. The span lengths of the test sites vary from 62.4 to 178.1m between consecutive pylons, and heights differ from 9 to 42m above ground level.
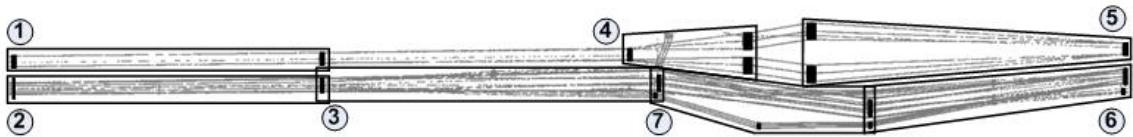
Figure 4.10: Selected 7 sub-scenes of Folsom test data.

Figure 4.11 shows the side views of the PLs in selected test sites and the corresponding reconstruction results. Table 2 describes the characteristics of each site with respect to PL length, point distance, the number of wires and the number of bundle wires. The bundle wires consists of several conductor cables connected by non-conducting spacers to reduce corona losses and audible noise. A number of bundles are usually used for high voltage lines. The PLs comprising of bundle wires are located close to one another at a distance of less than 0.3m orthogonal. If the presence of random errors in ALS data is considered, the distance between PLs in a bundle wire would be smaller than 0.3m. This short distance might cause difficulties for PMG in properly separating individual PLs from each other within a bundle wire, which results in the under-

modelling of PLs (i.e., representing two or more wires with one model) as shown in Figure 4.12(a).
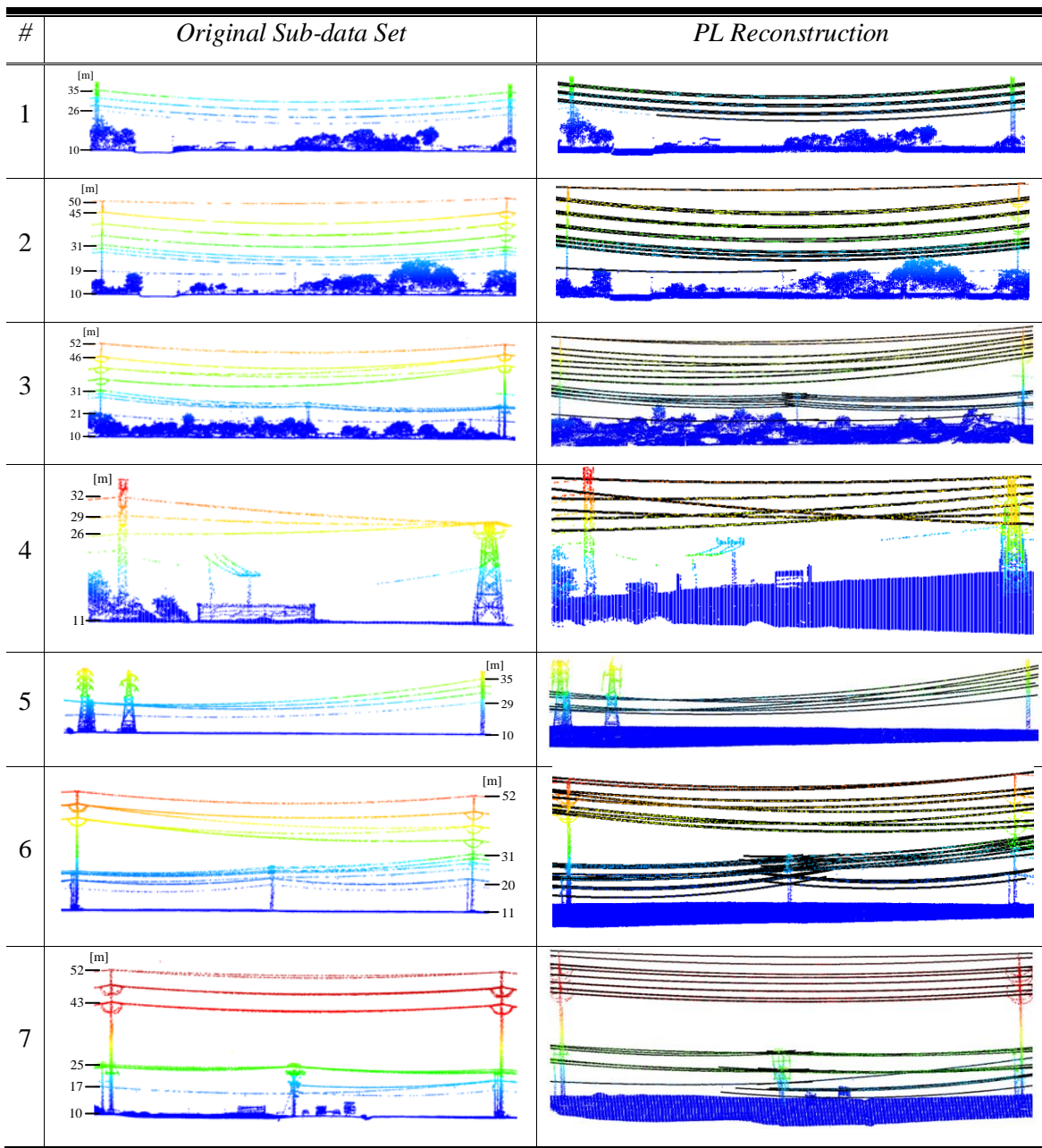
Figure 4.11: Side views of 7 sub-scenes (left) and corresponding PL modelling results coloured in black (right).

Table 4.2: PL modelling results obtained by PMG.

Site	Span Length [m]	Average Point Distance per PL [m]			CP Detection (%)	Bundle Wire	Total Lines	CM	PM	UM	OM	UD
		Ave	Min	Max								
1	162.7	0.45	0.37	0.85	79.5	0	7	6	1	0	0	0
2	162.9	0.38	0.27	0.54	23.0	6	21	19	0	0	1	1
3	178.1	0.34	0.25	0.53	24.4	6	28	26	1	0	1	0
4	62.4	0.18	0.14	0.21	62.9	0	6	6	0	0	0	0
5	165.8	0.29	0.25	0.52	80.2	0	7	7	0	0	0	0
6	135.8	0.30	0.17	0.83	19.3	6	36	35	0	0	1	0
7	112.4	0.16	0.11	0.44	22.6	6	32	32	0	0	0	0

Table 4.2 also indicates that a negative correlation between the number of PLs and CP detection rate. The decrease in the CP detection rate might be affected by occlusions that usually occur more often as the number of PLs increases. If no CP is detected over a PL, as shown in Figure 4.12(b), the under-modelling error occurs, as there is no primitive existing to trigger the model growing process. Also, a lower CP detection rate indicates a weaker presence of linear properties, which might degrade the overall performance of the PMG method. Table 4.2 also shows the range of point distances between consecutive points over PLs from 0.11m (dense point density) to 0.85m (sparse point density). The average point distance ranges from 0.16m to 0.45m. Larger point distances are normally detected in lower voltage PLs that run below high voltage ones due to the occlusion effect. This might induce large data gaps within a PL, as can be seen in Figure 4.12(c), which lead to the early termination of the model growing process due to the lack of measurements detected by the extended growing model and this results in the partial modelling error.

Table 4.2 summarizes the evaluation results of PMG's performance on each site. As shown in Figure 4.11, Site 1 shows the lowest scene complexity, where only one voltage type of PL is

present in the scene. The distribution of PLs in Site 1 is one of the simplest configurations, as it is comprised of only 7 PLs and does not have a bundle wire. Similar characteristics to Site 1 can be found in Site 4 and 5, which have 6-7 PLs and only one voltage type. Due to this, Sites 1, 4 and 5, which have the smallest number of PLs show a higher CP detection rate—from 62.9 to 80.2% compared to the other sites. The combined effects of the number of bundle wires and occlusions produced a relatively higher success rate of PL reconstruction over these sites and except for one PL error in Site 1, all the modelling results were recognized as the complete model. The partial modelling error in Site 1 was caused by a large data gap of more than 7m present at the end of the PL. The catenary curve of Site 1 shows a clear symmetric geometry, and almost straight lines between the different types of pylons can be found in Site 4, whereas the catenary curve of the PLs in Site 5 is non-symmetric. This suggests that the PMG's performance is not affected by the catenary curvature of the PLs.

The PLs in Site 2, 3, 6, and 7 have more complex structures with various PL voltage types and a number of bundle wires, which caused various types of modelling errors. In these sites, the sub-transmission lines diverge in different directions from one of the pylons and the distribution lines are located close to the vegetation area. 3.3% of modelling errors occurred over these four sites, which corresponds to 83% of total modelling errors. The location of a large data gap of more than 7m in PLs caused the partial modelling error if the data gap occurred at the end of PL (Site 3) otherwise it produced over-modelling errors (Site 2 and 3). In Site 2, one of the distribution lines passes through a vegetation area. This caused the undetected error, since the reconstructed model was rejected by the PL model validation process due to the large amount of vegetation points contained in the reconstructed model. In Site 6, the over modelling error also occurred when the parameters of an initial PL model were not correctly estimated due to data

errors, which misled the PL model growing direction, and thus the rest of PL points were captured by the new model.

In all these sites, the transmission with 6 bundle wires and sub-transmission lines run together. However, all lines were well separated and no under-modelling errors occurred. The determination of optimal voxel size, particularly its width and height, used for PL model growing plays critical role in preventing the PMG from generating under-modelling errors. In this study, we used 0.5m (width)×0.5m (height)×5m (length) as the voxel size for model growing by taking into account the ALS's typical positional accuracy for PL corridor mapping (Ussyshkin and Smith, 2007) and the distance between PLs in the bundle wire. Table 4.2 shows that this assumption works effectively without producing under-modelling errors. However, it would be possible to cause the under modelling error when an optimal value of the voxel size is hard to pre-specify. In Site 6, PLs are densely distributed in the sub-transmission line level. This causes a large occlusion along a downward direction of height, so that the average point distance over the PLs ranges from dense (0.17m) to sparse (1.83m). In Site 7, PLs are located immediately above buildings and are distributed in different directions between spans in the lower voltage PL structure. Although these difficulties exist, Table 4.2 indicates that PMG successfully reconstructed PL models over Site 6 and 7.

Single PL Extraction in
Bundle conductors

Tower
Structure

(a)

Detected PL Candidate Points

(b)

PL Models

Data Gap (~12 m)

Tower

Vegetation

(c)
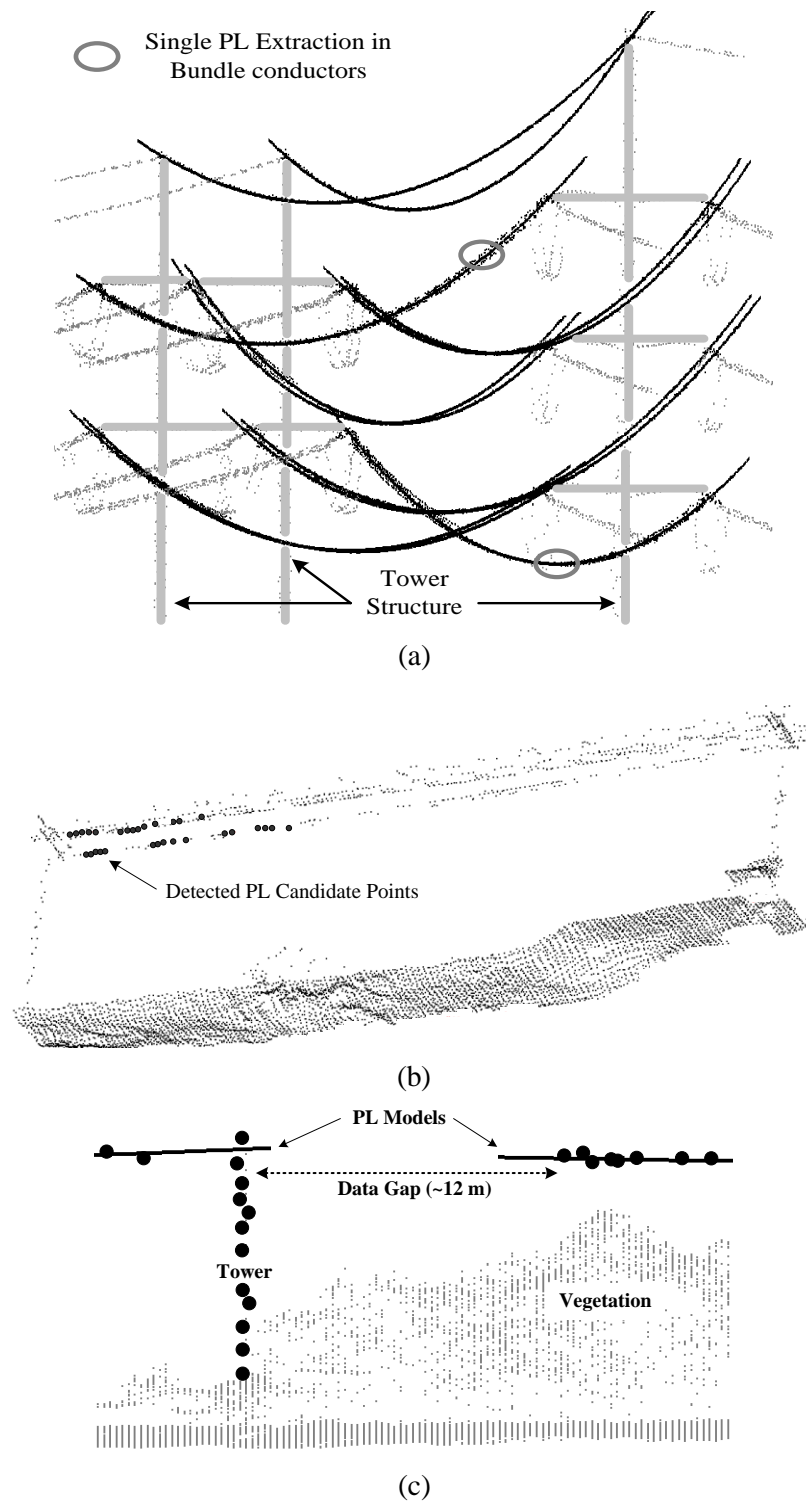
Figure 4.12: Examples of the limitations of 3D PL reconstruction due to (a) bundle wires, (b) low
detection rate of power line candidate points, and (c) low point density on PLs.

CHAPTER 5

3D power line model rectification: Inner and across span analysis

The previous chapter introduces the main aspect of PL model reconstruction. However, it still provides modeling errors such as partial-, under- and over-modeling errors, which might be insufficient for the precise PL risk analysis. To move to correct the incompletion of PL models, their rectification process is performed based on the inner and across span analysis. In the inner span analysis, individual PL models of each span are evaluated based on the MDL theory and then erroneous PL segments are replaced by precise PL models, thereby correcting under- and over-modeling errors. An important component of this process is the ability to estimate the degree of corruption of PL points using regression analysis and predict suitable model parameters especially under the windy environment. In the across span analysis as a subsequent step, detecting precise start and end positions of PL models, called Point Of Attachment (POA) is the most key issue to correct partial modeling errors as well as refine PL models. For this, connection of PL models is evaluated by generating their intersection positions and selecting optimal connections with minimum positional errors over the across spans. Consequently, the proposed method is capable of achieving the geometric and topological completion of PL models over the whole PL network.

5.1 Introduction

In Chapter 4, we proposed an automated process to reconstruct power line (PL) models from LiDAR point clouds. Although our method (PMG) has demonstrated promising perspectives in wire modeling, resulting models still include modeling errors, which should be rectified in order to increase its practicality in the PL risk management. In general, we can categorize PL modeling errors into three groups: under-, over- and partial-modeling errors. Figure 5.1 illustrates examples of each type of representative errors produced by PMG on real PL datasets. As shown in Figure 5.1, the "under-modeling" errors occur when PLs are reconstructed with a lower number of PL models compared to their actual count, resulting in producing over-simplified PL models (Figure 5.1(a)). The "over-modeling" errors is the opposite of under-modeling errors, which are produced if a PL is reconstructed with more than one model (Figure 5.1(b)). Even though PLs are modeled without under- or over-modeling errors, there is still a case where the modeling process converges early. This leads that reconstructed model is not able to reach PL's true end positions that are associated with insulators and pylons, often called as POA (Point Of Attachment). This error refers to the "partial-modeling" errors. In this chapter, we propose a sequential post-processing method, which rectifies the modeling errors by introducing two steps of span analysis; inner span analysis and across span analysis. The inner span analysis aims to identify and rectify the under- and over-modeling errors produced within a span, while the across span analysis concentrates on correcting the partial errors across linked spans. A final modeling outcome produced through the sequential span analysis is an improvement of modeling accuracy to PMG's results.
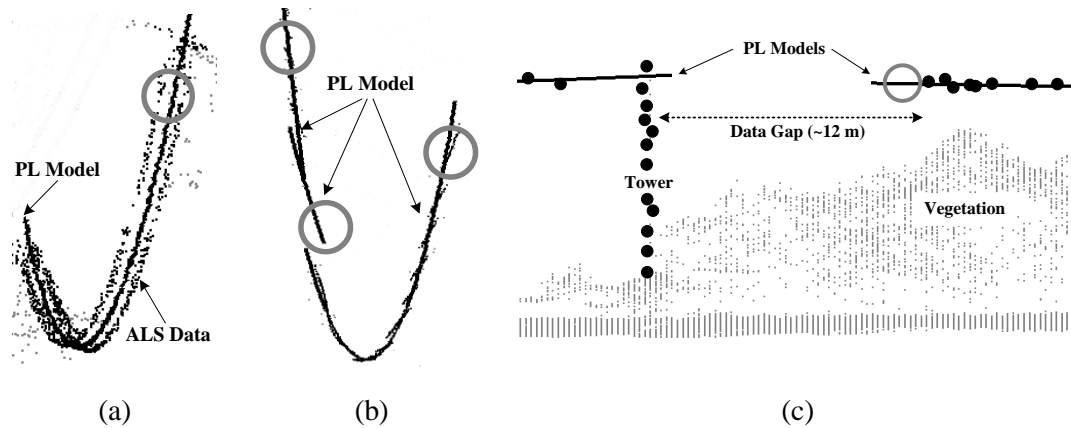
Figure 5.1: Examples of typical error types (denoted by circle) in reconstructing PL models: (a) under, (b) over, and (c) partial PL modeling error.

In practice, a POA is known to be important to the effective PL risk management. The main reason for this is that the POA can be used as an anchor position in the simulation of conductor blowout for the identification of PL risks. If POAs are detected with an acceptable accuracy (in practice, about 30 cm), it allows us to precisely assess a clearance quantity caused by encroachments of natural and/or artificial objects to PLs. Thus, knowing the POA positions is critical to conduct PL clearance analysis (Sohn and Ituen, 2010). POAs can usually be divided into two types: CAP (Cable Attachment Point) and IAP (Insulator Attachment Point). The CAP denotes a connection position between a PL and its associated insulator, while the IAP indicates a connection position between an insulator and the corresponding pylon structure. In this study, for the purpose of PL model rectification, the POA is defined as an intersection position between two consecutively lined PLs, which becomes either CAP or IAP according to insulator types. The insulator types are usually categorized as two different geometrical structures; suspension and dead-end types. The suspension type which normally exhibits a line or V shape is designed to allow two linked PLs to connect with an insulator at one point. In the dead-end type, the consecutive PLs are connected to different insulators and these insulators are to be connected each

other at one point. Therefore, the intersection point becomes the CAP in the suspension type and the IAP in the dead-end type.

5.2 Motivation

In the previous chapter, 3D PL models were reconstructed based on the proposed modeling method of piecewise model growing (PMG). Using the complex urban sub-data set, PMG demonstrated that it is able to achieve a high modeling success rate of about 96%. However, it might be insufficient for a complete risk analysis of PL networks as the method still produced some modeling errors. Even though the produced amount of errors may not be considered significant, these errors should be minimized as any small failure in PL modeling might hinder precise risk analysis and ultimately cause a critical massive power outage. We believe that the potential error sources affecting the PL modeling arise from irregular distribution of laser points reflected along PLs (PL points). The irregular distribution of PL points is caused by several factors. Habib (2009) discussed factors influencing the irregularity of laser point spacing (spatial distribution) with two error types: systematic biases and random errors. The systematic biases are mainly due to the insufficient calibration of individual sensors associated with point cloud acquisition (e.g., laser sensor, IMU, GPS) and misalignment between those sensors. Thus its positional accuracy is usually corrected through an appropriate sensor calibration process. On the other hand, the random errors are considered as a white noise in a stationary process, which follows a normal (Gaussian) distribution with identical means and variances. It is true that both systematic and random errors are one of main causes affecting the positional accuracy of laser point clouds, which lead to the irregular distribution of point clouds. However, these errors are usually much cared during sensor calibration process and the distribution characteristics of these

errors is given as *a priori* knowledge of the data acquired after the calibration process is finished. We believe that there are more factors causing the irregularity of spatial distribution of PL points than the systematic and random errors, which also causes problems in PL modeling. This is because characteristics and amount of these errors are hard to be known in advance and are usually unpredictable. These errors are related to the presence of occlusion, the nature of thin linear objects, as well as the nature of moving objects (i.e., the positions of PLs are changed by wind speed). All these factors are associated with the increase of the irregular distribution of PL points unexpectedly, which are explained in detail as follows:

Occlusion: PL networks are constituted in a complex manner where many PLs delivering different voltages are placed closer together in the same direction, but with different heights or run in different directions. The complex spatial configuration often occludes visibility of some parts of PL structure by themselves or by neighbouring structures like insulators or pylons, and thus causes missing of laser returns along PL. This occlusion leads to a wide range of data gaps. For example, average point distances per PL vary from dense (0.17m) to sparse (1.83m), even though PLs are located in the same span due to the occlusions (Jwa and Sohn, 2012).

Thin linear object: As PLs are a thin object with a small diameter in the level of several centimetres, it is difficult to hit them with entire laser footprints. This leads that the strength of return signals from PLs considerably decreases, which causes the missing of returned laser echoes. For example, aluminum conductors usually have about 2 cm in diameter (Shoemaker and Mack, 2007). On the other hand, the diameter of laser beam footprint becomes at least 5 cm with 0.5 mrad of laser beam divergence at the flight height of 100 m. Where, in the PL corridor mapping, the flight height of ALS is normally more than the 100 m above the ground level because

saturation effects in too strong return signals sometimes happen (von der Gathen, 1991). The other important consideration is that PLs are linear features unlike area features such as the surface of building rooftops or roads. According to Jelalian (1992), the strength of signal reflected from a linear feature is inversely proportional to the third power of laser range, R^3, compared to R^2 for the area features. As a result, the probability that energy of returning laser pulse is higher than a detection threshold value predetermined decreases and thus PL points will be sparsely recorded with the irregular distribution. Note that the threshold value plays an important role in discretely counting the number of laser returns (Baltsavias, 1999).

Moving object: PLs are moving objects as their locations vary due to dynamic load of external forces such as winds, resulting in the occurrence of oscillatory. Statistically, if wind speed is over 40 km/h in the PL corridor area, power outages start to frequently occur due to the undesired events such as vegetation encroachments (Betz et al., 2009). Under the situation of strong wind blowing, PL points acquired are plainly corrupted by the movements of PLs. That is, the movements cause the shape distortions of PLs, which original shape is formed with a straight line in the horizontal plan and catenary curve in the vertical plan. Furthermore, as the flow of wind is not constant, the degree of the shape distortions varies over the same corridor area as well as even within the same span. It is an ideal situation to record weather conditions including wind speed while PL point clouds are acquired using an weather probe mounted on airborne system or placed on the ground. However, we have observed that the weather data is often not used in practice (like the case of our current study) or its sampling rate is too low or its accuracy is not reliable. It is hard to estimate wind speed and its effects to modeling accuracy in advance.

5.3 Methodology

Figure 5.2 illustrates the overall process of PL model rectification proposed, which is comprised of two steps: inner span analysis and across span analysis. The basic idea of the inner and across span analysis is closely related to solving the problem of model selection for rectifying PL modeling errors produced by PMG method. An optimal model (thus recovering modeling errors) is found in hypothetical model space that is implicitly generated with given initial models. For the inner span analysis, the optimal model is selected among candidate models as the best representation to its inliers. Individual PL models of each span are thus evaluated with the objective to correct under- and over-modeling errors. Where, the candidate models are generated based on the well-known split and merge approach. We adopt the theory of Minimum Description Length (MDL) for the verification of PL candidate models. The process of MDL-based verification favours how to optimally fit the model to the data and also to simply explain the data with the model, resulting in the selection of optimal PL model. Note that all of PL models are evaluated to detect and correct modeling-errors based on the MDL-based verification. In the across span analysis, detecting precise POAs is the most key issue to correct partial modeling errors as well as refine PL models by finding their start and end positions. For fulfilling this purpose, we first identify a conjugate pairs consecutively connected over across spans. Their associated POAs are then estimated based on a least squares adjustment. As a result, the proposed method is capable of achieving the geometric and topological completion of PL models, thereby correcting PL modeling errors.
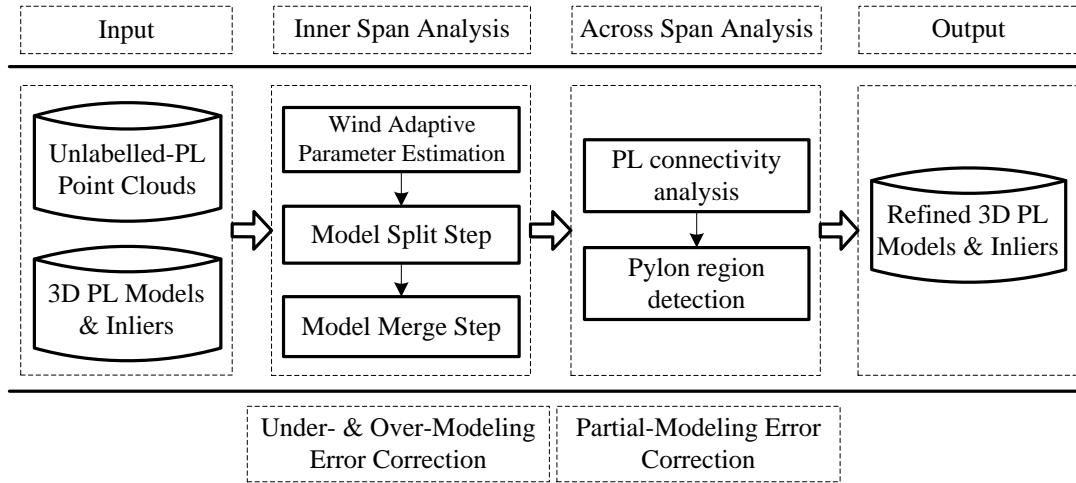
Figure 5.2: Schematic diagram of the inner and across span analysis proposed: 3D PL models and inliers as well as non-PL points are used as an input.

5.3.1 Inner PL span analysis

This section describes a method of correcting PL modeling errors, under- and over-modeling errors, in the inner PL span domain. The important aspect of proposed method is the ability to deal with noisy PL points corrupted by wind effects in correcting PL modeling errors based on a regression analysis. The detailed description and a mathematical formulation used in the inner span analysis are discussed in the following sub-sections.

5.3.1.1 MDL criteria formulation

As we have discussed in detail in Chapter 3, the MDL criterion function is basically composed of two terms, model closeness and model complexity, which is to be optimized for the best model selection of objects of interest by solving model selection problems. This section discusses about how the criterion function is formulated for the selection of optimal PL model, which leads to the correction of PL modeling errors. The model closeness $\mathcal{L}(D|M)$ is designed to

measure a deviation (i.e., goodness-of-fit) between a PL model M and the corresponding data D. This deviation can be assumed to follow a Gaussian-distribution $N(\mu, \sigma^2)$ with expectation μ and variance σ^2. The description length of $\mathcal{L}(D|M)$ is formulated as:

$$\mathcal{L}(D|M) = \frac{\Omega}{2\ln 2} \tag{5.1}$$

Where, Ω denotes the weighted sum of the squared residuals between M and D, $[D - M]^T P[D - M]$ in the matrix form.

The model complexity $\mathcal{L}(M)$ is designed to measure how many PL models Ms are used to represent the given data D. This can be formulated by specifying minimum number of observations on a model, if the model's length is known (Li 1992). Suppose that ε means a spatial resolution for expressing how close points are distributed each other over a PL model M. The probability that a point is randomly located on the M with a certain length l is then $\frac{\varepsilon}{l}$ and its description length becomes $\log_2\left(\frac{l}{\varepsilon}\right)$. Where, the resolution can be approximated as an average distance between PL points in the given PL models. For the estimation of model parameters, the minimum number of PL points m is required. Therefore, we can write the model complexity $\mathcal{L}(M)$ for expressing a PL model M in the following form:

$$\mathcal{L}(M) = m\log_2\left(\frac{l}{\varepsilon}\right) \tag{5.2}$$

As a result, based on the MDL theory, minimizing the cost of the criterion function combined by two terms leads to the selection of an optimal model M* given in the hypothetical model class Φ as:

$$M^* = \arg\min_{M \in \Phi} \{ \mathcal{L}(D|M) + \mathcal{L}(M) \} \tag{5.3}$$

The minimization of Eq. (5.3) means that the MDL criterion function should favour two cases: (1) the smaller discrepancy between PL models *Ms* and the given data *D*, (2) the simple representation of *Ms* in the given *D*. In the other cases, the criterion function penalizes *Ms*, so that its cost value increases. Therefore, under-modeling errors that cause the large discrepancy between *Ms* and *D*, and over-modeling errors that produce multiple model segments lead to the increase of their description length. That is why, in the MDL framework, incomplete PL models converge to the optimal models by correcting their undesired modeling errors.

5.3.1.2 Wind blowing effect in PL corridor area

A PL is a hanging object attached to its associated pylon structure and has a freedom to a swing. Under the strong windy environment, PLs dynamically move due to high wind loading. The wind blowing effect leads that measurements representing PLs are inevitably corrupted by their movements during data acquisition from airborne LiDAR system. This causes the severe noisy distribution of PL points and thus affects the performance of PL modeling as follows:

First, PL modeling accuracy (RMSE) measured as the discrepancy between PL models and the corresponding data is significantly degraded by the wind blowing effect. In the stationary case, the typical 3D positional accuracy of data used for PL corridor mapping is approximately 10~15 cm (Ussyshkin and Smith, 2007). In order to investigate how much the quality of PL data is degraded according to wind blowing, the relation between wind speed and modeling accuracy was made as shown in Figure 5.3. Where, we have collected part of the wind information for three corridors, 20023 for 161 kV, 20130 for 345 kV, and 24051 for 345 kV, from the utility company.
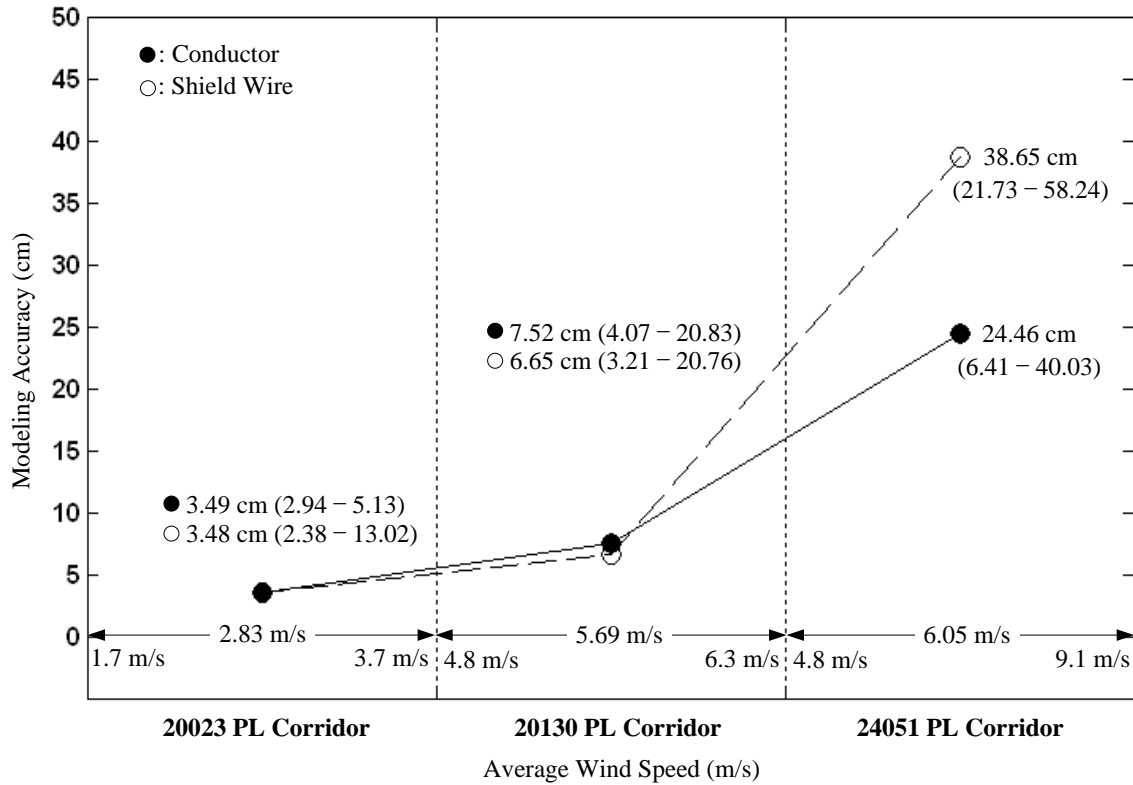
Figure 5.3: Variations of PL modeling accuracy [cm] with respect to wind speed [m/s].

20 spans of each corridor were tested and parameters of each PL model were estimated based on Eq. (4.1) and (4.2) in Chapter 4 using PL points which were manually segmented. In Figure 5.3, as the average wind speed increases from 2.83 m/s to 6.05 m/s over the three corridors, RMSE of PL models suffers by going up to 25 cm for conductors and 40 cm for shield wires. These measures indicate that it is hard to collect precise airborne LiDAR data for PL corridor mapping under the certain wind speed, for instance over 24051 corridor in Figure 5.3. Thus, the strong correlation between wind speed and modeling accuracy exists. In the 20130 and 24051 corridor, two corridors have a similar PL structures (i.e., single-circuit with bundle conductor) supporting 345 Kv and their average wind speeds show only small different. However, the RMSE of PL

models suddenly increases in the 24051 corridor compared to one of 20130 corridor (i.e., more than 3 times in conductors and more than 6 times in shield wires). This is because wind blew very dynamically with high strength and large variations of wind speed especially over the maximum wind speed of 20130 corridor (6.3 m/s). This leads that the impacts of wind blowing to PLs vary in various directions even at the constant wind speed. In addition, there might be a limitation in measuring accurate wind speeds using a low cost wind sensor under the situation of a wide variety of wind blowing.
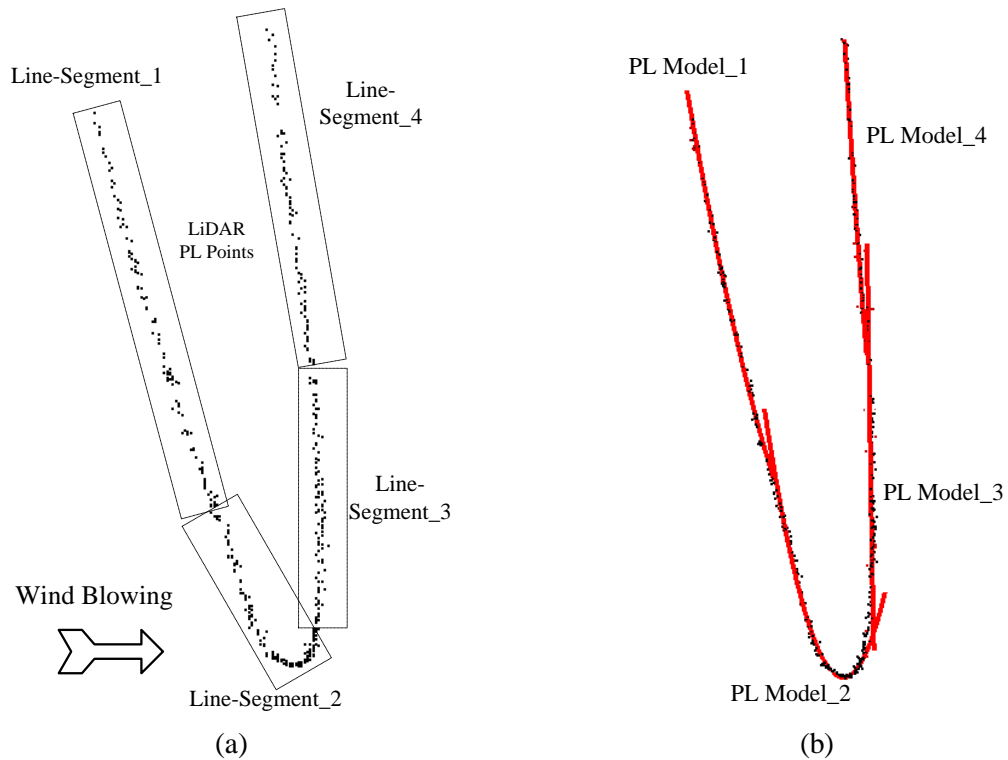
Figure 5.4: PL models with over-modeling errors due to wind blowing effect: (a) highly irregular distribution of PL points and (b) four PL model segments representing a PL.

Second, in the aforementioned error types, over-modeling errors occur only due to large data gaps, resulting in the generation of redundant line segments along a PL. In addition to the large

data gaps, the wind blowing effect also become a primary error source that mainly causes over-modeling errors due to the noisy distribution of PL points along PLs swinging from side to side as shown in Figure 5.4. Under the assumption that PLs are modeled using a linear basis function such as Eq. (4.1) in Chapter 4, even without large data gaps in Figure 5.4, it is hard to avoid the over-modeling error due to the wind blowing effect.

Third, the use of PL points corrupted by wind loading also affects the performance of the proposed post-processing method using the aforementioned MDL criterion function. The proposed method will be discussed in detail later. In order to correct over-modeling errors, the associated PL model segments should be hypothesized as a single PL model and thus the hypothesis (single model) is accepted in the MDL framework based on Eq. (5.3). However, due to the wind blowing effect, irregularity of PL point distribution accelerates, which causes large deviation between the hypothesized model and its PL points. As a result, the term of model closeness highly dominates over the MDL function and then the desired hypothesis might be rejected, thereby selecting PL models with over-modeling errors as an optimal model configuration.

We have discussed with difficulties in modeling PL objects, which are mainly caused by wind blowing effects. To overcome the difficulties, an approach, a wind adaptive parameter estimation, is proposed, which is discussed in detail in the next section.

5.3.1.3 Wind adaptive parameter estimation

In general, standard deviation σ used in Ω of the term of model closeness in Eq. (5.1) can be derived by measuring the deviation between an estimator and its observations, and expresses the precision of a set of observations. In a stationary case, σ is predictable by considering observation errors as white noise and can be used as *a priori* knowledge in the modeling process of objects

such as buildings. However, in the case of PLs as a dynamic object, LiDAR measurements are corrupted by random errors as well as external forces with various quantities such as wind loads, so σ becomes unpredictable. This means that it is difficult to determine σ in the range of deterministic approximation values. In this study, σ is called as a *noise scale factor*. To approximate σ as a predictable variable, the use of relationship between PL modeling accuracy and wind speed, "σ-wind speed", as shown in Figure 5.3 becomes an effective way. However, as mentioned in the previous sections, the information of wind speed is not always available and its accuracy is not reliable. Therefore, we propose an alternative method for measuring the wind blowing effects instead of using the information of wind speed, which is discussed as follows:

Measuring the magnitude of data noise for PL points

The effects of wind blowing to PLs can be approximated by measuring the degree of noisy distribution of PL points. This is because the more wind blows the more PL points are corrupted by the wind blowing effect. Suppose that PLs laid in a span are distributed with similar directions each other and are modeled based on the PMG method proposed in Chpater 4. Where, the PL models are generated with the high goodness-of-fit to the corresponding PL points. If PL points are corrupted by wind blowing, their PL models are also oriented with various quantities. The variation of PL orientations can be measured by the well-known root-mean-square error (RMSE) and thus reflects the wind blowing effect. Let $\{\theta_i : i = 1, ..., m\}$ denote the observed orientations of PL models and $\bar{\theta}$ indicates heir mean value. The RMSE of orientations of PL models $\Delta\theta$ is:

$$\text{RMSE}(\theta) = \Delta\theta = \sqrt{\frac{\sum_{i=1}^{m}(\theta_i - \bar{\theta})}{m}} \qquad (5.4)$$

Establishing relation of σ-Δθ

This step aims to establish a relation between noise scale factor and RMSE of orientations of PL models, "σ-Δθ" instead of "*σ*-wind speed". Our ultimate goal is to achieve the completeness of PL models by correcting PL modeling errors. This means that the number *n* of PL models reconstructed is equal to the real count of PLs *N*. Where, the ratio *R=n/N* becomes one. The ratio with more than one thus indicates the occurrence of over-PL modeling errors, while the ratio with less than one means the occurrence of under-PL modeling errors. This indicates that the corrected PL models should satisfy the condition, *R*=1, and the used noise scale factor becomes an optimal value $\hat{\sigma}$ under the current ambient situation (wind blowing) with a certain Δθ. As a result, the relation of $\hat{\sigma}$-Δθ can be developed from the relation of σ-Δθ. In the terms of correcting PL modeling errors, the use of $\hat{\sigma}$ approximated by the relation of $\hat{\sigma}$-Δθ leads to correct PL modeling errors with the condition, *R*=1. To determine the optimal noise scale factor $\hat{\sigma}$, there are essential processing steps proposed as follows:

- Generate PL models using the PMG method proposed in Chapter 4.

- Calculate RMSE of orientations of PL models Δθ for a span.

- Perform the rectification of PL models, which is discussed later, according to discrete values of σ differentiated by $\Delta\sigma$ (10cm).

- Examine the ratio having one (R=1) and find its associated values of σ which become optimal values of noise scale factor $\hat{\sigma}$.

In the given Δθ of each span as shown in Figure 5.5, plots are uniform over the optimal values of noise scale factor, $\hat{\sigma}$, by satisfying that *R*=1. Where, the range including the optimal values denoted as a gray block. As the RMSE of PL orientations Δθ increases from low (0.014°) to high

(0.25°) degree, the plots exhibit wild oscillations and the resulting range of $\hat{\sigma}$ narrows. We can expect that finding optimal noise scale factor is to be severely restricted by the high wind blowing effect.
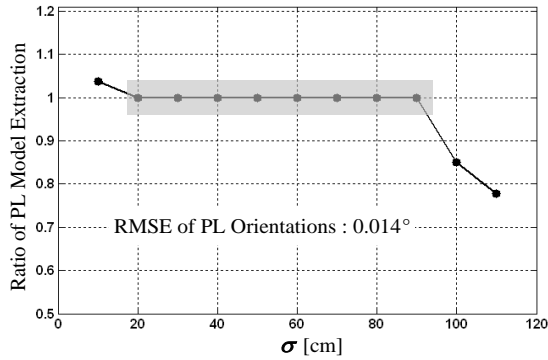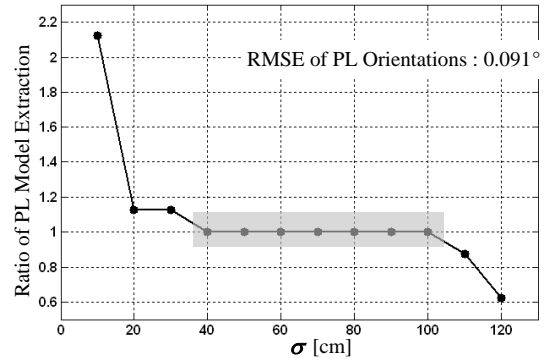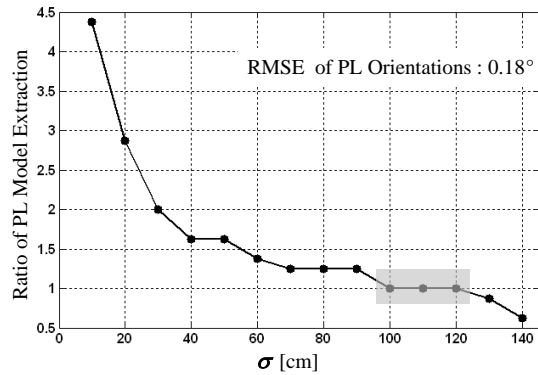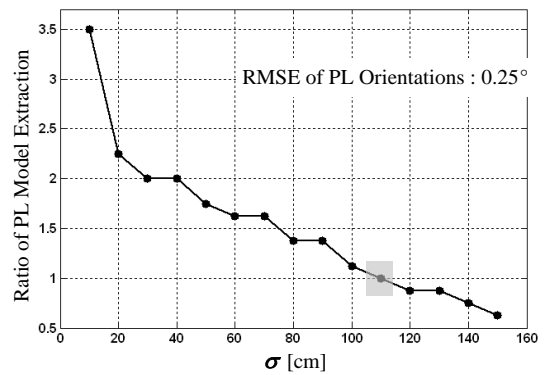
Figure 5.5: Plot of a relation between noise scale factor (σ) and ratio of complete PL modeling according to RMSE of PL model orientations: (a) 0.014°, (b) 0.091°, (c) 0.18°, and (d) 0.25°. The gray blocks denote the range of optimal noise scale factor having one in the ratio between the number of PL models extracted and the number of reference PLs.

Prediction of optimal noise scale factor

For the newly observed data, the value of $\hat{\sigma}$ is required to be predicted based on the relation of $\hat{\sigma}$-$\Delta\theta$. For this, the functional relation of $\hat{\sigma}$-$\Delta\theta$ should be formulated. We adopt a regression analysis which is usually used for analyzing and modeling a relationship between associated variables (Sen and Srivastava, 1990). In this study, 20 spans from two corridors were selected with respect to the degree of variations of PL orientation and used to estimate parameters of regression model. Figure 5.6 shows the plot of the regression model which is a function of $\hat{\sigma}$ conditioned on $\Delta\theta$. Where, a vertical bar denotes the range of optimal noise scale factor $\hat{\sigma}$ at each span and its mean value $\bar{\sigma}$ is expressed as a solid point. Using $\bar{\sigma}$s and $\Delta\theta$s derived from 20 spans, the regression model is developed as a linear in the following form:

$$Y(\bar{\sigma}) = f(\Delta\theta, \beta) = a\Delta\theta + b, \qquad \beta = \{a, b\} \tag{5.5}$$

Where, β denotes unknown coefficients which consists of a slope *a* and an intercept *b* which are estimated as 142.0 and 0.5599, respectively. The R-squared (R^2) of the regression model, which indicates how well data fit the corresponding model with the range 0 to 1, is calculated as 0.9838. This means that the model fits the data adequately. In Figure 5.6, the linear prediction values of $\hat{\sigma}$ calculated by the regression model fall within the range of optimal noise scale factor (vertical bars) only up to approximately $0.2°$ of $\Delta\theta$. This is due to the large fluctuations of $\bar{\sigma}$ by suddenly going up and down more than $0.2°$ of $\Delta\theta$. As a result, the good prediction of optimal noise scale factor for a new data set which is acquired under the strong wind blowing might be difficult even though the regression model is formulated by more complex models with many parameters (high order non-linear fitting).
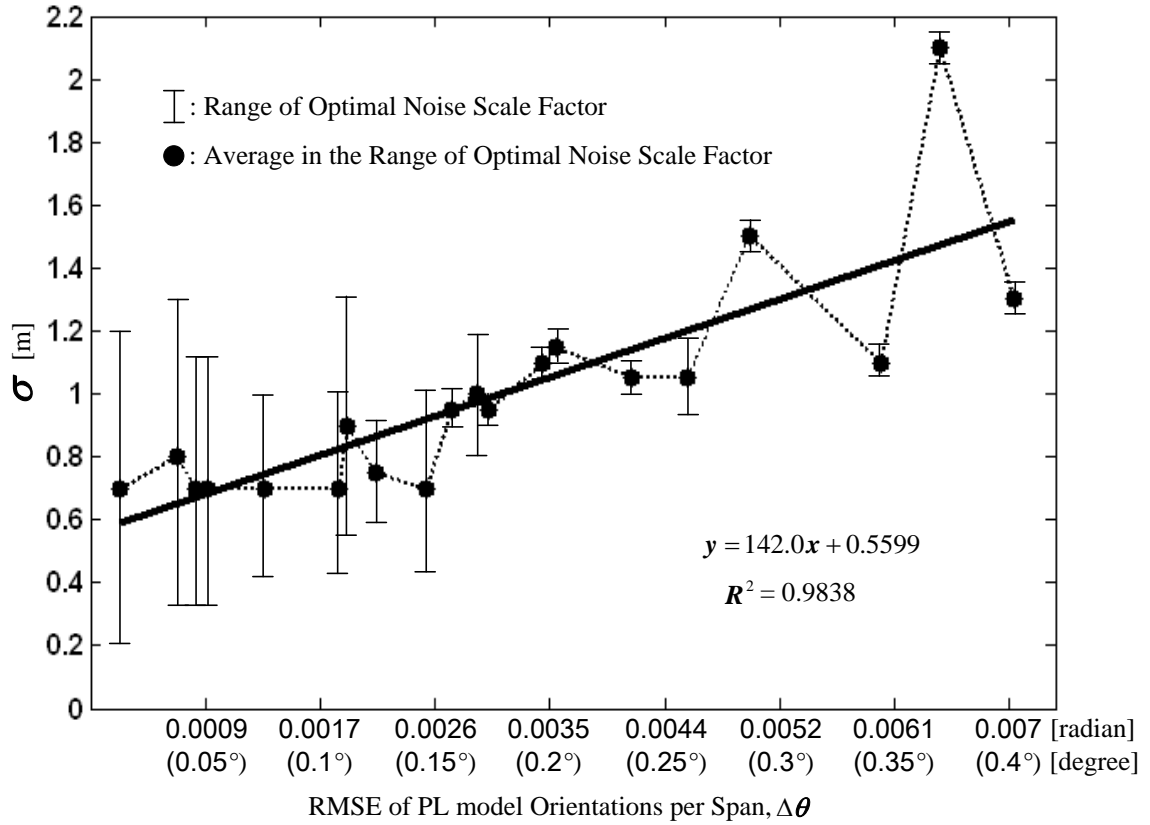
Figure 5.6: Plot of the relation between noise scale factor σ and RMSE of orientations of PL models $\Delta\theta$. The vertical bar denotes the optimal range of σ at each RMSE. The relation is modeled as a linear function and denoted as a solid line.

5.3.1.4 Model split process

Using prior knowledge on the noise scale factor, the split process is performed by dividing over-simplified PL models into single PL models, thereby correcting under-modeling errors. For this, some successive processing steps are proposed.

First, a segmentation process is required for the spatial re-grouping of PL points. This is because there is no *a priori* information about how many PL models *Ms* are needed for rectifying over-simplified PL models. The PL points grouped are thus used as seed segments for detecting

individual PL models. In this study, the region growing approach is considered as an effective method in grouping PL points using closeness property in spatial point distribution. This is due to the fact that PL points belonging to a PL model are closely distributed each other and mostly isolated from other objects. The region growing is performed by measuring a 3D Euclidean distance between points. If the distance is less than the pre-specified tolerance ζ, the associated points are labelled as the same group. In here, the value of distance threshold is determined as about 20 cm by considering the normal positional accuracy of airborne LiDAR points in PL corridor mapping. As a result, the region growing process continues until all points are assigned to the corresponding segments $\{s_1, ..., s_m\}$.

Second, the process of combining potential segments that represent the same PL is required to generate the corresponding PL model M without under-modeling errors. It is performed based on the hypothesis generation and verification process. The first step is that hypothetical PL models $\mathcal{H}$s are generated using pairs of segments. Then, for each hypothesis $\mathcal{H}$, the degree of line significance is measured by counting the number of segments that lie spatially close to the corresponding $\mathcal{H}$ within ζ. As a result, a $\mathcal{H}$ with the highest degree of line significance is firstly selected and its associated segments are labelled. Similarly, additional hypotheses $\{\mathcal{H}\}$ are subsequently generated using un-labelled segments. This process finally produces a set of n hypotheses, $\{\mathcal{H}_1, ..., \mathcal{H}_n\}$.

Third, so far we have been careful to make redundant hypotheses $\{\mathcal{H}\}$ to extend the opportunity of finding an optimal configuration of PL models $\mathcal{H}^*$ for the correction of under-modeling errors. The verification process of $\{\mathcal{H}\}$ is performed by evaluating the acceptance of one of two possible sets, null $\mathcal{H}_0$ and alternative $\mathcal{H}_a$, in the MDL framework. In here, the $\mathcal{H}_0$ becomes a PL model M before the split process as shown in Eq. (5.6). The $\mathcal{H}_a$ denotes a new

configuration of PL models, that is, given $\{\mathcal{H}_{j=1,...,n}\}$, $\mathcal{H}_a$ are created by the combination of $\{\mathcal{H}\}$ as illustrated as Eq. (5.7).

$$\mathcal{H}_0 = \{M\} \tag{5.6}$$

$$\{\mathcal{H}_a\} = \{\{\mathcal{H}_1, \mathcal{H}_2\}, \{\mathcal{H}_1, \mathcal{H}_2, \mathcal{H}_3\}, ..., \{\mathcal{H}_1, ..., \mathcal{H}_j, ..., \mathcal{H}_n\}\} \tag{5.7}$$

Note that the order of indices of $\mathcal{H}_j$ follows the degree of line significance. We are now interested in making a decision for which of $\{\mathcal{H}_a\}$ is to be the best configuration and whether it can be replaced with $\mathcal{H}_0$ or not. The decision is carried out in the aforementioned MDL framework. Therefore, under the assumption that $\mathcal{H}_0$ is an optimal representation of the current PL points $\mathcal{H}^*$, its rejection process is performed if the DL value of $\mathcal{H}_0$ is larger than one of $\{\mathcal{H}_a\}$, which is defined by

$$\mathcal{H}^* = \arg\min \{DL(\mathcal{H}_0), DL(\mathcal{H}_a)\} \tag{5.8}$$

Consequently, PL models with under-modeling errors are corrected by selecting the alternative hypothesis, that is one of $\{\mathcal{H}_a\}$. In the next section, over-modeling errors are corrected through the merge process which is described in detail.

5.3.1.5 Model merge process

To correct the over-modeling errors, redundant PL models should be merged into the neighbour PL models. For this, similar to the split process, the hypothesis verification of PL models is performed based on the aforementioned MDL criterion. Given a set of PL models $Ms = \{M_1, ..., M_k\}$, a null hypothesis $\mathcal{H}_0$ is formed by selecting two models from Ms, while its

alternative hypothesis $\mathcal{H}_a$ becomes a newly generated hypothetical PL model by merging the two models, which take the following forms

$$\mathcal{H}_0 = \{M_i, M_j | 1 \leq i, j \leq k \quad i \neq j\} \tag{5.9}$$

$$\mathcal{H}_a = \{M_{ij} | 1 \leq i, j \leq k \quad i \neq j\} \tag{5.10}$$

If the DL value of $\mathcal{H}_a$ is less than one of $\mathcal{H}_0$, the $\mathcal{H}_a$ is accepted as an optimal hypothesis $\mathcal{H}^*$, so that the over-modeling errors are corrected. This process is continued until $\mathcal{H}_a$ is selected as $\mathcal{H}^*$ over the all PL models Ms.

In Figure 5.7, we show a simple example of correcting under- and over-modeling errors through the proposed split and merge process using a real data set. As we can see, $\mathcal{H}_0 = \{M\}$ in Figure 5.7(a) shows rather poor fitting it to the PL points, which causes the under- modeling errors. On the other hand, $\mathcal{H}_0 = \{M_1, M_2, M_3\}$ in Figure 5.7(c) is generated by fitting well them to local segments of PL points, which causes the over-modeling errors. For the correction of the errors, the split or merge technique is applied to the $\mathcal{H}_0$ by separating or combining its PL models. This leads to produce alternative hypotheses $\mathcal{H}_a = \{\mathcal{H}_1, \mathcal{H}_2\}$ and $\mathcal{H}_a = \{M_{123}\}$ illustrated in Figure 5.7(b) and (d), respectively. In addition, each term of MDL function is evaluated in Table 5.1. As the $\mathcal{H}_a$s minimize the total cost of MDL function $\mathcal{L}_{tot}$, the $\mathcal{H}_0$s are converted to the corresponding $\mathcal{H}_a$s, so that the under- and over-modeling errors are corrected. Where, RMSE of PL orientations is observed as $0.092°$ for the split process and $0.51°$ for the merge process. Based on the regression model of Figure 5.6 and RMSEs, optimal values of noise scale factors are predicted as 0.74 m and 2.25 m, respectively.
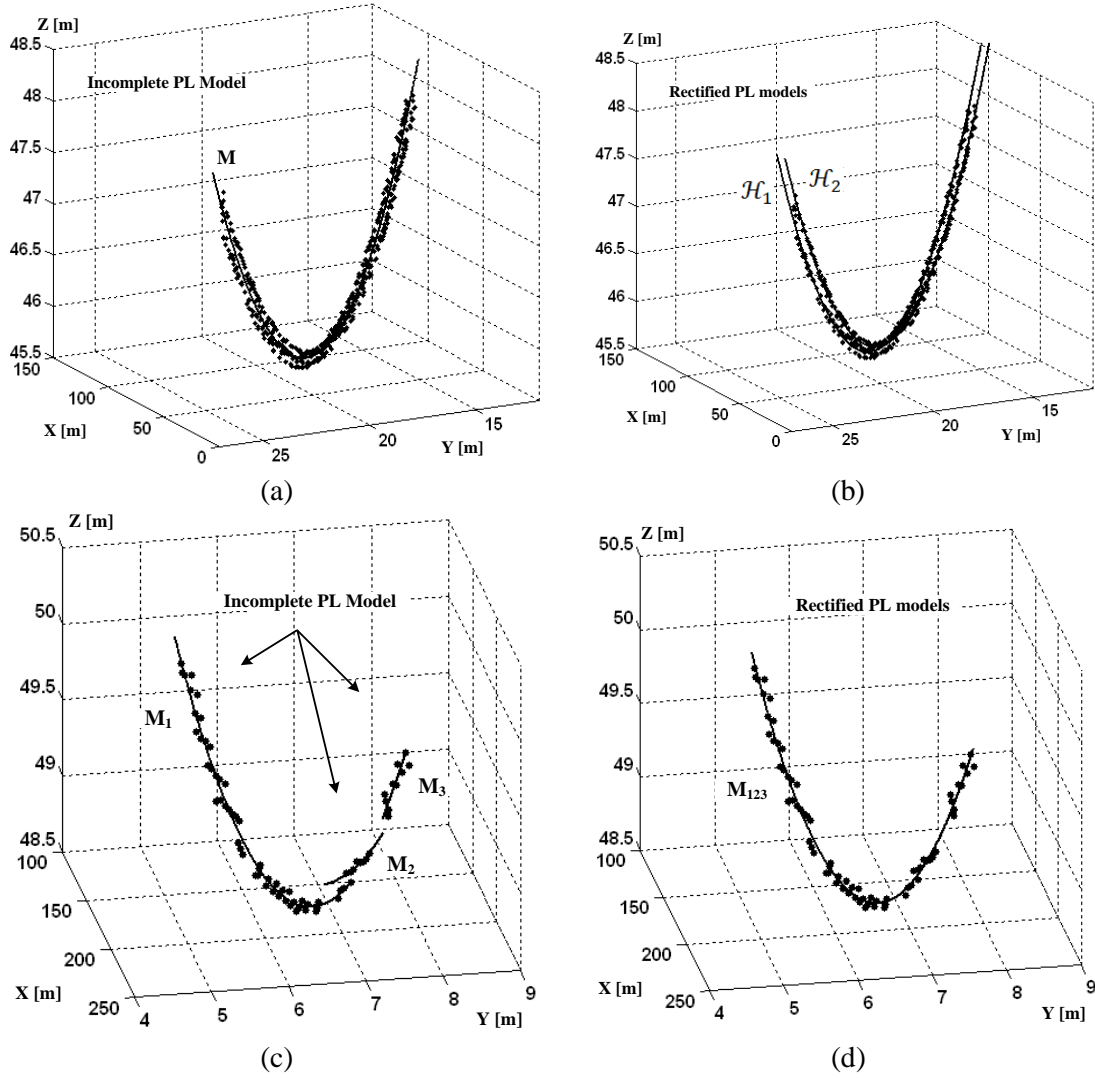
Figure 5.7: PL model correction through split ((a) and (b)) and merge ((c) and (d)) process; (a) and (c) mean $\mathcal{H}_0$ with the under- and over-modeling errors; (b) and (d) indicate $\mathcal{H}_a = \mathcal{H}^*$.

Table 5.1: MDL terms: total description length ($\mathcal{L}_{tot}$), model closeness ($\mathcal{L}(D|H)$), and model complexity term ($\mathcal{L}(H)$).

Step	#Line	$\mathcal{L}_{tot}$	$\mathcal{L}(D|H)$	$\mathcal{L}(H)$
Split	M	98.33	70.61	27.72
	$\mathcal{H}_1 + \mathcal{H}_2$	67.71	12.33	55.38
Merge	$M_1 + M_2 + M_3$	48.08	0.067	48.01
	M_{123}	24.15	0.081	24.07

5.3.2 Across PL span analysis

The main aim of our approach in this section is to correct partial-modeling errors by fining start and end positions of PLs across PL spans. This is mostly related to the process of POA detection. If POAs are determined, the correction of partial-modeling errors can be readily achieved by extending PL models to the corresponding POAs. However, detecting the POAs is a very complex problem because geometric information such as size and position of insulators as well as pylons is important to be known. To avoid the difficulties, in this study, two heuristic methods for the determination of POAs are proposed: (1) PL connectivity analysis and (2) pylon region of interest detection. This issue is discussed in more detail in the next sections.

5.3.2.1 Mathematical formulation for POA detection

In general, points intersecting PL models that are successively linked across spans become POAs, which are equivalent to the CAP in the suspension insulator type and the IAP in the dead-end insulator type. In this study, we only consider such POAs for the rectification of PL models. It assumes that two PL models Ms = {M_i, M_j} are in the conjugate pair relation if they are successively linked across span. Their intersection $w = \{X, Y, Z\}$ can be estimated based on a weighted least squares adjustment. Note that a PL model M is formed by the combination of a line (Equation 4.1) $L(\theta, \rho)$ and catenary curve (Equation 4.2) $C(a, b, c)$ in 3D space. Given the model parameters $\{\theta, \rho, a, b, c\}$ and their variances (i.e., σ_θ^2, σ_ρ^2, σ_a^2, σ_b^2, σ_c^2) which are evaluated as weights (i.e., P_{Li}, P_{Lj}, P_{Ci}, P_{Cj}), the conjugate paired two PL models can provide four observation equations from Eq. (5.12) to (5.15). After replacing the nonlinear equations with their linearized forms, w is to be estimated based on the form of a Gauss-Markov linear model (see, Eq. 4.7).

$$L_i(X,Y) = X\cos\theta_i + Y\cos\theta_i - \rho_i = e \qquad e\sim N\left(0, \sigma_0^2 P_{Li}^{-1}\right) \tag{5.11}$$

$$L_j(X,Y) = X\cos\theta_j + Y\cos\theta_j - \rho_j = e \qquad e\sim N\left(0, \sigma_0^2 P_{Lj}^{-1}\right) \tag{5.12}$$

$$C_i(X,Z) = a_i + c_i\cosh\left(\frac{X-b_i}{c_i}\right) - Z = e \qquad e\sim N\left(0, \sigma_0^2 P_{Ci}^{-1}\right) \tag{5.13}$$

$$C_j(X,Z) = a_j + c_j\cosh\left(\frac{X-b_j}{c_j}\right) - Z = e \qquad e\sim N\left(0, \sigma_0^2 P_{Cj}^{-1}\right) \tag{5.14}$$

5.3.2.2 PL connectivity analysis

To define optimal conjugate pairs of PL models from successively connected spans, connectivity of PL models across spans is required to be examined. The basic idea for this is to estimate possible POAs from hypothetic pairs of PL models and choose a POA with minimum positional error among them. However, the use of the simple statistical selection criterion sometimes causes the establishment of wrong conjugate pairs of PL models due to the complexity of PL network configuration. Where, a PL network is normally designed with multiple layered lines with the same orientation in which PLs are overlapped in the vertical domain (i.e., X-Y plane). From our heuristic observations, the undesired POAs are mostly isolated as positioned away from pylon structures. Therefore, the limitation can be easily solved by adding a geometric constraint to the selection criterion. The constraint is that all POAs should be placed near to a pylon structure. After creating a local search region *V* at a POA with minimum positional error, the existence of unlabelled points which might represent pylon structures is examined. If the point density *PD* of unlabelled points is equal to zero, the POA becomes an undesirable intersection point. As shown in Figure 5.8, let $\{M_{j=1,\ldots,m}\}$ denotes a set of *m* different PL models in the neighbour span. A PL model M_i in the current span generates its associated candidate POAs, $\left\{POA_{j=1,\ldots,m}^{ij}\right\}$ having point density of more than zero, *PD*(POAs) > 0, and the corresponding

accuracy $\left\{\sigma_{j=1,\dots,m}^{ij}\right\}$. One of the candidates is finally selected as an optimal POA, POA_i^* under the condition that it has a minimum position error and its *PD* is more than zero, which is defined by

$$POA_i^* = \arg\min_{\forall\{POA\}}\left\{\sigma_{j=1,\dots,m}^{ij}\right\}_{j=1}^m \tag{5.15}$$

In the real world, PLs are attached to the corresponding POAs without any geometrical deviation. However, it is impossible to avoid the deviation between PLs and their POAs when POAs are estimated by PL models which are derived from noisy data. To correct the deviation, the parameters of PL models are re-estimated by passing the corresponding POAs. Note that the accuracy of POAs varies according to the qualities of PL models used. This is why, it is required to first fix the POA with the high positional accuracy and then sequentially perform the adjustment of PL models over the whole PL network. As a result, this leads to improve the quality of PL models with low modeling accuracy.
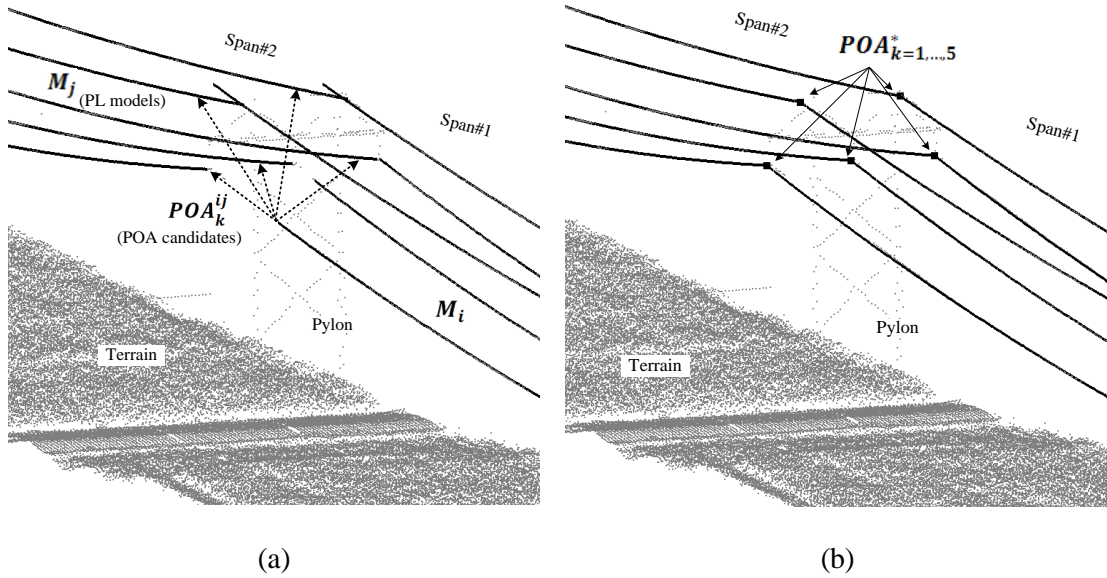
Figure 5.8: PL model rectification based on the PL connectivity analysis across spans: (a) determination of PL conjugate pairs and (b) optimal POA detection and PL model correction.

5.3.2.3 Pylon region of interest detection

As mentioned above, POAs are generated by using conjugate pairs of PL models. However, the relation of conjugate pairs is not always available due to the inequality in terms of the number of PL models between subsequently linked spans. The inequality is mainly due to two causes: original configuration of PLs and PL modeling errors (i.e., un-detection errors). In order to detect POAs for PL models with non-conjugate pairs, the use of pylon region can be useful to approximate the corresponding POAs. The POAs are detected by intersecting PL models with the pylon region detected.

As a pylon is also isolated objects like PLs, a region growing process becomes a suitable method for detecting the pylon region. Note that a seed position for growing the region would be one of POAs extracted. Once the pylon region is detected, its orientation is required to be known for computing accurate POAs. It is due to the fact that POAs are usually placed along the line

vector with pylon's orientation which passes through the center of pylon in X-Y plane. Two simple methods are applicable to compute the pylon's orientation; the use of (a) existing POAs and (b) direction of PL models. First, if more than two POAs are already detected, parameters of line vectors are easily calculated and the pylon's orientation is determined. Note that the distribution of POAs should be wide enough to the horizontal domain to avoid singular in the matrix computation. To check the feasibility, the geometric precision with respect to the orientation parameter can be used. That is, if the distribution of POAs is enough to be widen along the orientation of pylon, the good precision of the parameter σ_θ (smaller value) is observed. In the matrix form, it can be derived from the covariance matrix $D(\hat{\xi}) = \sigma_0^2(A^T A)^{-1} = \sigma_0^2 Q$ of the best estimation $\hat{\xi} = \{\theta, \rho\}$ which is related to the parameters of the line equation in the X-Y plane. Where, the elements of the cofactor matrix Q are comprised of $\begin{bmatrix} q_{\theta\theta} & q_{\theta\rho} \\ q_{\theta\rho} & q_{\rho\rho} \end{bmatrix}$, resulting in $\sigma_\theta = \sqrt{q_{\theta\theta}}$. The threshold of σ_θ, in this study, is simulated based on a 0.5-meter displacement between POAs in X-Y plane. Second, as two orientation vectors, PL and its pylon direction, are normally orthogonal, the mean value of orientations of PL models can be used to calculate the corresponding orientation of pylon

After obtaining the proper orientation of pylons using one of two methods, a hyperplane with the orientation is generated at the center of pylon region. New POAs for the non-conjugate pair PL models are finally determined by intersecting the PL models with the hyperplane. Figure 5.9 depicts the whole process for the detection of pylon region and the approximation of POAs.
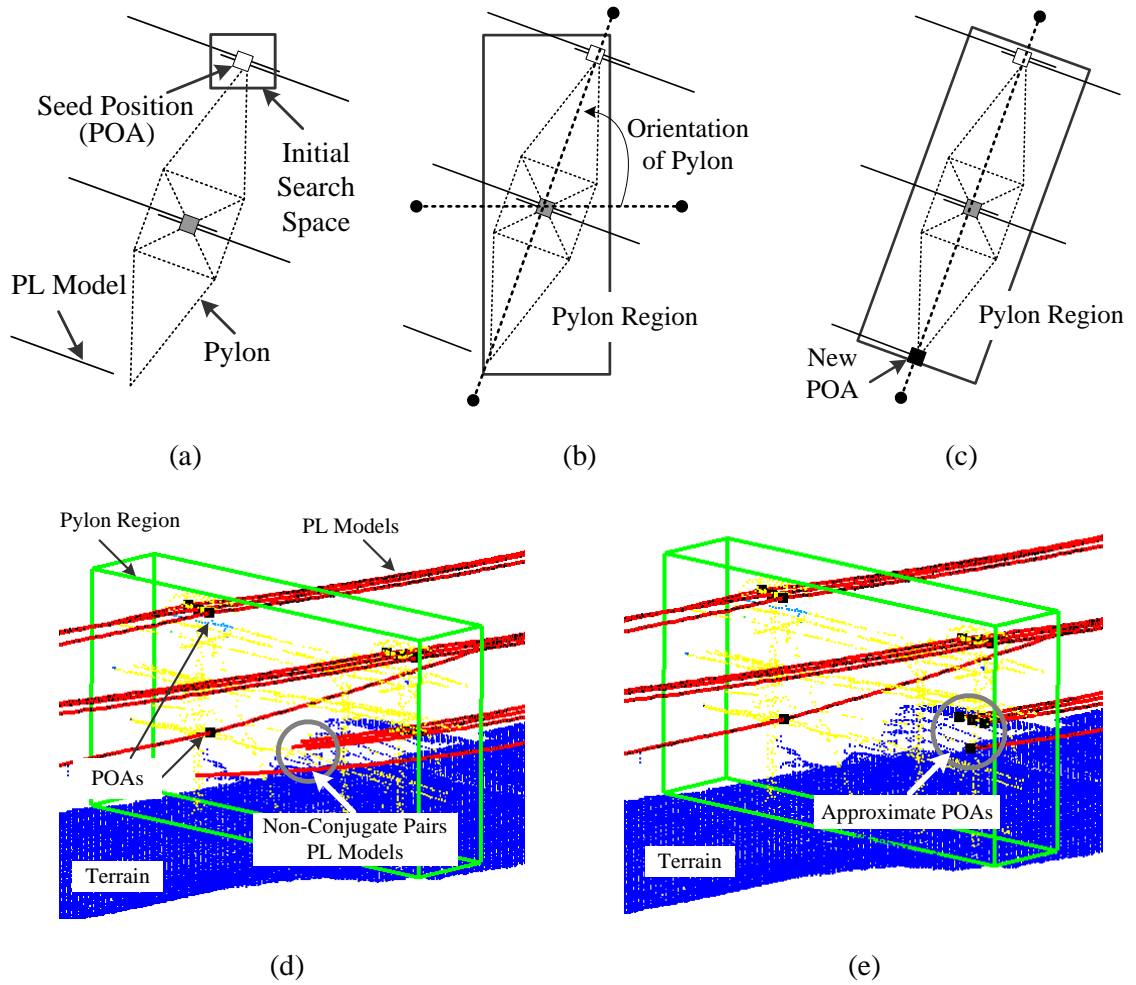
Figure 5.9: Illustration of POA detection using the pylon region: (a) region growing process, (b) determination of pylon orientation using POAs detected, (c) extraction of new POA and rectification of PL model with a partial-modeling error, (d) before and (e) after the rectification of PL models in the real data.

5.4 Experimental results

5.4.1 Folsom data

To evaluate the performance of the proposed approach, PL modeling results containing modeling errors which are generated in the previous chapter are used. As shown in Table 5.2(a), prior to the process of PL model rectification, 145 PL models out of total 151 PLs belonging to 9 spans were completely reconstructed which corresponds to a 96% success rate. In contrast, the aforementioned PL scene complexity caused 4% of the modeling errors which consist of partial modeling (1.3%), over modeling (2%), and un-detection (0.7%). Where the partial and over modeling errors were due to the large data gap (i.e., ~10 meters) and un-detection was caused by a vegetation encroachment. As evaluated in Table 5.2(b), except for un-detected PL models, the proposed approach corrects the incompletion of PL models, resulting in the 99.3% success rate of complete PL modeling. Additionally, we counted 125 POAs in the data set as depicted in table Table 5.3. In the across span analysis, the PL connectivity analysis achieves 90.4% POA detection rate and then the result is improved up to 98.4% using the pylon region of interest. Consequently, the POAs detected improves the quality of PL models by precisely determining their start and end positions. This results in the adjustment of total length of PL models from 19361.6 m to 17711.3 m, which corresponds to an 8.52% reduction rate. Figure 5.10 illustrates the final 3D view of the PL components including PLs, POAs, and pylons in the PL corridor network.
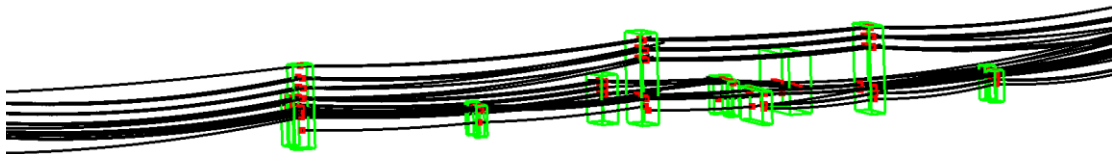
Figure 5.10: 3D PL network modeling containing 3D PL models (black color), POAs (red color), and pylon models (green color).

Table 5.2: Results of the 3D PL model reconstruction (a) before and (b) after the rectification of incomplete PL models

(a) PL model reconstruction

	Total	*Complete Modeling*	*Partial Modeling*	*Under Modeling*	*Over Modeling*	*Un-Detection*
Number	151	145	2	0	3	1
Rate (%)	100	96	1.3	0	2.0	0.7
(b) PL model rectification						
Number	151	150	0	0	0	1
Rate (%)	100	99.3	0	0	0	0.7

Table 5.3: POA detection rate before and after pylon modeling.

	Total	*Before Pylon detection*		*After Pylon detection*		
		Detection	*Un-Detection*	*Detection*	*Un-Detection*	*Wrong-Detection*
Number	125	113	12	123	0	2
Rate (%)	100	90.4	9.6	98.4	0	1.6

In Table 5.3, even if the detection rate of POAs increases by 8% using the pylon region, redundant POAs which corresponds to 1.6% wrong-detection are generated. The main two reasons are illustrated in Figure 5.10. First, in Figure 5.11(a), when more than two PLs converge to a POA, one of them is only involved to the relationship of conjugate pair. This leads to redundantly detect POAs for other PL models using the corresponding pylon region. Second, as shown in Figure 5.11(b), due to the un-detection of a PL model, a POA is wrongly generated by attaching the PL model to the different pylon.

(a)   (b)
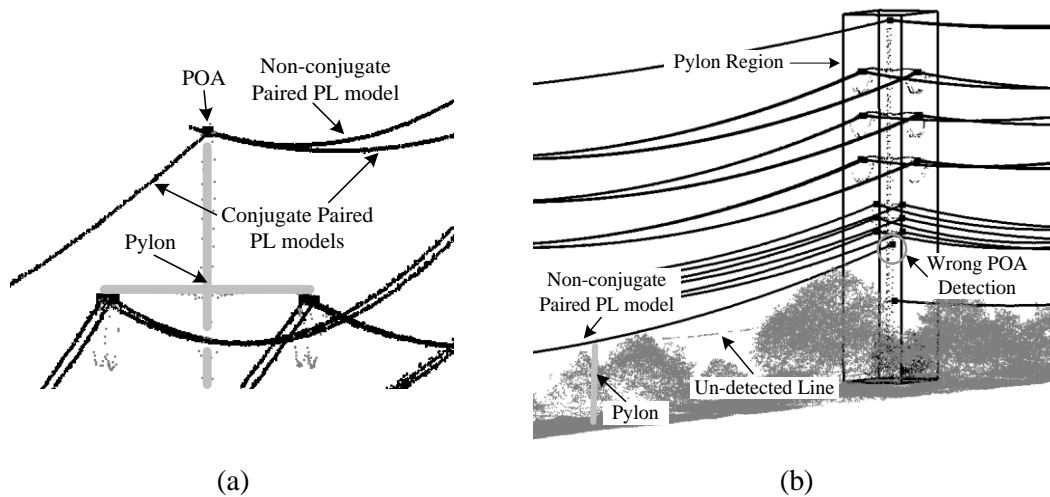
Figure 5.11: Examples of the limitations in detecting POAs due to non-conjugate paired PL models even in the use of pylon region.

5.4.2 GDI inventory data

For the practical use of the proposed method, it is an important to test its performance using long PL corridor data sets. We obtained a set of inventory data from a utility firm, GeoDigitial International Inc (GDI), which comprises four different PL corridor areas named as DB302, 20023, 20130 and 24051. Figure 5.12 shows configurations of total corridor areas in X-Y plane, which is coloured from dark blue to dark red with respect to height. Each corridor area contains its major pylon type supporting the corresponding electrical power voltage, that is, steel pole type supporting 138 kV for DB302, H-frame type supporting 161 kV for 20023, and four-legged rigid type supporting 345 kV for 20130 and 24051. The detailed data specification is summarized in Table 5.4. The data was acquired by Riegl's LMS Q560 laser scanner over about 138.5 km corridor area in April and May 2011. Due to four to five multiple returns from a single pulse, a high average point density with more than 16 pts/m^2 is obtained. However, points representing

PLs are sparsely distributed with about 2 pts/m^2 average point density which is equal to 0.7 m average point distance on PLs. This is due to the fact that a PL is a thin object with the thickness of degree of several centimetres, so the probability of hitting a laser pulse to PLs lower than other large objects such as building and tree. In addition, the thickness of PLs increases according to voltage capacity. For example PLs for 345 kV are about 1.5 times thicker than ones for 138 kV in a pipe-type conductor (Shoemaker and Mack, 2007). This leads that the average point distance on PLs slightly decreases from 0.71 m to 0.58 m which shows a proportion of about 1.2.

Table 5.4: Basic data specifications

Corridor	Acquisition Date [M/D/Y]	Voltage Type [kV]	Length [km]	Bundle Wires	Ave. Point Density [pts/m^2]	Ave. Point Distance per Conductor / Shield Wire [m]		
						Ave	Min	Max
BD302	5/17/2011	138	34.0	No	> 16	0.71 / 0.97	0.35 / 0.53	1.1 / 1.44
20023	4/21/2011	161	37.7	No	> 16	0.67 / 0.87	0.51 / 0.74	0.79 / 1.05
20130	4/21/2011	345	40.9	Yes	> 16	0.58 / 0.79	0.49 / 0.56	0.89 / 0.95
20145	4/16/2011	345	25.9	Yes	> 16	0.77 / 0.69	0.37 / 0.57	2.64 / 0.83
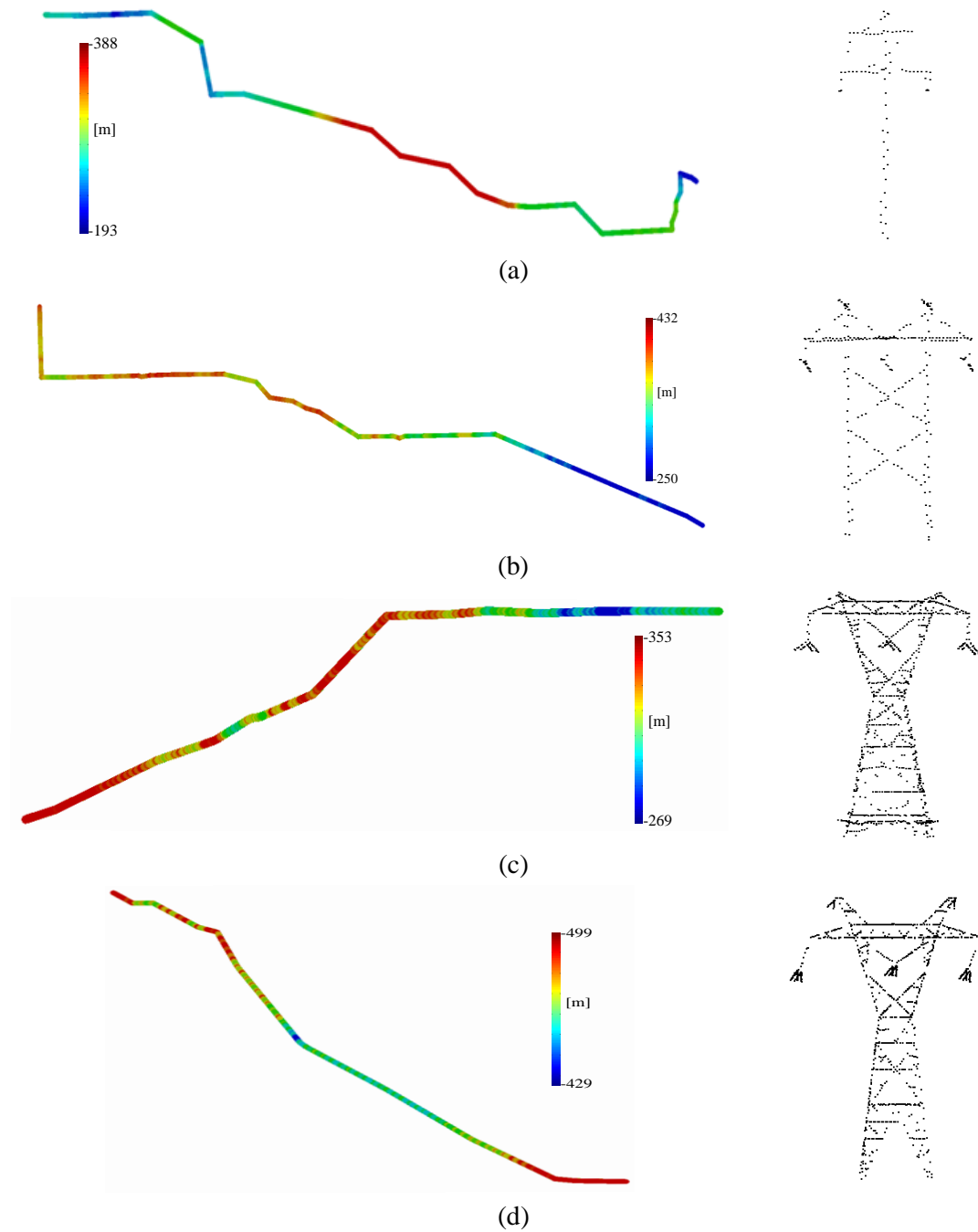
Figure 5.12: Test data sets of PL corridor area with different voltage types (left) and the corresponding pylon types (right): (a) 138 kV (DB302) and steel pole type (b) 161 kV and H-frame type (20023), (c) 345 kV and four-legged rigid type (20130), (d) 345 kV and four-legged rigid type (24051).
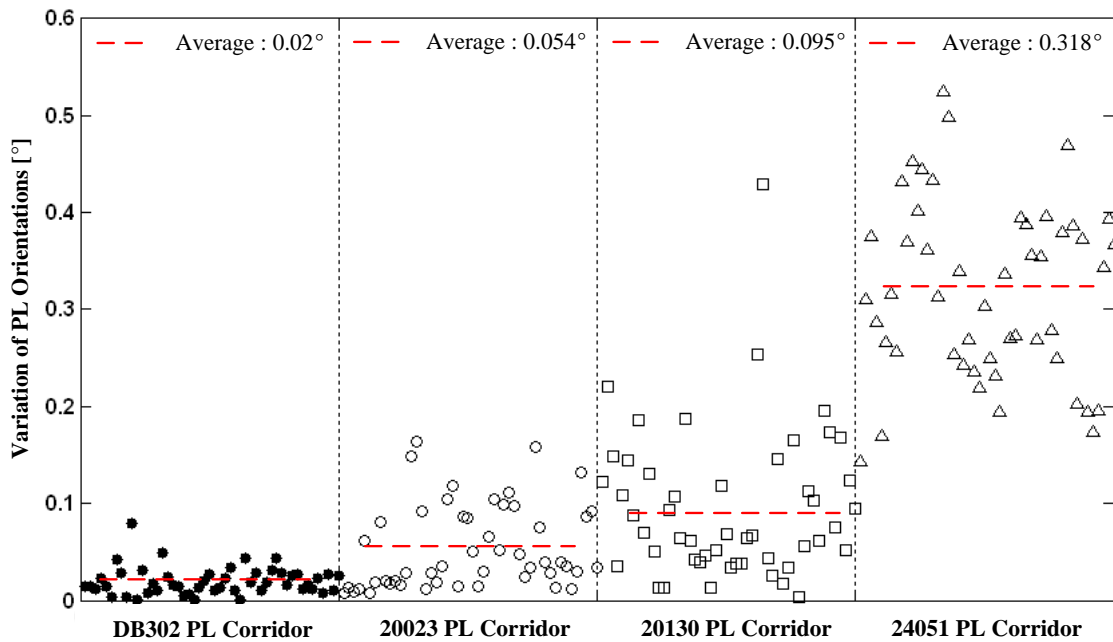
Figure 5.13: Scatter plot of variations of PL orientations for four PL corridor test areas.

To roughly know about how much the data is corrupted by external forces such as winds, variations of PL orientations are examined for the four PL corridor areas as shown in Figure 5.13. 50 spans are randomly selected from each of four corridor areas and then the corresponding RMS errors with respect to PL orientations per span are calculated. Suppose that there are no systematic errors and orthogonal laser beam arrays. The average variation of PL models in the BD302 shows very small of 0.02°. We can expect data to be collected almost without wind effects. Compared to the BD302, the next two corridors, 20023 and 20130, show that their RMS errors slightly increase and are scattered, resulting in the average of 0.054° and 0.095°. This means that the distribution of PL points is somewhat affected by winds. In the case of 24051 corridor area, the distribution of RMS errors shows large variations over the range from about 0.2° to 0.6°, resulting in the average of 0.318°. We surely make inferences that PL points are extremely corrupted by strong winds. Thus, the degradation of PL modeling accuracy is expected in the meter level from the Figure 5.3

and Figure 5.5. As a result, For the practical applications such as the PL risk management, the models are not appropriate to precisely assess clearance quantities derived from object (usually trees) encroachments.

5.4.2.1   BD302 PL corridor area

This corridor is comprised of 198 spans which correspond to the length of 34 km and contains the number of 594 conductors supporting 138 kV and 198 shield wires. Table 5.5 shows the results of PL modeling for conductors and shield wires before (Table 5.5(a)) and after (Table 5.5(b)) the PL model correction. Conductors are initially modeled with the complete modeling rate of 75.8%. Modeling errors which consist of 9.9% for partial modeling, 13.8% for over modeling, and 0.5% for un-detection also occur. The modeling errors are mostly subject to the low point density with a wide range of average point distance on PLs from 0.35 m to 1.1 m. Note that the PMG approach proposed in the previous chapter requires approximately 1 pts/m^2 point density for the estimation of PL model parameters. In the case of shield wires, the complete modeling rate is relatively low with 37.9% due to the wider point distance in range [0.53, 1.44] than the one of conductors. The reason is that the shield wires are thinner than conductors, so that the probability of hitting a laser pulse to PLs decreases. Large modeling errors thus happen with 22.7% for partial modeling, 9.6% for over modeling, and 29.8% for un-detection. After performing the PL model rectification, most of conductors and shield wires are completely generated, resulting in the success rate of 99.4% and 70.2 except for the un-detection rate of 0.6% and 29.8%, respectively. Figure 5.14 illustrates final result of the proposed approach for the BD302 PL corridor area. Each span is composed of three conductors and one shield wire and their PL models are continuously connected one another by the corresponding POAs.

Table 5.5: Results of the 3D PL model reconstruction (a) before and (b) after the rectification of incomplete PL models in the BD302 PL corridor area.

(a) PL model reconstruction

		Total	Complete Modeling	Partial Modeling	Under Modeling	Over Modeling	Un-Detection
Conductor	Number	594	450	59	0	82	3
	Rate (%)		75.8	9.9	0	13.8	0.5
Shield Wire	Number	198	75	45	0	19	59
	Rate (%)		37.9	22.7	0	9.6	29.8

(b) PL model rectification

		Total	Complete Modeling	Partial Modeling	Under Modeling	Over Modeling	Un-Detection
Conductor	Number	594	591	0	0	0	3
	Rate (%)		99.4	0	0	0	0.6
Shield Wire	Number	198	139	0	0	0	59
	Rate (%)		70.2	0	0	0	29.8

(a)

(b)
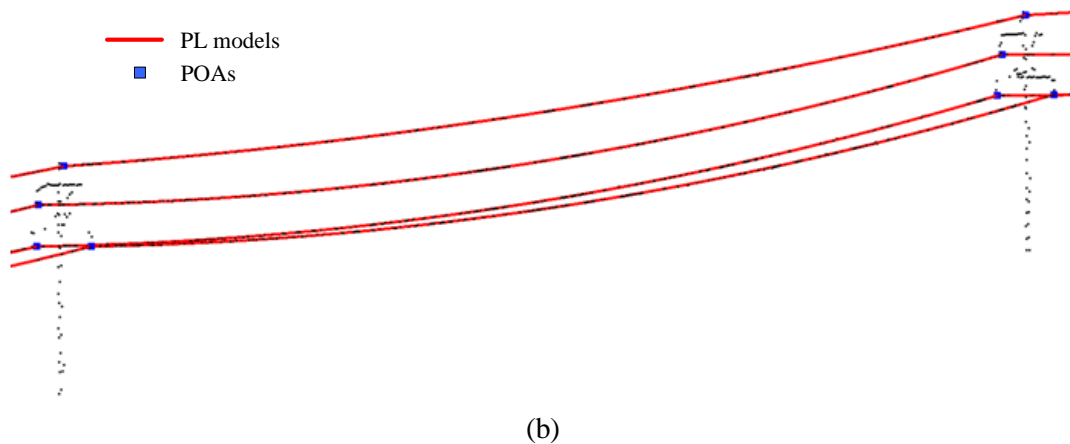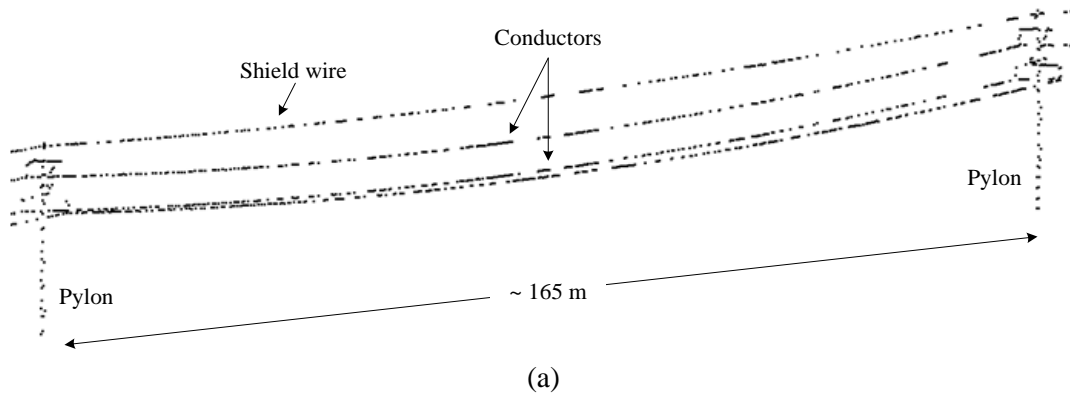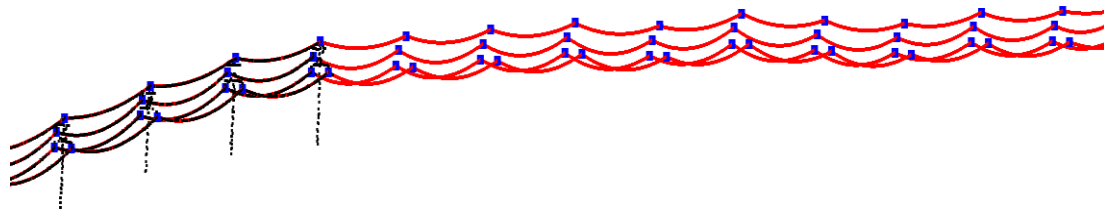
(c)

Figure 5.14: Examples of establishing PL model network in the BD302 corridor: (a) raw LiDAR data of PL structures within a span, (b) generation of PL models and POAs in a span, and (c) PL model network.

5.4.2.2   20023 PL corridor area

The 20023 corridor region consists of 157 spans which is equivalent to the length of 37.7 km. Each span contains three conductors supporting 161 kV and two shield wires and total line number is counted as 417 and 314, respectively. The modeling results are tabulated in Table 5.6 and depicted in Figure 5.15. Based on the PMG method, we first produce conductors with the complete modeling rate of 33.3% and the modeling errors of 66.6%. The proportion of errors can be divided into three types, 17.8% for partial modeling error, 47.6% for over modeling error, and 1.3% un-detection. Compared to the results of BD302 corridor, the modeling completion is poor even using PL points with relatively higher point density. We can infer the reason from the fact that the observed PL points are more corrupted with noise which arises from wind effects as well as random errors. This is supported by the change in the average variation of PL orientations from $0.02°$ in BD302 corridor to $0.054°$ in 20023 corridor. In the shield wires, only 14.6% of PL models are completely extracted. However, after carrying out PL model rectification, desired results are obtained by correcting partial and over-modeling errors, which accord with the complete modeling rate of 98.7% and 96.2% for conductors and shield wires. As the point density

of shield wires increases from 0.97 pts/m^2 in BD302 corridor to 0.87 pts/m^2 in BD302 corridor, the complete modeling rate highly increases from 70.2% to 96.2%.

Table 5.6: Results of the 3D PL model reconstruction (a) before and (b) after the rectification of incomplete PL models in the 20023 PL corridor area.

(a) PL model reconstruction		Total	Complete Modeling	Partial Modeling	Under Modeling	Over Modeling	Un-Detection
Conductor	Number	471	157	84	0	224	6
	Rate (%)		33.3	17.8	0	47.6	1.3
Shield Wire	Number	314	46	84	0	172	12
	Rate (%)		14.6	26.8	0	54.8	3.8
(b) PL model rectification							
Conductor	Number	471	465	0	0	0	6
	Rate (%)		98.7	0	0	0	1.3
Shield Wire	Number	314	302	0	0	0	12
	Rate (%)		96.2	0	0	0	3.8

(a)

(b)

(c)

Figure 5.15: Examples of establishing PL model network in the 20023 corridor: (a) raw LiDAR data of PL structures in a span, (b) generation of PL models and POAs in a span, and (c) PL model network.
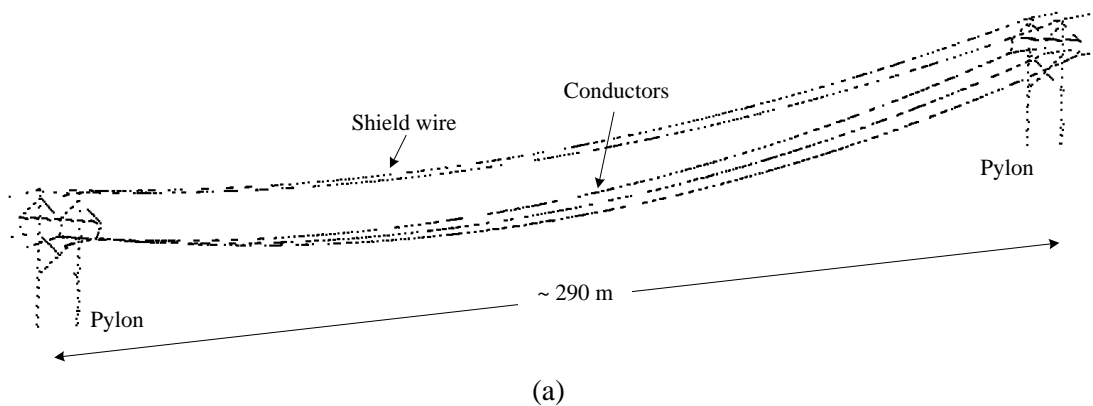
5.4.2.3   20130 PL corridor area

This corridor includes 199 spans and its length runs to about 40.9 km. There are six conductors supporting 345kV which correspond to three bundle wires and two shield wires for a span. For the whole corridor, the number of conductors and shield wires is counted as 714 and 238, respectively. As illustrated in Table 5.7 and Figure 5.16, the first modeling results of conductors and shield wires (see, Table 5.6(a)) reach 28.5% and 16.8% for complete modeling, 2.5% and 13.9% for partial-modeling, 67.5% and 68.5% for over-modeling, and 1.5% and 0.8% for un-detection. Especially, high over-modeling errors occur due to the configuration of bundle

wires under the irregular distribution of PL points. After the PL model rectification, 85% of conductors are completely modeled. However, 13.5% for under-modeling errors newly occurs. The reason for this is mainly subject to several issues. First, we need to turn to a discussion of adaptive optimization of weight factor in the section 5.2.1.2. In the regression model, if the variation of PL orientations is more than 0.2°, it is difficult to properly predict an optimal weight for the complete model correction. Second, let us consider as-built condition of PL arrangement. Within a span, PLs are sometimes placed with different orientations in the construction stage. It causes the increase of variation of PL orientations and a higher weight value is predicted by the regression model, resulting in the merge of PL models closely located. We examined that about 19% of under-modeling errors is subjected to the reason in this corridor. Except for the proportion of un-detection, models for shield wires are completely corrected with satisfied modeling rate of 99.2%.

Table 5.7: Results of the 3D PL model reconstruction (a) before and (b) after the rectification of incomplete PL models in the 20130 PL corridor area.

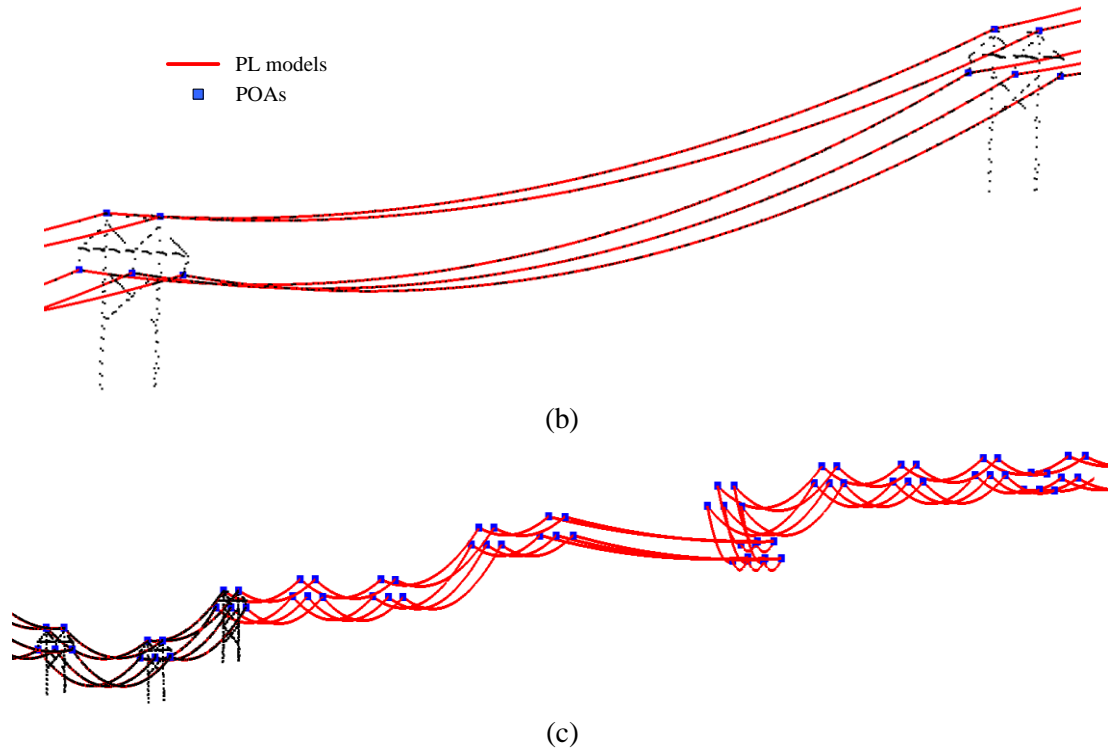| *(a) PL model reconstruction*							
		Total	*Complete Modeling*	*Partial Modeling*	*Under Modeling*	*Over Modeling*	*Un-Detection*
Conductor	*Number*	714	203	18	0	482	11
	Rate (%)		28.5	2.5	0	67.5	1.5
Shield Wire	*Number*	238	40	33	0	163	2
	Rate (%)		16.8	13.9	0	68.5	0.8
(b) PL model rectification							
Conductor	*Number*	714	607	0	96	0	11
	Rate (%)		85.0	0	13.5	0	1.5
Shield Wire	*Number*	238	236	0	0	0	2
	Rate (%)		99.2	0	0	0	0.8

(a)

(b)

(c)

Figure 5.16: Examples of establishing PL model network in the 20130 corridor: (a) raw LiDAR data of PL structures in a span, (b) generation of PL models and POAs in a span, and (c) PL model network.

5.4.2.4   24051 PL corridor area

65 spans with 390 conductors and 130 shield wires belong to the 24051 PL corridor in which the length reaches about 25.9 km. Like the 20130 PL corridor, a span is comprised of six conductors with 345kV (i.e., three bundle-conductors) and two shield wires. As shown in the statistics of Table 5.8, modeling PLs for this corridor seems to be a very challenging task because there is nothing to completely model PLs in the first modeling stage (Table 5.8(a)). It thus incurs partial modeling of 1.5%, over modeling of 97.7%, and un-detection of 0.8% for conductors and over modeling of 100% for shield wires. The main reason is derived from that variations of PL orientations are very severe, that is more than three times larger than others (See, Figure 5.12). The point density on PLs also exhibits very low with a wide range [0.37, 2.64] for conductors (See, Table 5.4). It might seem a reasonable statistics if winds hardly blow out at the epoch of data acquisition. As a result, the probability of hitting a laser pulse to PLs becomes low. However, we have seen that the many errors are to be compensated through the process of PL model rectification. The complete modeling rate increases up to 57.2% for conductors and 100% for shield wires, while under modeling errors of 41.8% newly are introduced. Due to the extremely noisy distribution of PL points, it would be difficult to individually model the PLs in bundle conductors in the proposed framework. Figure 5.17 illustrates an example of modeling PLs and establishing PL network by detecting POAs.

Table 5.8: Results of the 3D PL model reconstruction (a) before and (b) after the rectification of incomplete PL models in the 24051 PL corridor area.

(a) PL model reconstruction

		Total	Complete Modeling	Partial Modeling	Under Modeling	Over Modeling	Un-Detection
Conductor	Number	390	0	6	0	381	3
	Rate (%)		0	1.5	0	97.7	0.8
Shield Wire	Number	130	0	0	0	130	0
	Rate (%)		0	0	0	100	0

(b) PL model rectification

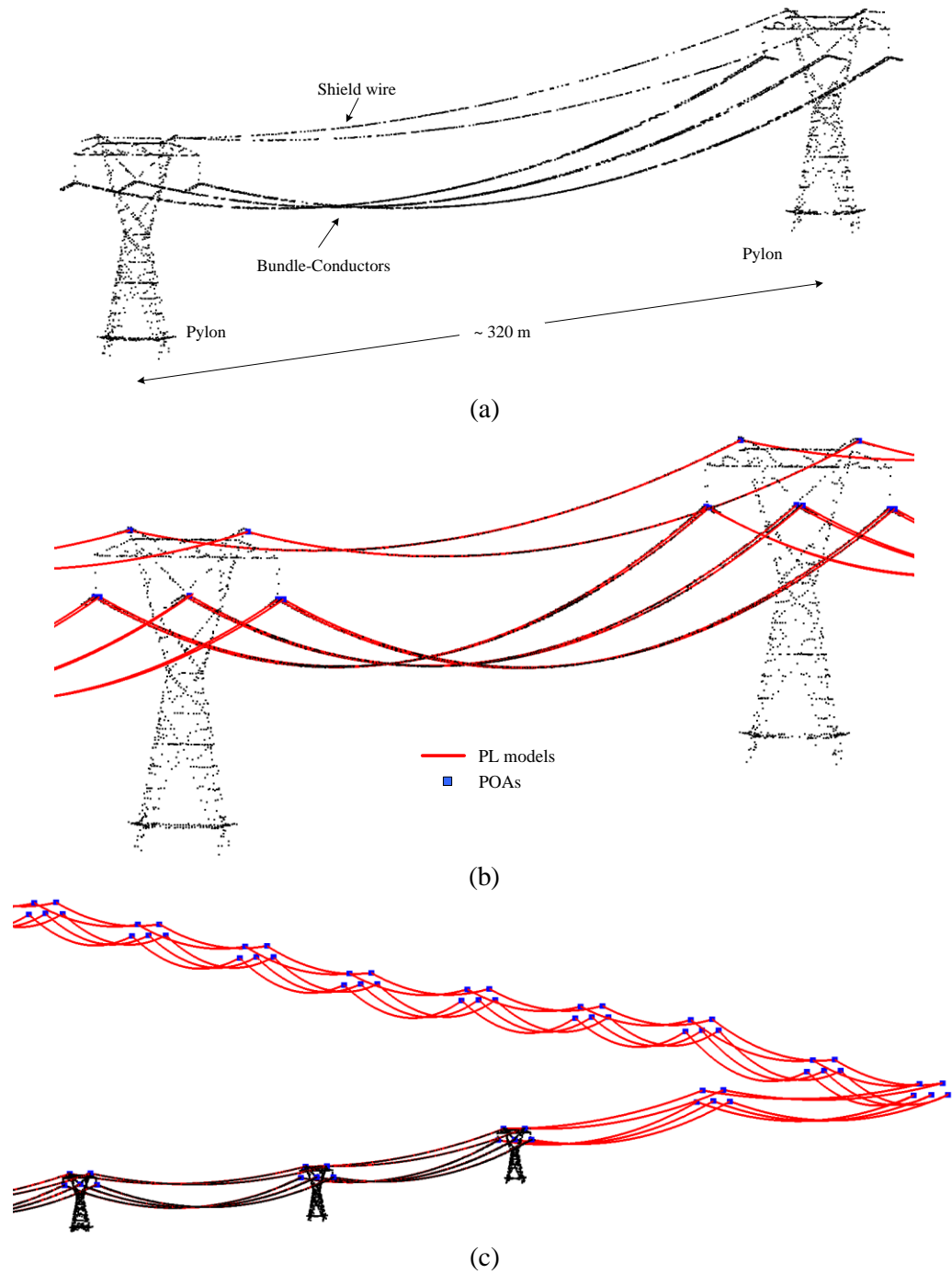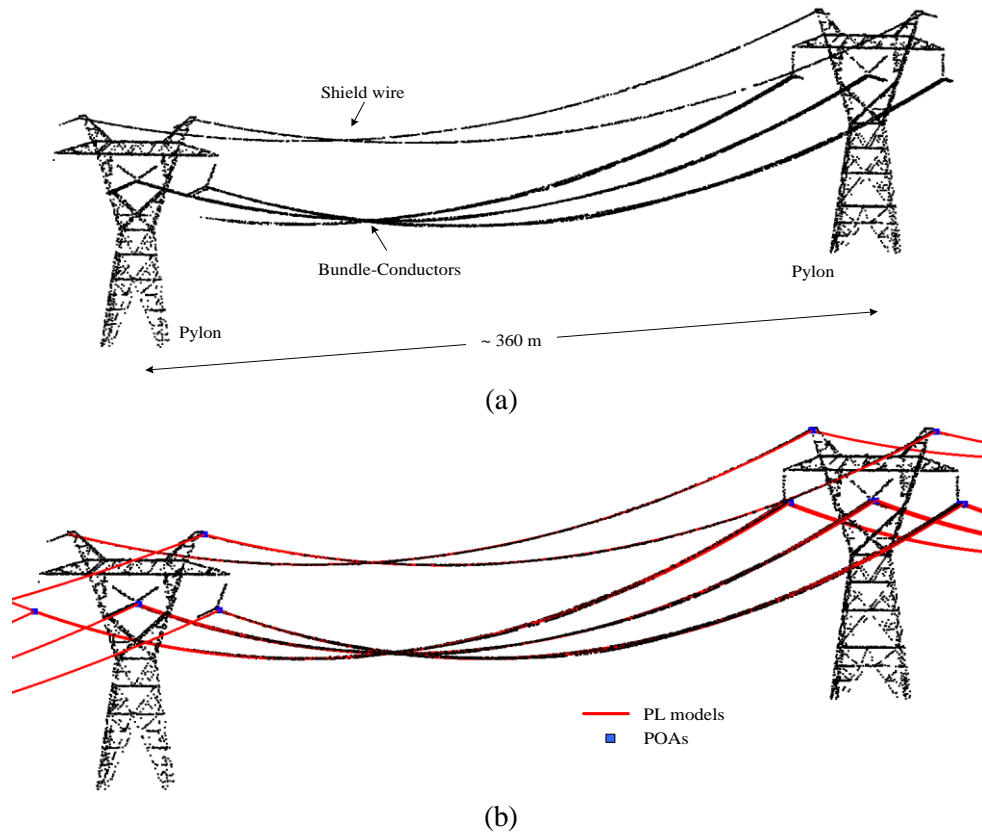|		Total	Complete Modeling	Partial Modeling	Under Modeling	Over Modeling	Un-Detection
Conductor	Number	390	223	0	166	1	3
	Rate (%)		57.2	0	41.8	0.2	0.8
Shield Wire	Number	130	130	0	0	0	0
	Rate (%)		100	0	0	0	0

(a)

(b)

(d)
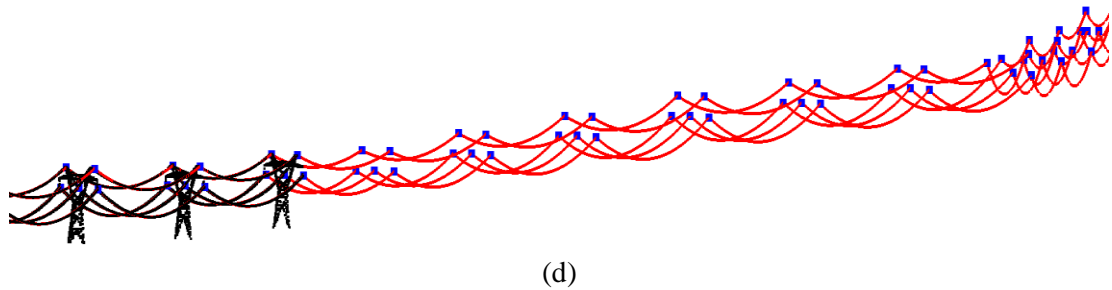
Figure 5.17: Examples of establishing PL model network in the 24051 corridor: (a) raw LiDAR data of PL structures in a span, (b) generation of PL models and POAs in a span, and (c) PL model network.

5.4.2.5 Quality assessment

The quality of PL modeling results including POAs' detection is evaluated in Table 5.9 and 5.10. Table 5.9 shows the PL modeling accuracy which is measured by RMS errors of deviation between each PL model and the corresponding PL points. It is used to judge whether or not the PL models are consistent with the goodness-of-fit condition to inliers. Let us consider the positional accuracy of ALS points (i.e., about 10 cm) in the typical PL corridor mapping. In the most of corridors, the modeling quality is satisfied with the error boundary. However, in case of the 24051 corridor, the deviation extremely increases especially for the shield wires. For this, we can estimate that PL points totally corrupted by systematic errors and/or external forces (i.e., wind effect). Therefore, we can conclude that the use of the data is not appropriate for the generation of PL models. Additionally, to perform an absolute quality measurement of our results, the generated PL models and POAs are compared with a reference which is digitized manually by an operator in the utility company (i.e., GDI) as shown in Table 5.10. For the evaluation of PL models, their 3D middle positions (i.e., sag positions) are used. From the result, we can approximate that the PL

modeling accuracy affects the quality of PL models and POAs. Moreover, in our process framework, as the quality of PL models is degraded, the one of POAs which are detected by the PL models is much the worse.

Table 5.9: PL modeling accuracy

[cm]	Conductor				Shield wire			
Corridor	BD302	20023	20130	24051	BD302	20023	20130	24051
Ave.	3.87	3.49	7.52	24.46	3.88	3.48	6.65	38.65
Min.	3.04	2.94	4.07	6.41	2.72	2.38	3.21	21.73
Max.	5.48	5.13	20.83	40.03	8.23	13.02	20.76	58.24

Table 5.10: Quality of PL models and POAs evaluated by the utility company (GDI)

Corridor	RMSE [cm]	
	PL model	POA
BD302	3.96	21.95
20023	5.18	31.08
20130	19.51	31.08
20145	59.43	65.23

Chapter 6

Conclusions and future directions

6.1 Conclusions

This thesis addressed the new concepts and development of robust methods in reconstructing 3D models of building rooftops and PLs from airborne LiDAR data. The proposed reconstruction scheme deals with model selection problems based on a data-driven approach. The model selection emphasizes that the reconstruction forms are not restricted to a set of models defined with a priori knowledge such as structure type and its size. Therefore, the geometric and topological relationships between primitives constituting significant parts of shape parameters should be optimally determined based on hypothesis model generation and its verification using selection criteria defined. This means that the proposed method is designed to be well suited for the high adaptability to the complex geometric forms of objects of interest.

6.1.1 3D building model reconstruction

The data-driven generic building modeling requires not only recovering detailed rooftop components but also the ability to deal with primitives corrupted by noisy data. Thus, the

regularization is essential step for the generic building rooftop modeling with geometric regular patterns from noisy primitives. In this study, primitives indicate edge segments derived by a successive chain of noisy boundary points and their combinations produce a polyhedral-like rooftop model (a wire-frame structure, CAD model). For its regularization process, a new method, implicit geometric regularization is presented. The implicit means that geometric regularities between line segments such as parallelity, collinearity, and orthogonality are represented implicitly to rooftop models by a set of rules defined during the regularization process instead of explicitly using hard constraints. Rooftop polygon boundaries are also delineated by avoiding redundant fragmented line segments and vertices. The resulting models are good, which means that a majority of rooftop structures is close to the corresponding real geometries. The proposed method presents several interesting aspects:

- *Automation*: a new automatic approach minimizing costly and labour intensive operations is proposed.
- *Robustness*: the proposed method has an ability to deal with building scene complexity including occlusions in which the quality of data shows approximately 0.15m positional accuracy and 0.4m average point distance. The resulting models are generated with less than 1 m positional accuracy of vertices extracted in the ISPRS test data.
- *Adaptive modeling*: the proposed method shows the high adaptability to building rooftops with various degrees of shape complexities, resulting in about 90% completeness in area- and polygon (over 10 m^2 area)-based evaluation in the ISPRS test data.

However, the work presented in this thesis still has some limitations in representing detail building rooftop shapes including arc segments. This is because the quality of extracting building

edge evidences normally relies on the quality of data with random errors and building scene complexity including occlusions.

6.1.2 3D power line model reconstruction

3D modeling of PLs has become an issue of increasing importance for the effective PL risk management. This is due to the fact that PL models are regarded as an essential component for identifying potentially hazardous situations such as vegetation encroachments. This study proposed a new approach, the PMG method, for automatic 3D PL reconstruction from airborne LiDAR data. The proposed method starts by extracting power line candidate points, which are converted into a catenary curve model representing a power line. This initial model is allowed to progressively grow to produce a complete power line model by producing hypothetical growing models and select optimal one. A stochastic constrained non-linear adjustment method is developed for estimating catenary curve model parameters. In evaluating the results of the PMG method, the proposed algorithm provides several promising aspects that could be useful in practice:

- *Automation*: the proposed automatic technique shows the satisfactory success rate for example 96% rate with less than 5.2cm in 3D PL modeling accuracy in the urban data set.

- *Robust modeling*: the proposed model-based approach demonstrates the benefits of reconstructing PL models under a high degree of PL scene complexity. Where, many PLs delivering different voltages are placed closer together in the same direction, but with different heights or run in different directions.

- *Precise modeling*: the individual modeling of PLs is possible even in bundle wires in which PLs are usually placed close to one another at a distance of less than 0.3m orthogonal.

- *Efficient process*: PL points and its corresponding PL models are simultaneously extracted without *a priori* knowledge derived by PL scene classification, which results in the minimization of data processing time and cost.

However, in order to fully gain the practical aspects, there is an issue which we need to overcome. A PL scene complexity affects the performance of our algorithm which causes PL modeling errors such as a partial-, under- and over-modeling errors. The PL scene complexity includes data gaps, vegetation encroachment, bundled wires, as well as combination of various PL voltage types.

6.1.3 3D power line model rectification

To move to correct the incompletion of PL models, their rectification process as a post-processing method was proposed based on the inner and across span analysis. The proposed approach started with PL models using a catenary curve reconstructed by the PMG method. In the inner span analysis, individual PL models of each span are evaluated based on the MDL theory and then erroneous PL segments are replaced by hypothetic PL models through achieving an optimal balance between hypothesized model complexity and its goodness-of-fit to observations, thereby correcting under- and over-modeling errors. In the across span analysis as a subsequent step, detecting precise start and end positions of PL models, called Point Of Attachment (POA) is the most key issue to correct partial modeling errors as well as refine PL models. Final results obtained by the proposed post-processing method showed that:

- *Automation*: the refinement approach of PL models is autonomous without human intervention and capable of achieving the geometric and topological completion of PL models over the whole PL network.

- *Robust modeling*: an important component of this study is the ability to estimate the degree of corruption of PL points and predict suitable model parameters especially under the windy environment. The proposed method produces satisfactory results with overall 90% complete modeling rate in GDI inventory data.

- *Precise modeling*: parameters of PL models are able to be updated so that more accurate information of line length and the positions of POA and sag point can be achieved. In most of GDI inventory data, high PL modeling accuracy with less than 10 cm which indicates deviation between PL models and their member points is obtained. By comparing with references which is digitized by an operator in GDI, the deviation in PL models and their POAs show the range from 4 cm to 20 cm and from 22 cm to 31 cm, respectively.

However, in the corridor affected by the strong wind effect, the quality of PL modeling and its POAs extremely decreases because PL points are totally corrupted by the external forces. For example, approximately 40 cm PL modeling accuracy, and 60 cm and 65 cm deviation in PL models and their POAs from references of GDI. Let us consider that the positional accuracy of airborne LiDAR data is about 10 cm and the design accuracy of PL models is about 15 cm in the as-built condition. We can conclude that the use of the data is not appropriate for the generation of PL models and their components.

6.2 Directions for Future Research

As described in the previous section, this research has covered modeling issues of objects of interest, particularly buildings and PLs, in the PL corridor area. All the proposed methods is implemented and tested, so the research objectives have been achieved satisfactorily. However, in carrying out the effective PL risk management, some of the aspects described in this research need further study, which are summarized as follows:

Effective PL component modeling: As a large model database is available in practice, the use of existing 3D models is to be well suited for the effective modeling of PL components. The model database can be easily obtained from non- and/or commercial model warehouses such as Google 3D warehouse and PLS-CADD in Power Line Systems Inc. The existing geometric and topological information of objects of interest is incorporated into a hypothesis model verification process. Possible research directions may be closely related to the statistical and structural pattern recognition techniques used in the computer vision. The approaches mainly focus on extracting quantitative properties of an object by parameterizing its shape and/or forming a set of syntactic grammars to discriminate geometric properties. Thus, it is expected that the method can reduce geometric distortions in the form of under- and over-modeling errors which is usually derived by the generic modeling method.

Data fusion: A state-of-the-art data acquisition system which is oriented for a corridor mapping produces various data sources including LiDAR points, video, and digital images with different views. Robust data fusion techniques are required to extract detailed contextual information of PL components. It is feasible to recover a parts of PL structures which has not been extracted due to the PL scene complexity.

Further testing: For the practical operations of proposed algorithms, more extensive throughput test to evaluate the efficiency (cost-saving), reliability (accuracy compared to the ground truth) and robustness (testing over more diversified voltage types and structures) should be required.

Bibliography

Abedini, A., Hahn, M., Samadzadegan, F., 2008. An investigation onto the registration of LIDAR intensity data and aerial images using the sift approach. *IAPRS*, 37(Part B1), pp. 169-175.

Ackermann, F., 1999. Airborne laser scanning - present status and future expectations, *ISPRS Journal of Photogrammetry and Remote Sensing*, 54(2-3), pp. 64-67.

Alharthy, A., Bethel, J., 2002. Heuristic filtering and 3D feature extraction from lidar data. In: *Proceedings of the ISPRS Commission III symposium*, XXXIV, part 3A.

Ameri, B., 2000. Feature-Based Model Verification (FBMV): a new concept for hypothesis validation in building Reconstruction, In: *Proceedings of the XIXth ISPRS Congress IAPRS, Vol. XIX, Part 3*, Amsterdam, the Netherlands, pp. 24- 35.

Ameri, B., Fritsch, D., 2000. Automatic 3D building reconstruction using plane-roof structures. *ASPRS Congress*, Washington, DC. 2000.

Axelsson, P., 1999. Processing of laser scanner data – alogorithms and applications. *ISPRS Journal of Photogrammetry and Remote Sensing*, 54, pp. 138-147.

Baarda, W., 1968. A testing procedure for use in geodetic networks. *Publication on Geodesy*, New Series Delft/Netherlands 2(5), pp. 97.

Bang, K., 2010. Alternative methodologies for LiDAR system calibration, Ph.D. thesis.

Baltsavias, E., P., 1999. Airborne laser scanning: basic relations and formulas, *ISPRS Journal of Photogrammetry and Remote Sensing*, 54, pp. 199-214.

Bakhashwain, J., M., Shwehdi, M., H., Johar, U., M., AL-Naim, A., A., 2003. Magnetic fields measurement and evaluation of EHV transmission lines in Saudi Arabia. *Proceedings of the International Conference on Non-Ionizing Radiation at UNITEN (ICNIR 2003)*, pp. 1-17.

Barron, A., Rissanen, J., Yu, B., 1998. The minimum description length principle in coding and modeling. IEEE Transactions on Information Theory, 44(6), pp. 2743-2760.

Belgiu, M., Thomas, J., 2013. Ontology based interpretation of very high resolution imageries grounding ontologies on visual interpretation keys. *16th AGILE International Conference on Geographic Information Science*, 14-17 May 2013, Leuven, Belgium, pp. 1-5.

Betz, H. D., Schumann, U., Laroche, P., 2009. Lightning: principles, instruments and applications. Springer.

Brunn, A., Weidner, U., Forstner, W., 1995. Model-based 2D-shape recovery. In *Proc. of 17. DAGM Conf. on Pattern Recognition*, Springer-Verlag, Berlin, pp. 260-268.

Chan, T., Lichti, D. D., 2011. 3D centenary curve fitting for geometric calibration. IAPRS, Vol. XXXVIII-5/W12, pp. 259-264.

Cheung, K., Yeung, D., Chin, R. T., 2002. On deformable models for visual pattern recognition. Pattern Recognition, Vol. 35, pp. 1507-1526.

Cho, W., Jwa, Y., Chang, H., Lee, S., 2004. Pseudo-grid based building extraction using airborne LiDAR data. In: *Proceedings of the XXth ISPRS congress Istanbul, Turkey, ISPRS*, XXXV, part B.

Clode, S., and Rottensteiner, F., 2005. Classification of trees and power lines from medium resolution airborne laserscanner data in urban environments. *Proceedings of APRS Workshop on Digital Image Computing 2005 (WDIC2005)*, 21 February, Brisbane, Australia, unpaginated CD-ROM.

Cothren, J., 2005. Reliability in constrained Gauss-Markov models: an analytical and differential approach with applications in photogrammetry. Report #473, Geodetic and Geoinformation Science, The Ohio State University.

Csanyi, N., Toth, C.K., 2007. Improvement of lidar data accuracy using lidar-specific ground targets. *PE&RS*, pp. 385-396.

Diana, G., Bocciolone, M., Cheli, F., Gigada, A., Manenti, A., 2005. Large wind-induced vibrations on conductor bundles: laboratory scale measurements to reproduce the dynamic behaviour of the spans and the suspension sets. *IEEE Transactions on power delivery*, 20(2), pp 1617-1624.

Douglas, D. H., Peucker, T. K., 1973. Algorithms for the reduction of the number of points required to represent a digitized line or its caricature. *Canadian Cartographer*, 10(2), pp. 112-122.

Ebisch, K., 2002. A correction to the Douglas–Peucker line generalization algorithm. *Computers & Geosciences*, 28(8), pp. 995-997.

Flood, M., 2011. Workflow challenges on airborne LiDAR electrical transmission project. *Photogrammetric Engineering & Remote Sensing*, 77(5), pp. 438-443.

Franken, P., 2003. Transmission line monitoring through airborne modeling. Fugro-Inpark B.V., Netherlands.

Geist, T., Hofle, B., Rutzinger, M., Pfeifer, N., Stotter, J., 2009. Laser scanning – a paradigm change in topographic data acquisition for natural hazard management. In: *Sustainable Natural Hazard Management in Alpine Environments* edited by Veulliet, E., Stotter, J., Weck-Hannemann, H., Springer, pp. 309-344.

Georgeff, M. P., Wallace, C. S., 1985. A general selection criterion for inductive inference. *European Conference on Artificial Intelligence (ECAI, ECAI84)*, Pisa, pp. 473-482.

Glander, T., Dollner, J., 2009. Abstract representations for interactive visualization of virtual 3D city models. *Computers, Environment and Urban Systems*, Vol. 33, pp. 375-387.

Goodfellow, J., Peterson, W., 2011. Trees and reliability. *Transmission & Distribution World*, ABI/IFORM Global, June 2011, pp. 25-29.

Grunwald, P., 2005. Introducing the minimum description length principle. *In: Advances in Minimum Description Length Theory and Applications*, MIT Press.

Haala, N., Kada, M., 2010. An update on automatic 3D building reconstruction. *ISPRS Journal of Photogrammetry and Remote Sensing*, Vol. 65, pp. 570-580.

Habib, A., 2009. Accuacy, quality assurance, and quality control of LiDAR data. In: Topographic Laser Ranging and Scanning edited by Shan, J., Toth, C. K., CRC Press, pp. 269-294.

Han, S., Hao, R., Lee, J. 2009. Inspection of insulators on high-voltage power transmission lines. IEEE Transactions on Power Delivery, Vol. 24, pp 2319-2327.

Hansen M. H., Yu, B., 2001. Model selection and the principle of minimum description length. *Journal of the American Statistical Association*, 96(454), pp. 746-774.

Hofmann-Wellenhof, B., Lichtenegger, H., Collins, J., 2001. GPS Theory and Practice, *Springer*, New York.

Hu, H., Augenbroe, G., 2012. A stochastic model based energy management system for off-grid solar houses. *Building and Environment*, 50, pp. 90-103.

Hurysz, P., Crider J., 2009. Technology advances vegetation management. *Transmission & Distribution World*, 61(10), pp. 48-51.

Industry Canada, 2003. Electric Power: A canadian specialty – the canadian electric power industry at the service of the world. http://www.international.gc.ca/trade/ner/electric-en.asp (accessed: 15 December 2008).

Ituen, I., and Sohn, G., 2008. A case study: workflow analysis of power line systems for risk management. *International Archives of Photogrammetry and Remote Sensing*, 37(Part B3b): 331-336.

Jwa, Y., Sohn, G., Cho, W., Tao, V., 2008. An Implicit Geometric Regularization of 3D Building shape Using Airborne LiDAR Data. *IAPRS*, 37(PartB3A), pp. 69-76.

Jwa, Y., Sohn, G., 2012. A Piecewise Catenary Curve Model Growing for 3D Power Line Reconstruction, *Photogrammetric Engineering & Remote Sensing*, 78(12), pp. 1227-1240.

Jekeli C., 2001, Inertial Navigation Systems with Geodetic applications. Walter de Gruyter Berlin, New York.

Jelalian, A. V., 1992. Laser radar systems, Artech House, Incorporated, Boston, Massachusetts.

Kersten, Th., Baltsavias E. P., 1994. Sequential estimation of sensor orientation for stereo image sequences. *IAPRS*, 30(5), pp. 206-213.

Kittler, J., Illingworth, J., 1986. Minimum error thresholding. *Journal of Pattern Recognition*, 19(1), pp. 41-47.

Lach, S., Kerekes, J., 2008. Robust Extraction of Exterior Building Boundaries from Topographic Lidar Data. *IEEE Proc. IGARSS*, pp.85-88.

Lee, J., Han, S., Byun, Y., Kim, Y., 2011. Extraction and regularization of various building boundaries with complex shapes utilizing distribution characteristics of Airborne LiDAR points. *ETRI Journal*, 33(4), pp. 547-557.

Li, Z., Liu, Y., Walker, R., Hayward, R., and Zhang, J., 2010. Toward automatic power line detection for a UAV surveillance system using pulse coupled neural filter and an improved hough transform. *Machine Vision and Applications*, 21(5), pp. 677-686.

Liang, X., Lu, M., Zhang, J., 2011. On-site visualization of building component erection enabled by integration of four-dimensional modeling and automated surveying. *Automation in Construction*, 20, pp. 236-246.

Lu, M., L., Kieloch, Z., 2008. Accuracy of transmission line modelling based on aerial LiDAR survey. *IEEE Transactions on power delivery*, 23(3), pp 1655-1663.

Lu, C., Chen, D., Kou, Y., 2003. Algorithms for spatial outlier detection. *Proceedings of the 3rd IEEE International Conference on Data-mining (ICDM'03)*, 19-22 November, Melbourne, FL, unpaginated CD-ROM.

Ma, R., 2005. DEM generation and building detection from lidar data, *PE&RS*, 71(7), pp. 847-854.

Ma, G., Li, C., Quan, J., Jiang, J., Cheng, Y., 2011. A fiber bragg grating tension and tilt sensor applied to icing monitoring on overhead transmission lines. *IEEE Transactions on power delivery*, 26(4), pp 2163-2170.

Mayer, H., 2008. Object extraction in photogrammetric computer vision. *ISPRS Journal of Phtogrammetry & Remote Sensing*, Vol. 63, pp. 213-222.

McLaughlin, R. A., 2006. Extracting transmission lines from airborne lidar data. *IEEE Geoscience and Remote Sensing Letters*, 3(2): 222-226.

Melzer, T., and Briese, C., 2004. Extraction and modeling of power lines from als point clouds. *Proceedings of 28th Workshop of the Austrian Association for Pattern Recognition (OAGM)*, 17-18 June, Hagenberg, Austria, pp. 47-54.

Myung, I. J., 2003. Tutorial on maximum likelihood estimation. Journal of Mathematical Psychology, Vol. 47, pp. 90-100.

Narolski, S., 2010. Is that tree too close?. *Transmission & Distribution World*, ABI/INFORM Global, 62(7), pp. 46-51.

Neal, M., 2009. Aerial laser surveying: data enables arizona public service to locate and eliminate clearance 2 violations and facilitate long-range planning. *Transmission & Distribution World*, June 2009, pp 5-9.

Neidhart, H., Sester, M., 2008. Extraction of building ground plans from LiDAR data. *IAPRS*, 37(Part B2), pp. 405-410.

Orwig, D.A., Abrams, M.D., 1997. Variation in radial growth responses to drought among species, site, and canopy strata. *Trees*, 11, pp 474–484.

Pfeifer, N., Mandlburger, G., 2009. LiDAR data filtering and DTM generation. In: Topographic Laser Ranging and Scanning edited by Shan, J., Toth, C. K., CRC Press, pp. 307-334.

Rahim, A., A., Abidin, I., Z., Tarlochan, F., Hashim, M., F., 2010. Thermal rating monitoring of the TNB overhead transmission line using line ground clearance measurement and weather monitoring techniques. *The 4th International Power Engineering and Optimization Conference (PEOCO2010)*, pp 274-280.

Ramer, U., 1972. An iterative procedure for the polygonal approximation of plane curves. *Computer graphics and Image Processing*, Vol. 1, pp. 224-256.

Rissanen, J., 1983. A universal prior for integers and estimation by minimum description length. The Annals of Statistics, 11(2), pp. 416-431.

Rissanen, J., 1999. Hypothesis selection and testing by the MDL principle. *The Computer Journal*, 42(4), pp. 260-269.

Rottensteiner, F., 2009. Status and further prospects of object extraction from image and laser data. Invited paper at the *2009 Urban Remote Sensing Joint Event*, Chaina, 20-22 May 2009, on CD-ROM.

Rottensteiner, F., Sohn, G., Jung, J., Gerke, M., Baillard, C., Benitez, S., Breitkopf, U., 2012. The ISPRS benchmark on urban object classification and 3D building reconstruction. *XXII ISPRS2012 and 16ARSPC in Melbourne congress*, Aug. 24-Sep. 3, on CD-ROM.

Salameh, H., Hassouna, S., 2010. Arranging overhead power transmission line conductors using swarm intelligence technique to minimize electromagnetic fields. *Progress In Electromagnetics Research B*, 26, pp. 213-236.

Sampath, A., Shan, J., 2007. Building Boundary Tracing and Regularization from Airborne Lidar Point Clouds, *PE&RS*, 73(7), pp. 805-812.

Schenk, T., 2001. Modelling and Analyzing Systematic Errors in Airborne Laser Scanners, Technical Notes in Photogrammetry, Vol. 19, The Ohio State University, Columbus, US.

Scherer, R., J., Schapke, S., E., 2011. A distributed multi-model-based management information system for simulation and decision-making on construction projects. *Advanced Engineering Informatics*, 25, pp. 582-599.

Sen, A., Srivastava, M., 1990. Regression analysis: theory, method, and applications. Springer-Verlag New York Inc.

Shan, J., Lee, D.S., 2002. Generalization of building polygons extracted from IKONOS imagery. *ISPRS Symposium on Geospatial Theory, Processing and Applications*, on CDROM.

Shan, J., Toth, C.K., 2009. Topographic Laser Ranging and Scanning, CRC Press.

Shannon, C. E., 1948. A mathematical theory of communication, Mobile Computing and Communications Review, 5(1), pp. 1-55.

Shoemaker, T., Mack, J., 2011. Lineman and cableman's handbook, New York press.

Smith J., Hall, F., 2011. A proactive approach to tower maintenance. Transmission & Distribution World, 56, pp. 56F-56I.

Snow, K. B., Schaffrin B., 2003. Three-dimensional outlier detection for GPS networks and their densification via the BLIMPBE approach. *Journal of GPS Solution*, 7(2), pp. 130-139.

Sohn, G., Dowman, I., 2007. Data fusion of high-resolution satellite imagery and LiDAR data for automatic building extraction. *ISPRS Journal of Photogrammetry and Remote Sensing*, 62 (1), 43–63.

Sohn, G., Huang, X., Tao., V, 2008. Using binary space partitioning tree for reconstructing 3d building models from airborne lidar data. *Photogrammetric Engineering & Remote Sensing (PE&RS)*, 74(11), pp. 1425-1440.

Sohn, G., Ituen, I., 2010. The Way Forward: Advances in Maintaining Right-Of-Way of Transmission Lines. GEOMATICA, 64(40), pp. 451-462.

Sohn, G., Jung, J., Jwa, Y., Armenakis, C., 2013. Sequential Modeling of Building Rooftops by Integrating Airborne LiDAR Data and Optical Imagery: Preliminary Results, *ISPRS Annals of the Photogrammetry, Remote Sensing and Spatial Information Sciences*, Vol. II-3/W1, pp. 27-33.

Solomonoff, R., 1964. A formal theory of inductive inference. *Information and Control*, 7(1-2), pp. 1-22, 224-254.

Strmiska, R. G., 2000. Five important power line component anomalies. *The International Society for Optical Engineering (SPIE)*, 4020 (85), pp. 85-90.

Sugden, S., J., 1994. Construction of transmission line catenary from survey data. *Applied Mathematics Modelling*, Vol. 18, pp. 274-280.

Taillandier, F., Deriche, R., 2004. Automatic buildings reconstruction from aerial images: a generic bayesian framework. *IAPRS*, Vol. 35, Part 3A, on CDROM.

Tarsha-kurdi, F., Landes, T., Grussenmeyer, P., Smigiel, E., 2006. New approach for automatic detection of buildings in airborne laser scanner data using first echo only. *ISPRS Symposium of Commission III-Photogrammetric Computer Vision*, on CDROM.

Tarsha-Kurdi, F., Landes, T., Grussenmeyer, P., 2008. Extended RANSAC algorithm for automatic detection of building roof planes from LiDAR data. *Photogrammetric Journal of Finland*, 21(1), 97–109.

Toth, C. K., 2009. Strip adjustment and registration. In: Topographic Laser Ranging and Scanning edited by Shan, J., Toth, C. K., CRC Press, pp. 235-268

Ussyshkin, R. V., Smith, R. B., 2007. A new approach for assessing lidar data accuracy for corridor mapping applications. *5th International Symposium on Mobile Mapping Technology*, 29-31 May, Padua, Italy, unpaginated CD-ROM.

Vale, A., Gomes-Mota, J., 2007. Lidar data segmentation for track clearance anomaly detection on over-head power lines. *Proceedings of IFAC Workshop*, 17-18 May, Yzmir, Turkey, pp. 17-19.

Vitanyi, P. M. B., Li, M., 2000. Minimum description length induction, bayesianism, and kolmogorov complexity. *IEEE Transaction on Information Theory*, 46(2), pp. 446-464.

Von Der Gathen, P., 1991. Saturation effects in Na LiDAR temperature measurements. Journal of Geophysical Research: Space Physics, 96(A3), pp. 3679-3690.

Wagen, J., Rizk, K., 2003. Radiowave propagation, building databases, and GIS: anything in common? A radio engineer's viewpoint. *Environment and Planning B: Planning and Design*, 30, pp. 767-787.

Wehr, A., Lohr, U., 1999. Airborne laser scanning—an introduction and overview. *ISPRS Journal of Photogrammetry and Remote Sensing*, 54(2/3), pp. 68-82.

Weidner, U., Forstner, W., 1995. Towards automatic building extraction from high resolution digital elevation models. *ISPRS Journal of Photogrammetry and Remote Sensing*, 50(4), pp. 38-49.

Wolf, P. R., and Ghilani, C. D., 1997. Adjustment Compuations: Statistics and Least Squares in Surveying and GIS. 3rd edition, Wiley-Interscience Publication, pp. 169-200.

Wu, S., Marquez, M.R.G., 2003. A Non-Self-Intersection Douglas-Peucker Algorithm. SIBGRAPI, pp. 60-66.

Xu, J., Wan, Y., YAO, F., 2010. A method of 3D building boundary extraction from airborne LiDAR points cloud. In proceeding of Photonics and Optoelectronic (SOPO), on CD-ROM.

Yan, G., Li C., Zhou, G., Zhang, W., and Li, X., 2007. Automatic extraction of power lines from aerial images. *IEEE Geoscience and Remote Sensing Letters*, 4(3), 387-391.

Yu, B., Liu., H., Wu, J., Hu, Y., Zhang, L., 2010. Automated derivation of urban building density information using airborne LiDAR data and object-based method. *Landscape and Urban Planning*, 98, pp. 210-219.

Zhao, T., Sebo, S. A., Kasten, D. G., 1996. Calculation of single phase AC and monopolar DC hybrid corona effects. *IEEE Transactions on power delivery*, 11(3), pp. 1454-1463.

Zhang, K., Yan, J., Chen, S.C., 2006. Automatic construction of building footprints from airborne lidar data, *IEEE Transactions on Geoscience and Remote Sensing*, 44(9), pp. 2523–2533.